



1 **Tropospheric Ozone Precursors: Global and Regional Distributions, Trends,**  
2 **and Variability**

3

4 Yasin Elshorbany<sup>1\*</sup>, Jerald R. Ziemke<sup>2</sup>, Sarah Strode<sup>2,3</sup>, Hervé Petetin<sup>4</sup>, Kazuyuki Miyazaki<sup>5</sup>,  
5 Isabelle De Smedt<sup>6</sup>, Kenneth Pickering<sup>7</sup>, Rodrigo J. Seguel<sup>8</sup>, Helen Worden<sup>9</sup>, Tamara  
6 Emmerichs<sup>10</sup>, Domenico Taraborrelli<sup>10</sup>, Maria Cazorla<sup>11</sup>, Suvarna Fadnavis<sup>12</sup>, Rebecca R.  
7 Buchholz<sup>9</sup>, Benjamin Gaubert<sup>9</sup>, Néstor Y. Rojas<sup>13</sup>, Thiago Nogueira<sup>14</sup>, Thérèse Salameh<sup>15</sup>, Min  
8 Huang<sup>16</sup>

9

10 \*Correspondence to: elshorbany@usf.edu

11 <sup>1</sup> School of Geosciences, College of Arts and Sciences, University of South Florida, St.  
12 Petersburg, FL, USA

13 <sup>2</sup> NASA Goddard Space Flight Center, Greenbelt, Maryland, USA

14 <sup>3</sup> Goddard Earth Sciences Technology and Research (GESTAR II), Maryland, USA

15 <sup>4</sup> Earth Sciences Department, Barcelona Supercomputing Center, Barcelona, Spain

16 <sup>5</sup> Jet Propulsion Laboratory, California Institute of Technology, Pasadena CA

17 <sup>6</sup> BIRA-IASB, Ringlaan 3 Av. Circulaire, 1180 Brussels, Belgium

18 <sup>7</sup> Dept. of Atmospheric and Oceanic Science, University of Maryland, College Park, MD USA

19 <sup>8</sup> Center for Climate and Resilience Research, Department of Geophysics, Faculty of Physical and  
20 Mathematical Sciences University of Chile, Chile.

21 <sup>9</sup> Atmospheric Chemistry Observations and Modeling (ACOM), National Center for Atmospheric  
22 Research (NCAR), Boulder CO, USA.

23 <sup>10</sup> Institute of Energy and Climate Research, IEK-8: Troposphere, Forschungszentrum Jülich,  
24 Jülich, Germany.

25 <sup>11</sup> Universidad San Francisco de Quito USFQ, Instituto de Investigaciones Atmosféricas, Diego  
26 de Robles y Av Interoceánica, Quito, Ecuador.

27 <sup>12</sup> Center for Climate Change Research, Indian Institute of Tropical Meteorology, MoES, Pune,  
28 India.

29 <sup>13</sup> Department of Chemical and Environmental Engineering, Universidad Nacional de Colombia,  
30 Bogota, Colombia

31 <sup>14</sup> University of São Paulo, São Paulo, Brazil

32 <sup>15</sup> IMT Lille Douai, Institut Mines-Télécom, Univ. Lille, Centre for Energy and Environment, F-  
33 59000 Lille, France.

34 <sup>16</sup> University of Maryland, College Park, MD, USA



35 **Abstract**

36 Ozone formation is nonlinear, and results from the photochemical oxidation of methane and non-  
37 methane hydrocarbons (NMHCs) in the presence of nitrogen oxide ( $\text{NO}_x = \text{NO} + \text{NO}_2$ ). Previous  
38 studies showed that  $\text{O}_3$  short- and long-term trends are nonlinearly controlled by near-surface  
39 anthropogenic emissions of carbon monoxide (CO), volatile organic compounds (VOCs), and  
40 nitrogen oxides. In this article, we investigate tropospheric ozone spatial variability and trends  
41 from 2005 to 2019 and relate those to ozone precursors on global and regional scales. We also  
42 investigate the spatiotemporal characteristics of the ozone formation regime in relation to ozone  
43 chemical sources and sinks. Our analysis is based on remote sensing products of the Tropospheric  
44 Column of Ozone (TrC- $\text{O}_3$ ) and its precursors, nitrogen dioxide (TrC- $\text{NO}_2$ ), formaldehyde (TrC-  
45 HCHO), and total column of CO (TC-CO) as well as ozonesonde data and model simulations. Our  
46 results indicate a complex relationship between tropospheric ozone column levels, surface ozone  
47 levels, and ozone precursors. While the increasing trends of near-surface ozone concentrations can  
48 largely be explained by variations in VOC and  $\text{NO}_x$  concentration under different regimes, TrC-  
49  $\text{O}_3$  may also be affected by other variables such as tropopause height. Decreasing trends in TrC-  
50  $\text{NO}_2$  have varying effects on the TrC- $\text{O}_3$ , which is related to the different local chemistry in each  
51 region. The concomitant increase or decrease in TrC- $\text{O}_3$  and TrC- $\text{NO}_2$  over the eastern US, and  
52 central Europe is due to dominant NO-sensitive conditions resulting from the strict measures to  
53 control  $\text{NO}_x$  emissions over the last two decades. The decreasing trends of TrC- $\text{NO}_2$  but increasing  
54 trends of TrC- $\text{O}_3$  in some regions in the central US and parts of eastern Asia are due to high  $\text{NO}_x$   
55 conditions leading to VOC sensitivity in these regions. We also shed light on the contribution of  
56  $\text{NO}_x$  lightning and soil NO and nitrous acid (HONO) emissions to trends of tropospheric ozone on  
57 regional and global scales.

58



59 **1. Introduction**

60 Tropospheric ozone ( $O_3$ ) is an important air pollutant due to its diverse effects on air quality,  
61 ecosystem (Mills et al., 2018), health (Lefohn et al., 2018; Fleming et al., 2018), and climate  
62 (Boucher et al., 2013; Myhre et al., 2013; Zanis et al., 2022).  $O_3$  is a photochemical product  
63 that results from the oxidation of methane ( $CH_4$ ) and non-methane hydrocarbons (NMHCs) in  
64 the presence of nitrogen oxides ( $NO_x$ ).  $O_3$  is considered a short-lived climate forcer (SLCF)  
65 and is the third-most important greenhouse with a global average radiative forcing of  
66  $(0.34^{+0.09}_{-0.06} \text{ W m}^{-2}$ ; IPCC, 2023). Recent studies showed increasing trends of tropospheric  $O_3$ ,  
67 especially in the temperate and polar regions of the Northern Hemisphere, while the evidence  
68 in the Southern Hemisphere is unclear (Tarasick et al., 2019; Archibald et al., 2020).  
69 Tropospheric  $O_3$  short- and long-term trends are nonlinearly controlled by anthropogenic  
70 emissions of carbon monoxide (CO), volatile organic compounds (VOCs), and nitrogen oxides  
71 ( $NO_x=NO+NO_2$ ). Coupled Model Intercomparison Project Phase 6 (CMIP6) overestimates  
72 observed surface  $O_3$  concentrations in most regions, with larger variability over Northern  
73 Hemisphere (NH) continental regions (e.g., Tarasick et al., 2019; Turnock et al., 2020). The  
74 higher variability in the northern continental regions is due to the variable emissions of ozone  
75 precursors (i.e., CO, VOCs, and  $NO_x$ ). CMIP6 models simulate large increasing trends of  $O_3$   
76 and  $PM_{2.5}$  with an annual mean increase of up to 40 ppb and  $12 \mu\text{gm}^{-3}$ , respectively, over the  
77 historical periods (1850-2014). However, these studies found also that CMIP6 models  
78 consistently underestimate  $PM_{2.5}$  concentrations in the NH, especially during the winter  
79 months, and with larger variability near natural source regions, indicating missing sources  
80 (e.g., HONO) of  $O_3$  (e.g., Elshorbany et al., 2014). Future scenarios show that emission control  
81 measures can influence future changes to air pollutants. Although the global increases in  $CH_4$   
82 abundance may offset benefits to surface  $O_3$  from local emission reductions (Fiore et al., 2002;  
83 Shindell et al., 2012; Wild et al., 2012), recent reports (e.g., Zanis et al., 2022), showed the  
84 dominant role of precursor emission changes in projecting surface ozone concentrations under  
85 future climate change scenarios. In this study, we investigate the relation between ozone trends  
86 and the trends of its precursors.

87 Satellite observations have the advantage of large spatial and consistent temporal coverage.  
88 Tropospheric columns of ozone ( $\text{TrC-O}_3$ ), in Dobson unit ( $1 \text{ DU}=2.69 \times 10^{20} \text{ molecules m}^{-2}$ ),  
89 are usually used to represent tropospheric ozone levels. The tropospheric column of a species  
90 is the species' concentration integrated from the surface to the top of the troposphere, the  
91 tropopause. The tropopause height is dynamically changing, and it varies over time, increasing  
92 or decreasing as a function of several factors, including tropospheric and stratospheric  
93 temperature (warming or cooling). Steinbrecht et al (1998) found that observed tropospheric  
94 warming of  $0.7 \pm 0.3 \text{ K}$  per decade leads to an increase in the tropopause high and a decrease  
95 (at a rate of 16 DU/decade) in the observed column ozone levels. Similarly, after removing the  
96 variations related to major natural forcings, including volcanic eruptions, ENSO (El Niño–  
97 Southern Oscillation), and QBO (Quasi–Biennial Oscillation), Meng et al. (2021) concluded  
98 that a continuous rise of the tropopause in the Northern Hemisphere (NH) from 1980 to 2020  
99 is evident, which they related mainly to tropospheric warming caused by anthropogenic  
100 emissions. Both Steinbrecht et al (1998) and Meng et al. (2021) calculate the same rate of  
101 tropopause increase for the periods 1980-2000 and 1980-2020, respectively. These results  
102 could affect calculated tropospheric ozone trends by changing the volume of the troposphere.  
103 We investigate the trends in  $\text{TrC-O}_3$  and ozone precursors at different column depth and  
104 determine their causal relationships.



105 Global models play a vital role in interpreting the observed trends in ozone precursors,  
106 verifying the consistency of emission inventories with observed precursor concentrations, and  
107 relating trends in ozone precursor emissions to ozone trends. Because satellite measurements  
108 are often sensitive to species concentrations above the surface, models provide additional  
109 information on the vertical distribution of ozone precursors needed to relate emissions or  
110 surface trends to a column or free tropospheric observations. For example, chemical transport  
111 models are used to relate Ozone Monitoring Instrument (OMI) NO<sub>2</sub> columns to surface NO<sub>2</sub>  
112 concentrations and their trends over the United States (e.g. Lamsal et al 2008, 2015; Kharol et  
113 al, 2015) since they provide vertical information on the NO<sub>2</sub> distribution. Models are also used  
114 to infer NO<sub>x</sub> emission trends from observations (e.g. Richter et al., 2005; Stavroukou et al.,  
115 2008; Miyazaki et al, 2016) or to examine whether simulations driven by state-of-the-art  
116 emissions inventories can reproduce observed changes in NO<sub>x</sub> (Itahashi et al., 2014;  
117 Godowitch et al, 2010). Models also provide insight into the role of background NO<sub>2</sub> versus  
118 local sources in relating satellite-observed NO<sub>2</sub> columns to NO<sub>x</sub> emissions changes (Silvern et  
119 al, 2019). Similarly, global models are vital for understanding trends in CO, since the lifetime  
120 of CO allows both local emissions and long-range transport and the global background to  
121 influence regional trends of CO and O<sub>3</sub>. Duncan and Logan (2008) attributed the decreasing  
122 CO in the NH from 1998-1997 to decreasing European emissions and highlighted the role of  
123 Indonesian fires in driving interannual variability. Numerical models can also be used to  
124 assimilate satellite CO observations to invert for CO emission fluxes, often highlighting  
125 differences between bottom-up and top-down inventories (e.g., Kopacz et al., 2010; Fortems-  
126 Cheiney et al., 2011; Elguindi et al., 2020; Gaubert et al., 2020). For instance, several modeling  
127 studies found that the increasing emissions from China in recent years in some emission  
128 inventories were inconsistent with the negative trends observed by MOPITT (Yin et al, 2015;  
129 Strode et al., 2016; Zheng et al, 2019), while the decreases over the United States and Europe  
130 are supported by the observed decrease in CO. Jiang et al (2017) and Zheng et al (2019) also  
131 found that a decrease in biomass burning contributes to the negative CO trend in the NH. Mean  
132 calculated O<sub>3</sub> burden using CMIP6 simulation (Griffiths et al, 2021) revealed an increase of  
133 44% from 1850 to the mean of the period of 2005-2014 and by another 17% until 2100 using  
134 the SSP370 experiments. Other sources of NO<sub>x</sub> such as lightning and soil emissions play an  
135 important role in controlling the O<sub>3</sub> budget, especially in low-NO<sub>x</sub> regions. We investigate  
136 these sources and the role they play in determining O<sub>3</sub> trends and variability on regional and  
137 global scales, as well as their determining factors.

138 Previous literature demonstrates the importance of controlling the emissions of ozone  
139 precursors to effectively reduce surface O<sub>3</sub> levels. Therefore, a thorough and rigorous  
140 understanding of the trends and variability for O<sub>3</sub> precursors is of paramount importance for a  
141 global abatement strategy of O<sub>3</sub> levels. In this study, we use ozonesonde, remote sensing, and  
142 global models to evaluate tropospheric O<sub>3</sub> and O<sub>3</sub> precursor trends of CO, HCHO, and NO<sub>2</sub>,  
143 on regional and global scales.

## 144 2. Methodology

### 145 2.1. Trend Analysis

146 We analyze the historical trends of tropospheric ozone and its precursors CO, NO<sub>2</sub>, and HCHO,  
147 from 2005 to 2019. For trend analysis, we use two methods, the Quantile regression (QR)  
148 method (Chang et al., 2023), and the Weighted Least Squares (WLS). For NO<sub>2</sub> and HCHO, and  
149 CO trends are calculated based on the QR method (Chang et al., 2023), as follows: (1) we first  
150 compute the deseasonalized monthly time series of NO<sub>2</sub> and HCHO tropospheric columns





151 (hereafter referred to as TrC-NO<sub>2</sub>, TrC-HCHO), and CO atmospheric column (TC\_CO), (2) we  
 152 use the quantile regression method for computing the trend, focusing here on the median, and (3)  
 153 uncertainties at a 95% confidence level are estimated using the block bootstrapping approach,  
 154 through 1000 iterations with blocks size of  $N^{0.25}$  with N the number of monthly values. They are  
 155 calculated over a 1°x1° grid and only in cells where at least 75% of the monthly values are  
 156 available. TC\_CO column (see sec. 2.2.1) time series trends are also calculated as Weighted  
 157 Least Squares (WLS) of the monthly anomaly, weighted by the monthly regional standard  
 158 deviation (for comparison with the QR method). For the CO trend map, we use a 12-month  
 159 running average before computing the linear trend (Buchholz et al., 2021). The tropospheric  
 160 ozone column (TrC-O<sub>3</sub>), trends are calculated based on the WLS method. Tropospheric columns  
 161 of satellite observations are calculated based on the WMO thermal definition of the tropopause.  
 162 To account for varying tropospheric column definitions used in previous literature, we also  
 163 evaluate the trends at different column depths.

## 164 2.2. Data resources

165 In this section, we present the different data repositories and their characteristics.

### 166 2.2.1. Satellite data

167 A list of the applied satellite data products and their resolution is shown in Table 1. For  
 168 Tropospheric ozone data, we use the Ozone Monitoring Instrument/Microwave Limb Sounder  
 169 (OMI/MLS) product (Ziemke et al., 2006). The OMI/MLS product is the residual of the OMI total  
 170 ozone column and the MLS stratospheric ozone column, available as gridded monthly means. The  
 171 tropospheric NO<sub>2</sub> column retrievals used were the QA4ECV project (<http://www.qa4ecv.eu/ecvs>)  
 172 version 1.1 level 2 (L2) product for OMI (Boersma et al., 2017a), GOME-2 (Boersma et al.,  
 173 2017b), and SCIAMACHY (Boersma et al., 2017c). The ground pixel sizes of the OMI, GOME-  
 174 2, and SCIAMACHY retrievals are 13 km×24 km, 80 km×40 km, and 60 km×30 km, with local  
 175 Equator overpass times of 13:45, 09:30, and 10:00 LT, respectively. We also use HCHO  
 176 tropospheric columns retrieved from OMI (De Smedt et al. 2018) from the QA4ECV project.  
 177 Atmospheric total column CO daytime observations were obtained from the MOPITT instrument  
 178 aboard the Terra Satellite (Barret et al., 2003; Buchholz et al., 2017). Monthly daytime L3 data  
 179 were obtained at 1° gridded horizontal resolution from the NASA Langley Research Center  
 180 Atmospheric Science Data Center (ASDC), using version 9 (V9) retrievals, and the joint near-  
 181 infrared/thermal-infrared product (Deeter et al., 2022).

182

183 **Table 1.** Satellite data products and their reference periods.

Parameter	Resolution (Satellite pixel size)	Instrument/Platform	Reference Period	Reference
NO <sub>2</sub>	1°x1° (13 km x 24 km)	OMI/Aura	2005–2020	Boersma et al., 2017a
NO <sub>2</sub>	1°x1° (40 km x 80 km)	GOME-2/METOP-A	2007–2018	Boersma et al., 2017b



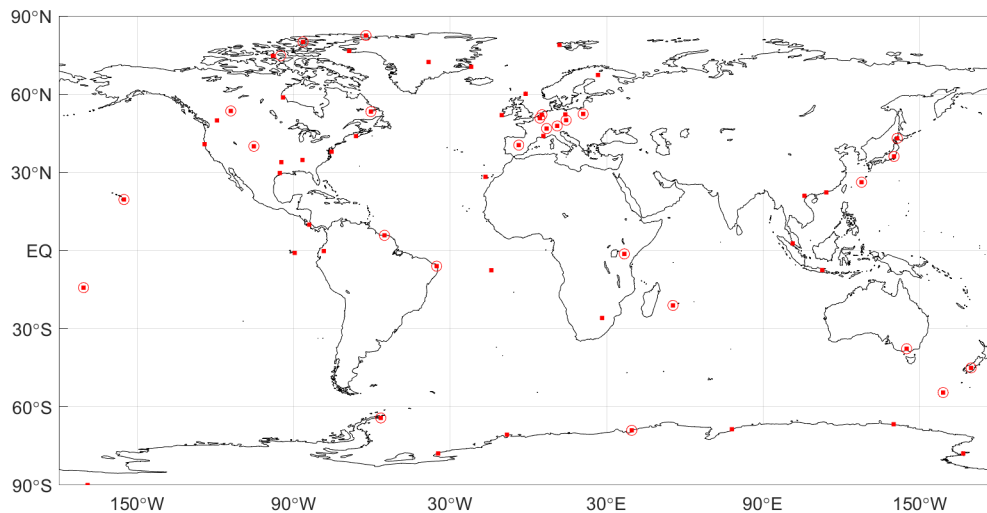
Parameter	Resolution (Satellite pixel size)	Instrument/Platform	Reference Period	Reference
NO <sub>2</sub>	1°x1° (30 km x 60 km)	SCIAMACHY/ENVISAT	2005–2011	Boersma et al., 2017c
CO	1°x1° (22 km x 22 km)	MOPITT/TERRA	2002–2020	Deeter et al., 2022
HCHO	1°x1° (13 km x 24 km)	OMI/Aura	2004–2020	De Smedt et al., 2018
Ozone	1°x1°	OMI/MLS	2004–2020	Ziemke et al., 2006

184

### 185 2.2.2. Ozonesonde Data

186 Direct sampling of ozone throughout the atmospheric column by ozonesondes on board of high-  
 187 altitude balloons is a primary source of information of the ozone abundance and changes in the  
 188 free troposphere. Ozonesonde data have been used extensively for satellite ozone product  
 189 validations, trend analyses, and as a priori climatology profiles for satellite retrieval algorithms  
 190 (McPeters and Labow, 2012; Labow et al., 2015; Hubert et al., 2021; Christiansen et al., 2022;  
 191 Newton et al., 2016). Ozonesondes networks around the globe have been providing the ozone  
 192 community with accurate in situ measurements of high vertical resolution (100-m) for the last 5  
 193 decades in the Northern Hemisphere (Krizan and Lastovicka, 2005), nearing 3 decades at  
 194 stations in the tropics (Thompson et al., 2017), and in the last decade, new efforts are  
 195 contributing with data from undersampled regions such as the tropical Andes (Cazorla and  
 196 Herrera, 2022). Other important contributions include dedicated campaigns for regional studies  
 197 (i. e. Newton et al., 2016; Fadnavis et al., 2023). Figure 1 shows a map with ozonesonde stations  
 198 around the globe whose data are publicly available from data providers (station names,  
 199 coordinates, and links for data access in the Supplementary Material, Table S1).

200



201

202 Figure 1: Ozone-sounding stations around the globe (red squares) whose data are publicly  
 203 available (Table S1). Stations that meet the criteria to calculate trends (Wang et al., 2022) are  
 204 circled in red.

205

206 **2.2.3. Model simulations of ozone precursors and their vertical distribution**

207 Model simulations provide information on the vertical distribution of trace gases that can help  
 208 interpret the observed columns. Here, we use the Goddard Earth Observing System (GEOS)  
 209 Earth System Model (Molod et al, 2015) running with the GMI chemistry mechanism (Duncan et  
 210 al, 2007; Strahan et al, 2007; Nielsen et al, 2017) to simulate the contributions of the lower,  
 211 middle, and upper troposphere to the tropospheric columns of ozone and its precursors. The  
 212 MERRA-2 reanalysis (Gelaro et al., 2017) constrains the GEOS-GMI meteorology. The GEOS-  
 213 GMI meteorology is replayed to the MERRA-2 meteorology as described in Orbe et al (2017).  
 214 Liu et al (2022) evaluated another GEOS simulation with GMI chemistry with satellite  
 215 observations of TrC-O<sub>3</sub>, TrC-NO<sub>2</sub>, TrC-HCHO and TC-CO.

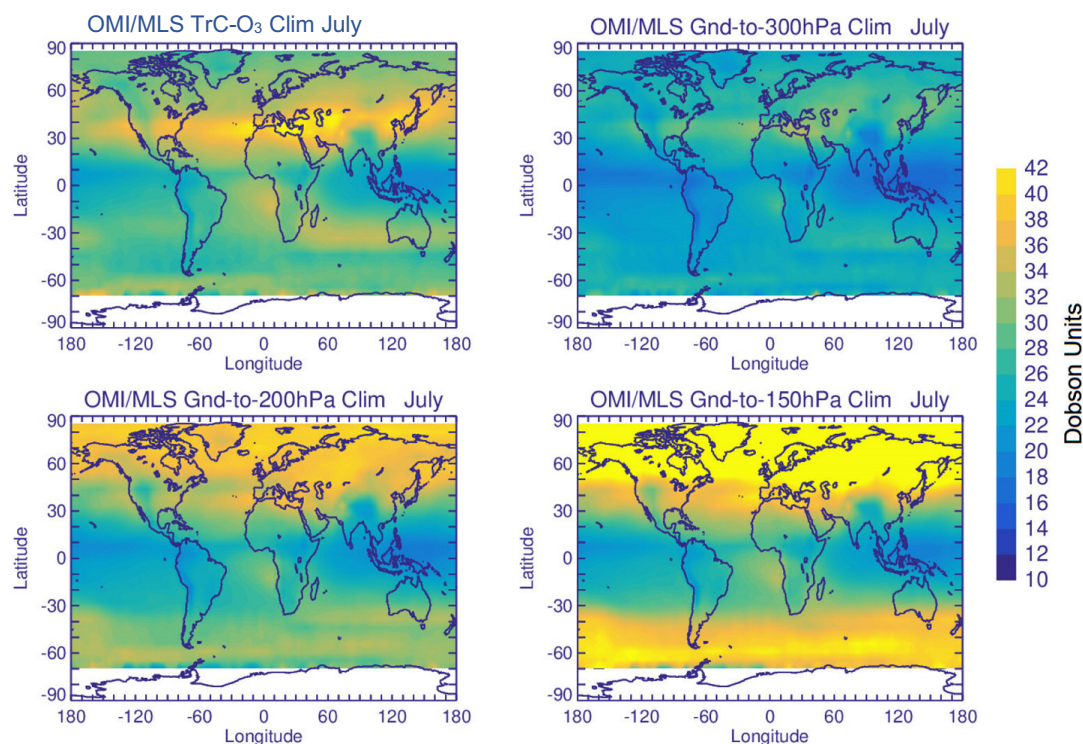
216 **3. Data Analysis and Discussion**

217 **3.1. TrC-O<sub>3</sub> Sensitivity to Tropopause**

218 Calculated TrC-O<sub>3</sub> depends on several factors such as tropospheric ozone levels, atmospheric  
 219 warming (e.g., due to GHG emissions) or cooling (stratospheric or tropospheric (e.g., after major  
 220 volcanic eruptions), and tropopause height (TH). Atmospheric warming or cooling can lead to a  
 221 decrease or an increase, respectively, of TrC-O<sub>3</sub> due to the respective change in the TH. Several  
 222 methods are used to determine the TH. The WMO thermal definition (WMO) for the first TH,  
 223 the lowest altitude level at which the lapse rate decreases to 2° K km<sup>-1</sup> or less, provided that the  
 224 average lapse rate between this level and all higher levels within 2 km does not exceed 2° K km<sup>-1</sup>.  
 225 A second tropopause may be also found if the lapse rate above the first tropopause exceeds  
 226 3°K km<sup>-1</sup> (WMO, 1992; Hoffmann and Spang (2022). Other studies define the TH based on  
 227 fixed pressure levels (from ground to 150, 200, 300, and 400 hPa). Mean OMI/MLS TrC-O<sub>3</sub>  
 228 values in July (2005-2019) calculated based on the WMO thermal definition, are shown in  
 229 Figure 2. TrC-O<sub>3</sub> values are comparable to previously reported CMIP6 and satellite  
 230 measurements (Griffiths et al., 2021). Partial ozone columns (OC) calculated from the ground to



231 different pressure levels, 150, 200, and 300 hPa show increasing OC values with increasing  
232 column depth, with calculated OC at 150 and 200 hPa being the closest to the TrC-O<sub>3</sub> WMO  
233 values, still overestimating OC in the northern hemisphere (50-90° N), especially for the 150 hPa  
234 OC, see Figure 2.  
235

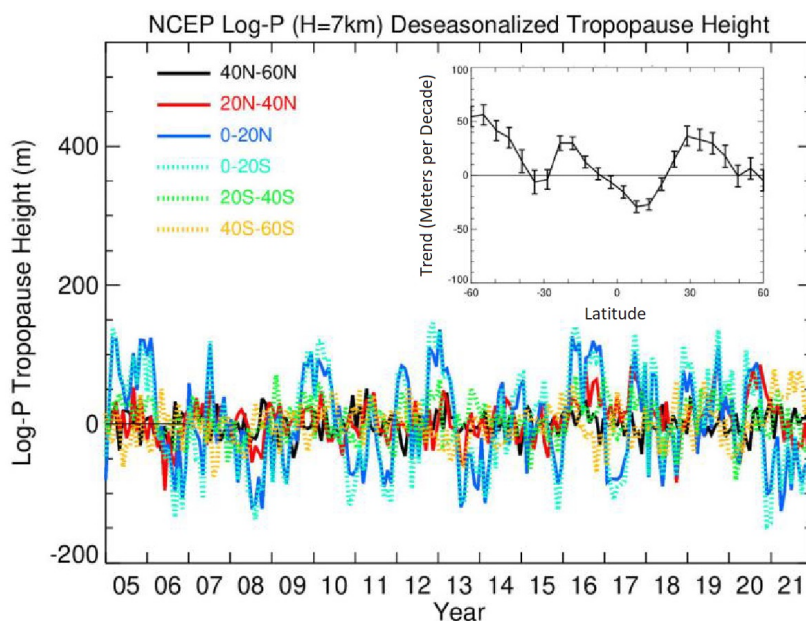


236  
237 Figure 2: Global Mean Column Ozone based on the WMO definition as well as to different  
238 pressure levels.  
239

240 Steinbrecht et al (1998) found that observed tropospheric warming of  $0.7 \pm 0.3$  K per decade  
241 leads to an increase in the TH and a decrease in total ozone. They also calculated a decrease of  
242 16 DU/km increase in TH. These results indicate the importance of TH on calculated long-term  
243 ozone trends. This could also affect comparisons between trends calculated based on different  
244 TrC-O<sub>3</sub> definitions and near-surface ozone levels. The time series of deseasonalized TH from  
245 2004 to 2021 are shown in Figure 3 together with their zonal mean trends. Trends in TH are  
246 positive reaching 60 meters/decade except in a narrow band in the tropics from 10°S to 20°N and  
247 at 30°S, where TH decreases at a rate up to 30 meters/decade. TH in the tropical regions is also  
248 characterized by high variability (see Figure 3). These results are also consistent with recent  
249 reports showing a positive trend of TH from 20-80°N at a rate of 50-60 m/decade (Meng et al.,  
250 2021). They related this increase primarily to tropospheric warming. The decrease of the TH in  
251 the tropics may contribute by some extent to the increasing TrC-O<sub>3</sub> trend in this region (see sec.  
252 3.4). These results show also that using a fixed pressure level for the tropopause may not be  
253 accurate given the change in TH over time. In the following sections, tropospheric columns will  
254 be calculated based on the WMO tropopause definition.



255



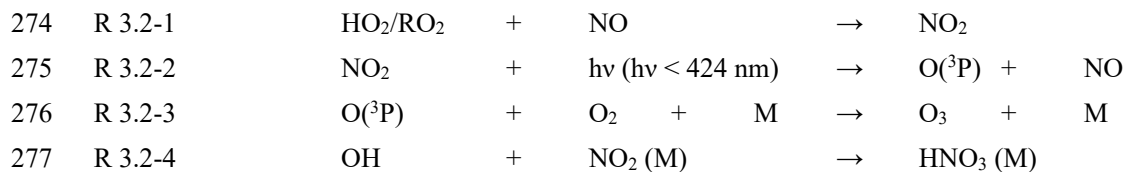
256

257 Figure 3: National Centers for Environmental Prediction (NCEP) WMO (2K/km) tropopause  
 258 log-P height time series with trends (meters/decade) embedded.

259

### 260 3.2. Spatial Distribution of O<sub>3</sub> and its Precursors

261 Tropospheric O<sub>3</sub> is a photochemical product that results from the photolysis of NO<sub>2</sub>. Therefore,  
 262 the sources and fate of NO<sub>2</sub> in the atmosphere determine O<sub>3</sub> burden and distribution. NO<sub>2</sub> is  
 263 formed from the reaction of hydrogen proxy (HO<sub>2</sub>) and alkyl proxy (RO<sub>2</sub>) radicals with NO (R  
 264 3.2-1). While photolysis of NO<sub>2</sub> is the main source of ozone, high NO<sub>2</sub> levels can suppress O<sub>3</sub>  
 265 levels as NO<sub>2</sub> reacts with OH radical forming HNO<sub>3</sub> (R 3.2-2 to R 3.2-4), thus reducing the  
 266 oxidation rate of hydrocarbons and respectively HO<sub>2</sub> and RO<sub>2</sub> levels, leading to a net loss of O<sub>3</sub>  
 267 (e.g., Elshorbany et al., 2010). Ozone production efficiency is calculated as the ratio of the  
 268 number of NO<sub>2</sub> molecules photolyzed to form O<sub>3</sub> to that lost due to the reaction with OH  
 269 forming HNO<sub>3</sub>. Under NO-sensitive conditions, the decrease in NO<sub>x</sub> leads to a reduction in OH,  
 270 HCHO, and O<sub>3</sub>. However, under high NO conditions, a reduction in NO<sub>x</sub> could lead to an  
 271 increase in photochemical products, OH, HCHO, and O<sub>3</sub> because a reduction in NO<sub>2</sub> leads to a  
 272 decrease in OH loss rate, thus higher HO<sub>2</sub> and RO<sub>2</sub> production (Elshorbany et al., 2009; 2010;  
 273 2012).



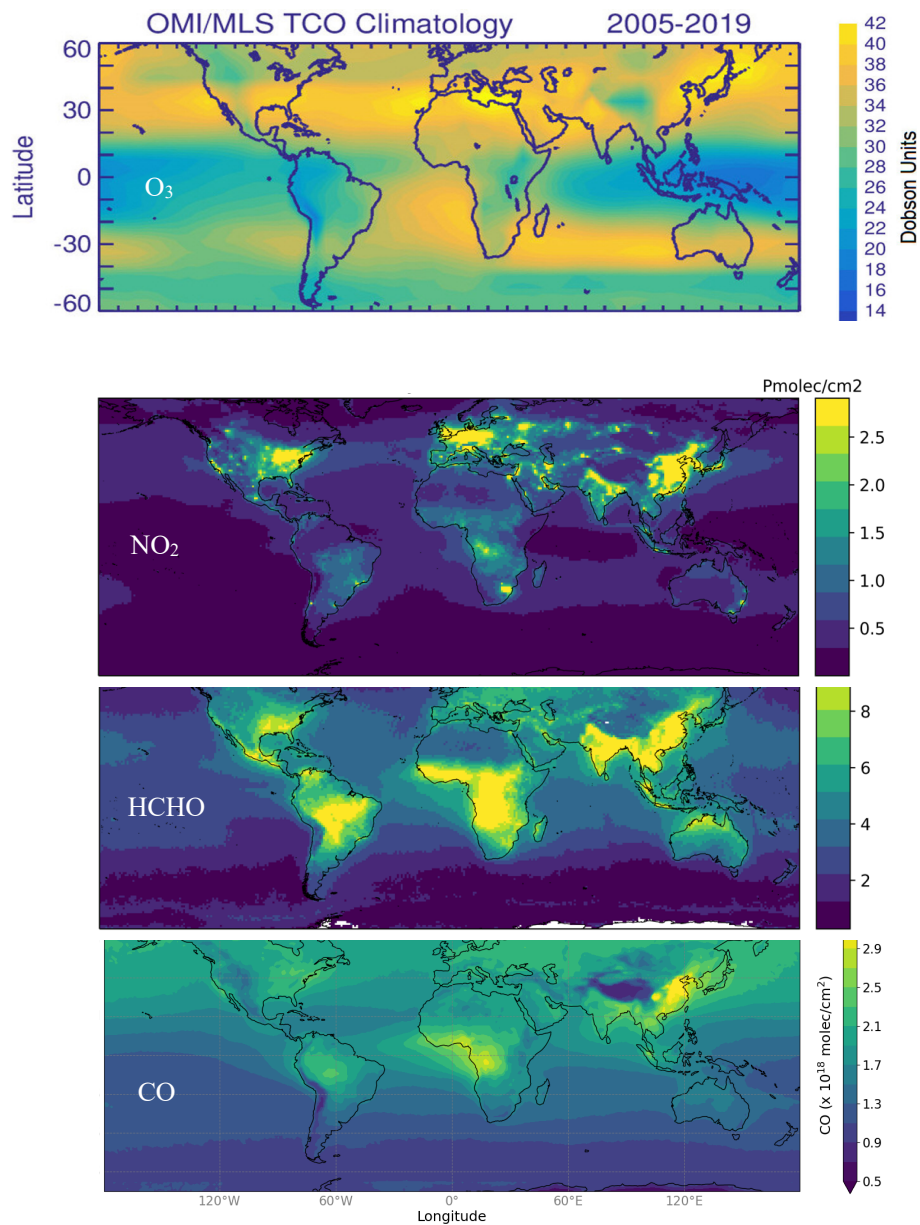
278



279 The observed mean tropospheric columns of O<sub>3</sub>, NO<sub>2</sub>, and HCHO and atmospheric column of  
280 CO from 2005 to 2019 are shown in Figure 4. NO<sub>2</sub> concentration has been decreasing since 2005  
281 in North America, Europe, and Australia, mainly due to the applied strict measures to reduce air  
282 pollution. Since O<sub>3</sub> is a photochemical product that is formed based on non-linear chemistry, a  
283 reduction in NO<sub>2</sub> may lead to an increase or decrease in tropospheric O<sub>3</sub> levels based on the  
284 dominant photochemical regime in the respective region. The highest values of the NO<sub>2</sub>  
285 tropospheric column are in the northern hemisphere between 10 °N and 50°N, especially over the  
286 eastern US, northern Europe, and east and south Asia, with elevated levels between 10 and 30°S,  
287 especially in sub-Saharan Africa, and Brazil. TrC-O<sub>3</sub> is also highest over the band of 20-50° N,  
288 especially over the eastern coast of the US, southern Europe, and east Asia. Some differences  
289 exist between O<sub>3</sub> and NO<sub>2</sub> spatial patterns which is due to the different photochemical sensitivity  
290 (see sec. 3.4). On average, the northern hemisphere has higher CO than the southern hemisphere  
291 due to a larger number of sources. Additionally, high amounts of CO are found in regions with  
292 large anthropogenic sources (e.g., eastern China) or regions with large and regular fire seasons  
293 (e.g., central Africa). HCHO and CO show a similar spatial pattern over western Africa due to  
294 emissions from biomass burning. In the following sections, global and regional trends of TrC-O<sub>3</sub>  
295 are investigated along with tropospheric ozone precursors.

296





297

298 Figure 4: Mean (2005-2019) of TrC-O<sub>3</sub>, TrC-NO<sub>2</sub>, TrC-HCHO, and TC-CO.

299

### 3.3. Simulated O<sub>3</sub> Precursors

300

301

302

303

304

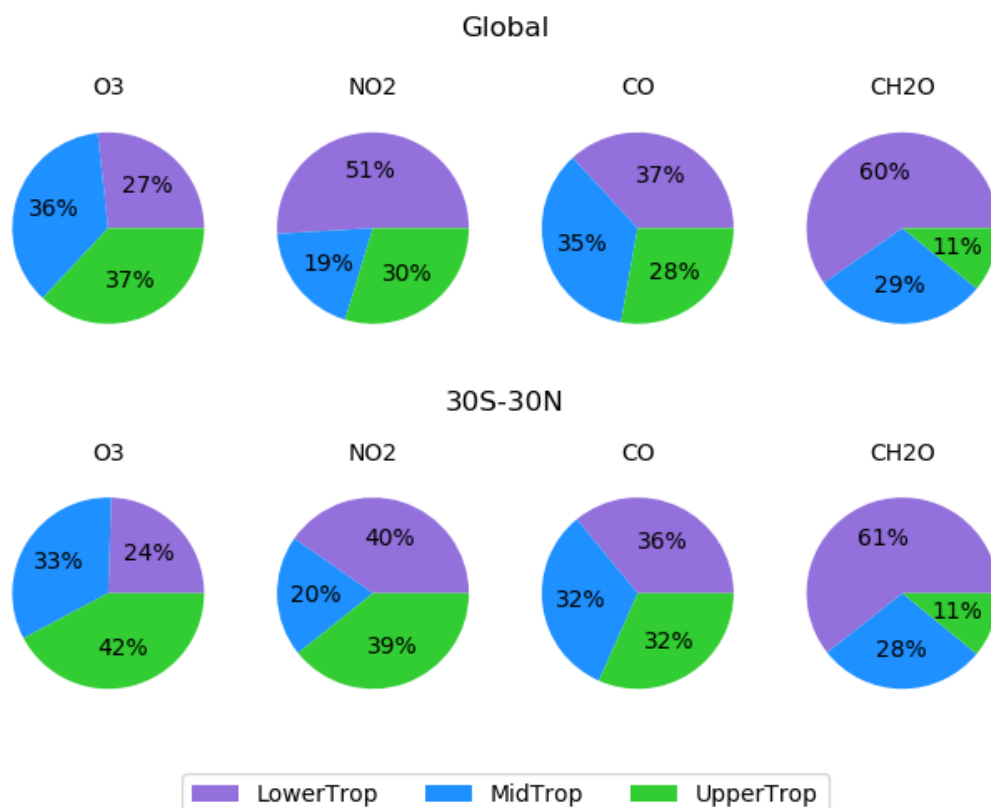
305

Ozone and its precursors differ in their vertical distribution through the troposphere. In this section, we use the GEOS GMI simulations to show how the lower, middle, and upper troposphere contribute to the simulated columns of O<sub>3</sub> and its precursors to complement the column information from satellites. Figure 5 shows the simulated mean (2005-2019) contributions to tropospheric columns of O<sub>3</sub>, NO<sub>2</sub>, formaldehyde, and CO, partitioned into the lower (up to 700hPa), middle (700-400hPa), and upper (400hPa to tropopause) portions of the



306 tropopause for the tropical band (30°S:30°N) and the global mean. The middle and upper  
 307 troposphere make large contributions to the simulated TrC-O<sub>3</sub> and its variability (Figure 5),  
 308 while the lower troposphere makes the largest contribution to the HCHO column since it is  
 309 mainly a photochemical product (e.g., Elshorbany et al., 2009), and all three levels make  
 310 substantial contributions to the CO column. Globally, the lower troposphere makes the largest  
 311 contribution to the simulated tropospheric NO<sub>2</sub> column due to the larger NO<sub>x</sub> emissions in the  
 312 northern hemisphere.

313



314

315 Figure 5: Simulated average (2005-2019) contributions to the tropospheric columns of O<sub>3</sub>, NO<sub>2</sub>,  
 316 formaldehyde, and CO from the lower (surface-700hPa), middle (700-400hPa), and upper  
 317 troposphere (400hPa-tropopause) using NASA GEOS5 GMI. The top row is for the global mean,  
 318 while the bottom row is averaged from 30°S-30°N.

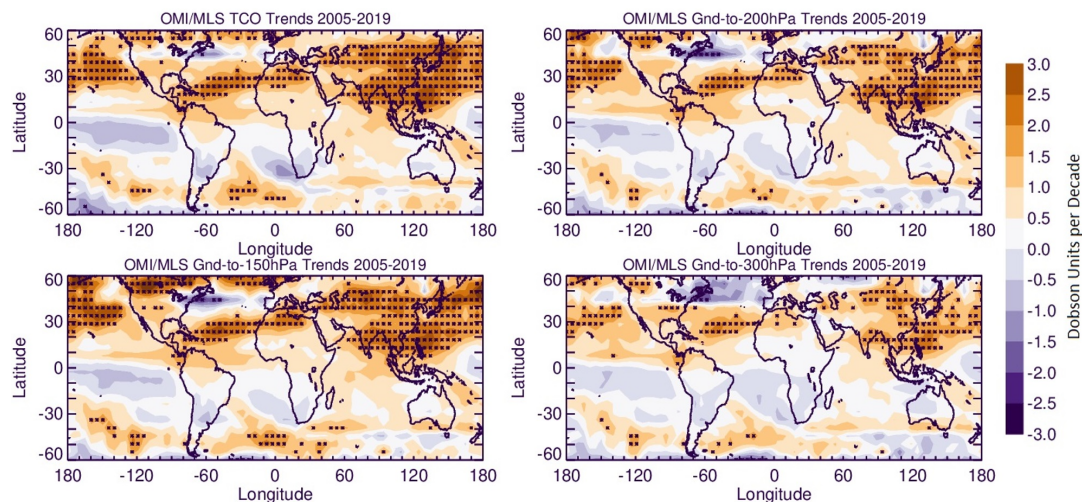
### 319 3.4. Tropospheric Trends

#### 320 3.4.1. Global Tropospheric Ozone

321 Global TrC-O<sub>3</sub> trends calculated for different column depths are shown in Figure 6. Compared to  
 322 TrC-O<sub>3</sub>, OC trends up to 150 hPa seem to be the closest despite OC values being much higher  
 323 than that of the TrC-O<sub>3</sub> (Figure 2). All significant trends are positive indicating increasing trends  
 324 of ozone columns, regardless of the tropopause height. Insignificant (at 2  $\sigma$  levels) decreasing  
 325 TrC-O<sub>3</sub> trends were also found in some locations, e.g., South Australia, South Africa, and the



326 eastern coast of the US. As mentioned in sec. 3.1, TrC-O<sub>3</sub> trends in the northern tropics may be  
 327 slightly enhanced by the decreasing TH trends in that region (Steinbrecht et al., 1998). In  
 328 contrast, increasing TrC-O<sub>3</sub> trends in other regions may be slightly offset by the increasing TH  
 329 trends (see Figure 3).

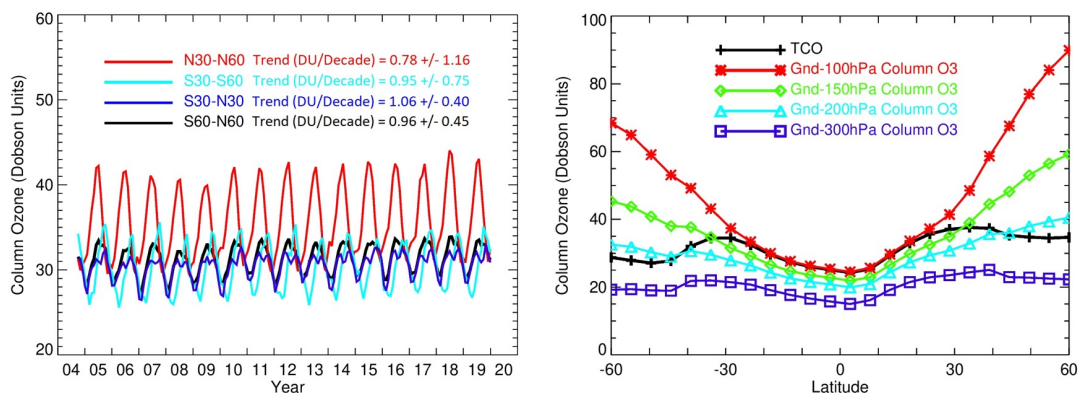


330

331 Figure 6: Trends in tropospheric column ozone, based on the WMO thermal definition, and the  
 332 trends on ozone columns (from ground to 150, 200, and 300 hPa). Trends are calculated based on  
 333 deseasonalized monthly data from 2004 to 2021. Asterisks denote significant trends (different  
 334 from zero at 2 $\sigma$  level).

335

336 The time series of OMI/MLS TrC-O<sub>3</sub> averaged over several latitudinal bands as well as at  
 337 different column depths are shown in Figure 7. Zonal mean TrC-O<sub>3</sub> compares well with partial  
 338 ozone columns in the tropics (from 30°S to 30°N) with the OC of up to 300 hPa differing by  
 339 about 10 DU from the TrC-O<sub>3</sub> (Figure 7). The lowest TrC-O<sub>3</sub> trends are located in the northern  
 340 hemisphere (30°N – 60°N) at  $0.78 \pm 1.16$  DU/decade, followed by the southern hemisphere (30°S -  
 341 60°S) ( $0.95 \pm 0.75$  DU/decade) and the tropical band (30°S -30°N) ( $1.06 \pm 0.40$  DU/decade). In  
 342 addition, the continental trends over Australia, South Africa, and South America in the 30-60°S  
 343 band are essentially negative and the positive trends in this band are driven mainly by oceanic  
 344 emissions (Figure 6). The positive trends in the 30-60°N band are slightly offset by the negative  
 345 trends over Eastern US and Europe (see Figure 6).



346

347 Figure 7: Time series and zonal mean trends of OMI/MLS TrC-O<sub>3</sub> in different latitudinal bands  
 348 (left) and for different column depths (right) from 2005-2019.

349

350 Observed trends for the time period before COVID-19 (2005-2019) show that OC trends  
 351 were highest in the northern latitudes (0-30° N) reaching about 1.5 DU/decade, followed by the  
 352 northern midlatitudes 30-60°N (Figure 8). The high trends in the 30-60°N band are dominated by  
 353 transpacific impacts as well as some impacts from East Asia. The positive trends in the southern  
 354 hemisphere (0-30° S) are mainly over Amazonia and Southeast Asia, being offset by small  
 355 negative trends over Western Australia and South Africa. The trends during the time period  
 356 (2005-2021) show a significant decline in O<sub>3</sub> column trends in the northern hemisphere but a  
 357 slightly increasing trend in the southern hemisphere. The decreasing trends in the northern  
 358 hemisphere during the COVID-19 is consistent with previous literature showing a significant  
 359 decrease in several pollutants including NO<sub>2</sub> and O<sub>3</sub> due to the extended lockdown periods  
 360 imposed during the pandemic (e.g., Bauwens et al., 2020; Elshorbany et al., 2021). The decrease  
 361 of NO<sub>2</sub> under the dominant NO-sensitive conditions in Europe and the USA led to a decrease in  
 362 tropospheric O<sub>3</sub>. The increase in the southern hemisphere is due to a variety of reasons including  
 363 the lesser impact of the pandemic (Oleribe et al., 2021), and persistent pollution issues, even  
 364 during the pandemic (Matandirotya et al., 2023). In addition, most regions in the southern  
 365 hemisphere are VOC-sensitive regions, conditions under which the reduction in NO<sub>2</sub> would lead  
 366 to an increase in tropospheric O<sub>3</sub> (see sec. 3.4)

367 Zonal mean trends (Figure 8) show that OC up to 150 hPa is almost identical to that of  
 368 TrC-O<sub>3</sub> except for the high latitudes 45°-60° S and 45°-60° N. The decreasing trends above 30°N  
 369 and 30°S are due to the offsetting impact of negative trends over Eastern US and Europe in the  
 370 north, and Australia and South Africa in the south, respectively. This impact is less apparent in  
 371 the 150 hPa due to the lower positive trends in that band compared to TrC-O<sub>3</sub>. The 200 hPa OC  
 372 comes next with a very good agreement from 60° S to 10° N. followed by the 100 hPa which is  
 373 only in good agreement from 30° S to 30°N, while the 300 hPa OC was the farthest from the  
 374 TrC-O<sub>3</sub>. The decreasing trends of O<sub>3</sub> over Eastern US and Europe are consistent with the  
 375 decreasing trend of NO<sub>2</sub> (see below), which is due to the successful measures applied since 2004  
 376 to mitigate air pollution in these regions. The decrease of O<sub>3</sub> is a result of decreasing NO<sub>2</sub> trends  
 377 demonstrating the NO-sensitive conditions dominating these regions.

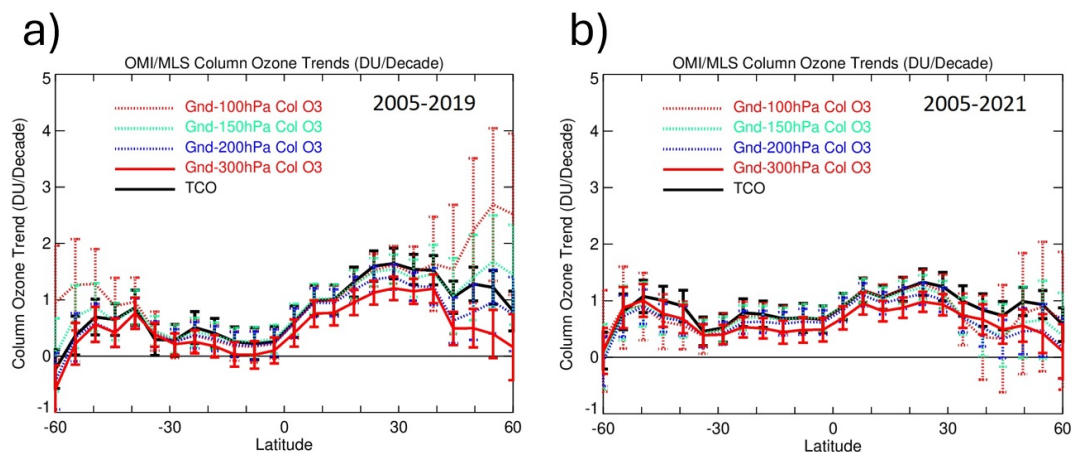
378

379





380



381

382 Figure 8: Tropospheric column ozone (TrC-O<sub>3</sub>) and trends for different column depths before the  
383 COVID-19 pandemic (2005-2019) and including the pandemic (2005-2021).

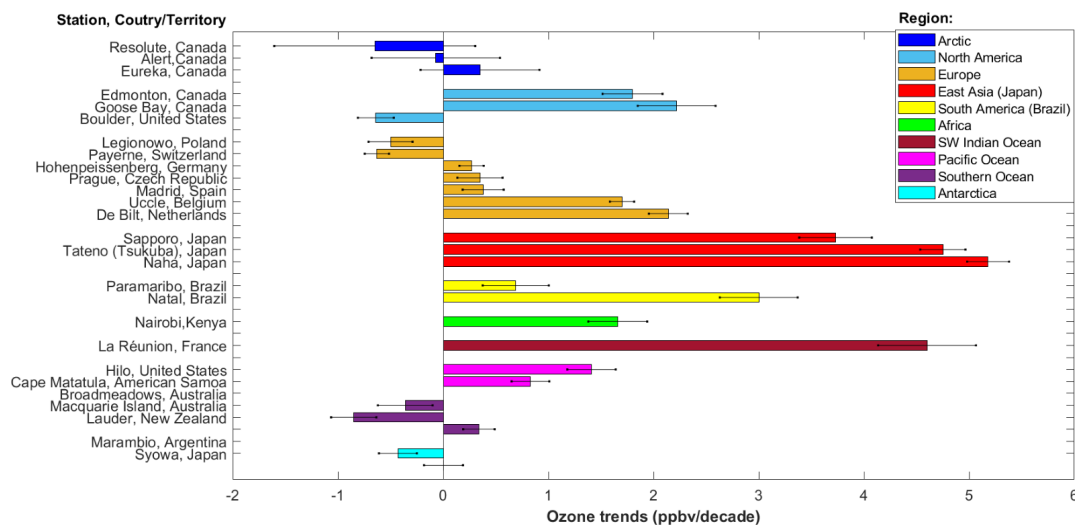
384

385 **3.4.2. Free tropospheric trends**

386 Trends of ozone in the free troposphere presented here are based on ozonesonde data from the  
387 literature. Despite the high stability of ozonesonde measurements across the global networks  
388 over several decades (Stauffer et al., 2022), the spatial sparsity of sounding stations and non-  
389 uniform sampling frequency among sites is a limitation in using these data to produce trends.  
390 These shortcomings have constrained the ability to include data from many stations in previously  
391 published analyses. Recently, it was proven that minimum temporal requirements to calculate  
392 trends from ozonesondes demand sampling to be executed at least three times per month (Wang  
393 et al., 2022; Christiansen et al., 2022) with at least eight months of sampling in a year, and at  
394 least 15 annual means for an analysis of about two decades (Wang et al., 2022). With these  
395 criteria, recent ozonesonde trend analyses indicate that ozone concentration increased globally by  
396 1.8±1.3 ppbv/decade in the free troposphere within 800 to 400 hPa (Christiansen et al., 2022).  
397 However, there is significant regional variability, as illustrated in Figure 9 where ozone trends  
398 published by Wang et. Al. (2022) (1995-2017 data between 950-250 hPa) are organized by  
399 regions and stations. For example, ozone in East Asia (Japan) has been increasing at a rate of 3.5  
400 to 5 ppbv/decade, particularly since 2010 (Christiansen et al., 2022). Over the Southwestern  
401 Indian Ocean (La Réunion), trends are of similar magnitude (>4.5 ppbv/decade). In tropical  
402 South America, over the Atlantic basin region (Paramaribo and Natal), sounding measurements  
403 also show ozone increases by almost 3 ppbv/decade (Natal), but other regions in South America  
404 continue to lack sufficient measurements to produce trends. At tropical stations in Africa  
405 (Nairobi) and the Pacific Ocean (Hilo and American Samoa) trends are also positive, although of  
406 lower magnitudes (0.83-1.7 ppbv/decade). In contrast, polar stations both at the Arctic and  
407 Antarctica as well as the Southern Ocean show overall decreasing ozone concentrations to non-  
408 significant trends. Exceptions are the Eureka station in Canada and Lauder station in New  
409 Zealand, which both show slight ozone increases (less than 0.5 ppbv/decade). The direction of  
410 regional trends by Wang et. al. (2022) is consistent with regional trends presented in similar  
411 independent research (Christiansen et al., 2022). As atmospheric composition continues to  
412 become modified under the current regime of climate change, building consistent and longer



413 time series of ozonesonde measurements at other regions will continue to be an important source  
 414 of firsthand information to assess tropospheric ozone changes and trends.



415  
 416 Figure 9: Ozone trends in the free troposphere from ozonesonde measurements calculated by  
 417 Wang et. Al. (2022) and organized by region and station. Data covers the 1995-2017 period  
 418 within 950 to 250 hPa. Error bars show 1-σ uncertainty.

419

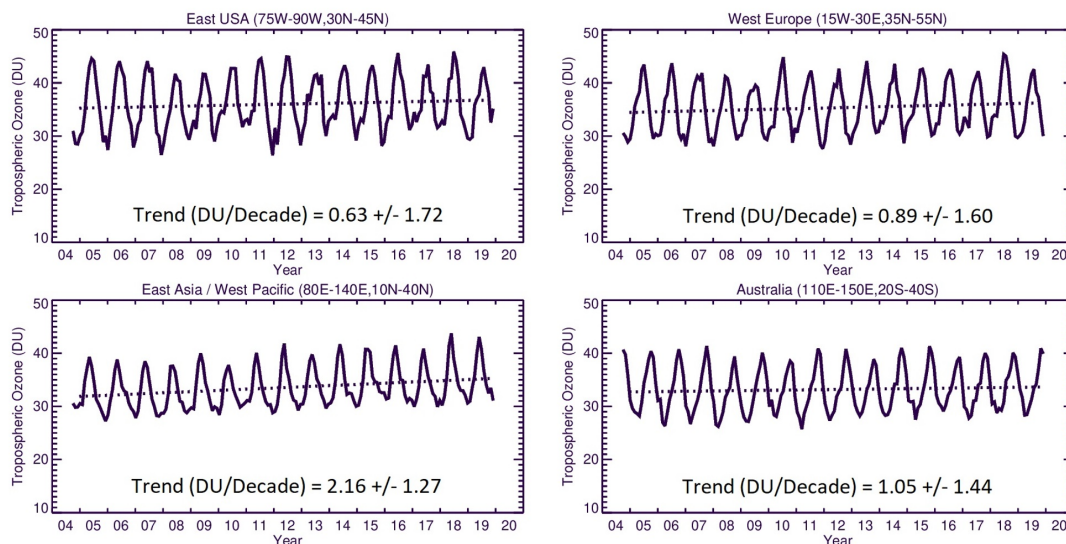
### 420 3.4.3. Regional Ozone Trends

421 As shown in Figure 10, the highest OMI/MLS regional trend is observed over East Asia  
 422 ( $2.16 \pm 1.27$  DU/decade) while the lowest trend is calculated over Eastern USA ( $0.63 \pm 1.72$ )  
 423 followed by Western Europe ( $0.89 \pm 1.60$ ) and Australia ( $1.05 \pm 1.44$ ) DU/decade. We next  
 424 calculate the monthly trends from the GEOS-GMI simulation to investigate how the simulated  
 425 trends vary by altitude.

426

427





428

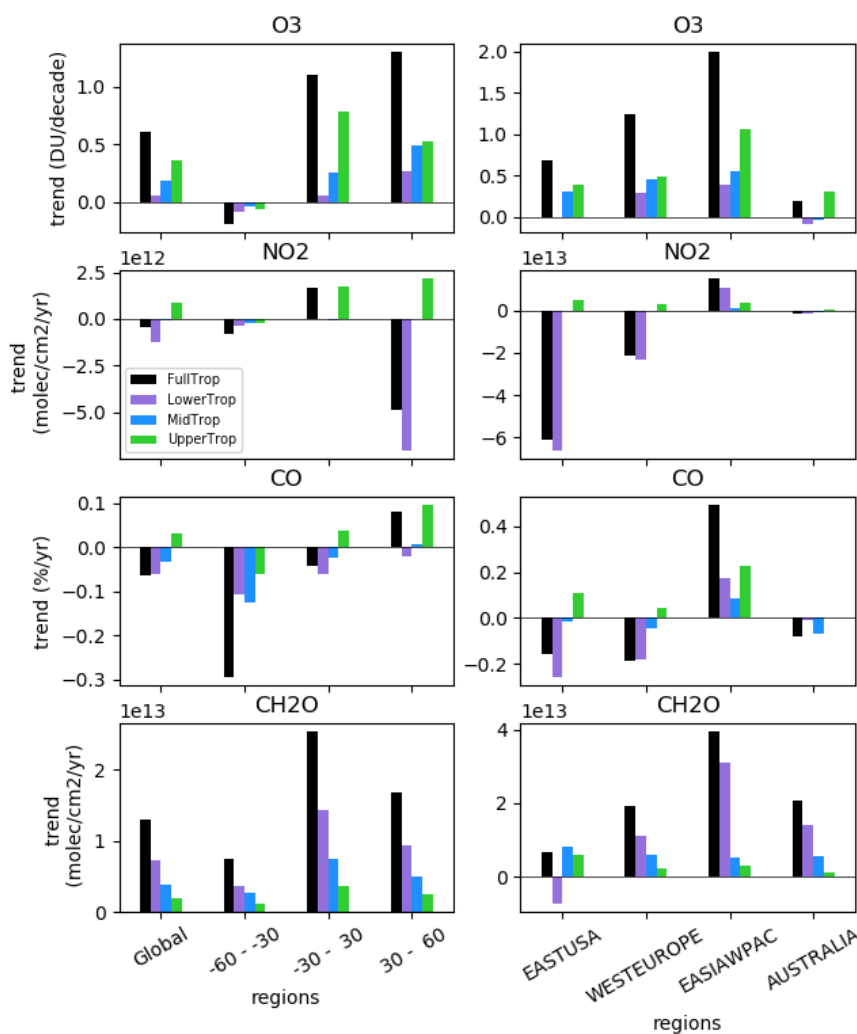
429 Figure 10: OMI/MLS observed regional mean trends of TrC-O<sub>3</sub>.

430

431 The simulated trends in partial columns of O<sub>3</sub>, NO<sub>2</sub>, formaldehyde, and CO from 2005 to 2019  
432 for different pressure levels as well as the tropospheric columns are shown in Figure 11. The  
433 simulated tropospheric columns of O<sub>3</sub> and HCHO show a positive trend in most regions (Figure  
434 11), consistent with the results of Liu et al (2022) using a different GEOSCCM simulation. Liu et  
435 al (2022) highlighted the importance of formaldehyde trends for analyzing the simulated trends  
436 in tropospheric ozone. Considering different latitude bands, the highest trends are simulated  
437 between 30° S and 60° N, consistent with calculated trends based on satellite observations (see  
438 sec. 3.4). In contrast, the simulated NO<sub>2</sub> and CO trends are mostly negative, although positive  
439 trends are simulated over East Asia. The largest NO<sub>2</sub> negative trends are in the northern  
440 hemisphere between 30°N and 60°N. The decreasing NO<sub>2</sub> trends but increasing O<sub>3</sub> and HCHO  
441 trends in the northern hemisphere are due to the NO-sensitive conditions prevailing over Europe  
442 and the USA.

443

444



445

446 Figure 11: Global and regional trends in O<sub>3</sub>, NO<sub>2</sub>, CO, and HCHO calculated from the GEOS  
 447 GMI simulation for the tropospheric column (black), lower troposphere (purple), middle  
 448 troposphere (blue), and upper troposphere (green) from 2005 to 2019. The lower, middle, and  
 449 upper troposphere are defined as in Figure 5.

450

451 The simulation provides an estimate of the relative contribution from different portions of the  
 452 tropospheric column to the column trends and shows that this contribution varies by region and  
 453 constituent. The middle and upper troposphere make the largest contributions to the simulated  
 454 TrC-O<sub>3</sub> trend globally, with large contributions from the upper troposphere driving the simulated  
 455 TrC-O<sub>3</sub> trend at 30°S-30°N and counteracting the negative TrC-O<sub>3</sub> trend in the southern  
 456 midlatitudes (Figure 11). However, the middle and lower troposphere make larger contributions  
 457 to the positive TrC-O<sub>3</sub> trends in the northern middle and high latitudes. The middle and upper  
 458 troposphere contribute most of the simulated positive TrC-O<sub>3</sub> trend over the eastern USA, while  
 459 the lower and middle troposphere are more important over western Europe, and all three levels



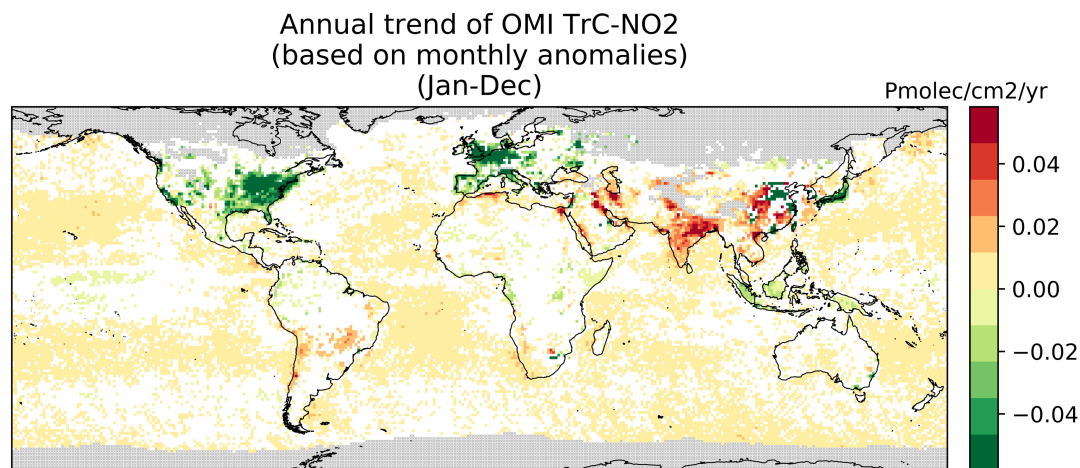
460 contribute over East Asia. The upper troposphere makes the primary contribution to the  
 461 simulated trend over Australia. Simulated TrC-O<sub>3</sub> trends are also quite comparable to those  
 462 observed by OMI/MLS within the measurement model uncertainty (see Figure 10 and Figure 7).  
 463 Over Australia, the OMI/MLS trend of 1.05 DU/decade is higher than the model trend of about  
 464 0.2 DU/decade (see Figure 11). However, since OMI/MLS trend has a calculated uncertainty  
 465 (2σ) of 1.44 DU/decade, both the model and OMI/MLS for Australia are not statistically  
 466 different.

467 While the upper troposphere is a major driver of the simulated TrC-O<sub>3</sub> trends, the lower  
 468 troposphere is the largest contributor to the simulated trends in the tropospheric NO<sub>2</sub>, CO, and  
 469 HCHO trends globally and over many regions (Figure 11). Exceptions include the simulated  
 470 HCHO column over the Eastern USA, which is driven by the middle and upper troposphere; an  
 471 important role for upper tropospheric CO over East Asia; and the CO trend over Australia driven  
 472 by the middle tropospheric contribution. Figure 11 also shows that in some regions, such as the  
 473 eastern USA for all 3 precursors, the upper and lower tropospheric trends counteract each other,  
 474 reducing the magnitude of the column trend. In the following sections, we investigate trends and  
 475 variability in O<sub>3</sub> precursors, NO<sub>2</sub>, CO, and HCHO.

#### 476 3.4.4. NO<sub>2</sub> Trends

477 The TrC-NO<sub>2</sub> trends over 2005-2019 are shown in Figure 12 with a regional summary in Figure  
 478 13. On a global scale, there is a strong spatial variability of the TrC-NO<sub>2</sub> trends. About a third of  
 479 the oceans show significantly increasing TrC-NO<sub>2</sub> (at 95% confidence level), especially at mid-  
 480 latitude, with trends up to +0.01 Pmolec/cm<sup>2</sup>/yr, while only a few cells in the equatorial Pacific  
 481 show a significant decrease.

482



483

484 Figure 12: Global trends of OMI NO<sub>2</sub> tropospheric column (TrC-NO<sub>2</sub>) over 2005-2019 (see text  
 485 for details on the calculation of the trends). Grey areas correspond to areas without enough data,  
 486 white areas correspond to regions where the trends remain statistically insignificant at a 95%  
 487 confidence level.

488 Regional trends are shown in Figure 13. For significant trends in a given region, the  
 489 numbers correspond to the percentiles 5/50/95 of trends among the different cells of the region  
 490 where trends are significant. Each region is tagged with a circle whose size is proportional to the  
 491 p50 of the significant trends (red for positive and green for negative), which allows us to quickly



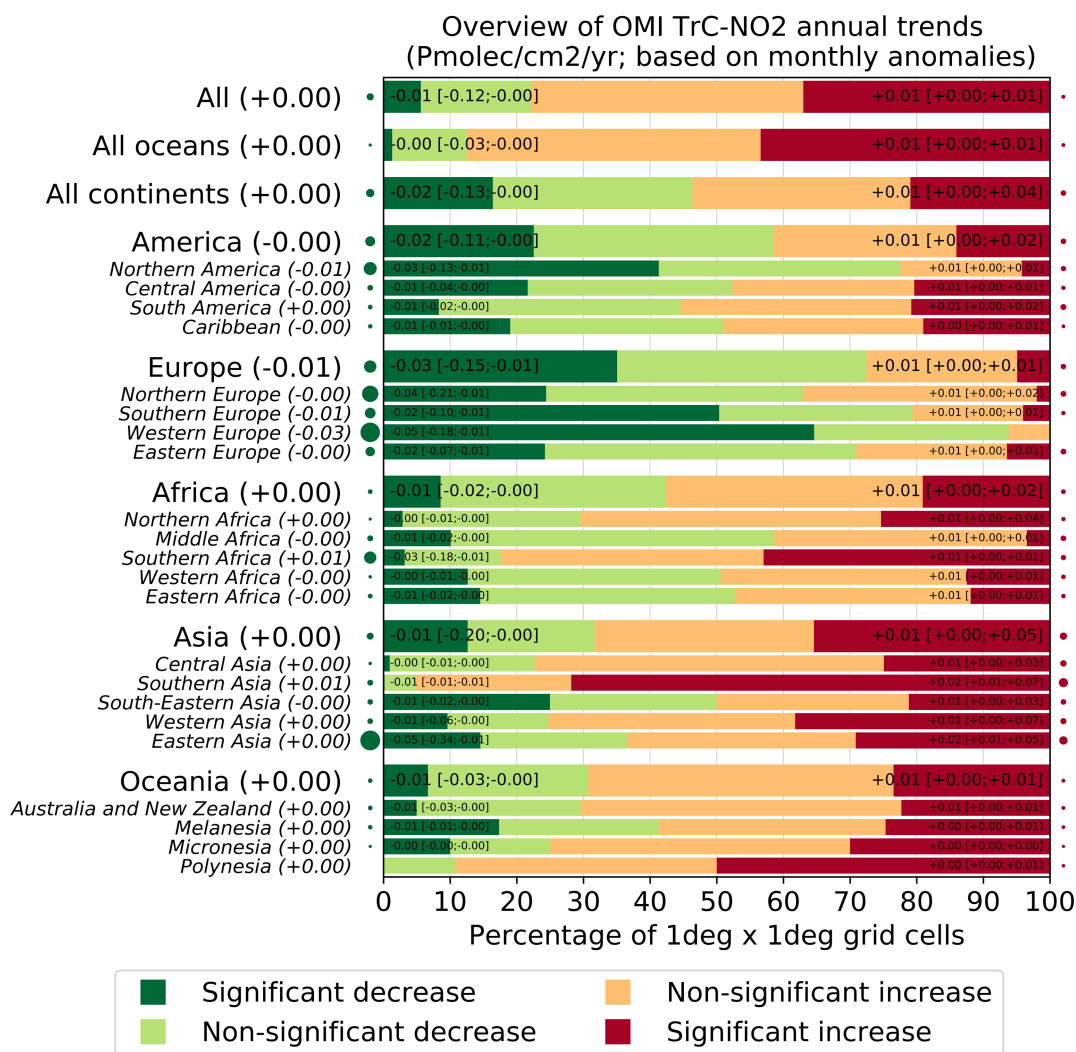
492 see regions where the trend is strong. For instance, for Eastern Asia (this region includes 1442  
493  $1^\circ \times 1^\circ$  grid cells) about 15% of the grid cells (about 216 grid cells) in this region show a  
494 significant decrease in TrC-NO<sub>2</sub>. Over these specific 216 cells with a significant decrease of  
495 TrC-NO<sub>2</sub>, the 5th and 95th percentile of the trend is -0.34 and -0.01, respectively, Pmolec/cm<sup>2</sup>/yr  
496 About 28% of the grid cells in this region show a significant increase of TrC-NO<sub>2</sub> (which means  
497 about 403 grid cells). Over these specific 403 cells with a significant increase of TrC-NO<sub>2</sub>, the  
498 5th (resp 95th) percentile of the trend is +0.01 (resp 0.05) Pmolec/cm<sup>2</sup>/yr. Therefore, the Eastern  
499 Asia region shows sub-regions with significantly decreasing TrC-NO<sub>2</sub>, others with significantly  
500 increasing TrC-NO<sub>2</sub>, and the rest with non-significant (positive and negative) trends. This figure  
501 allows us to quickly understand the distribution of the trends within this given region while the  
502 overall regional trend is given by the 50<sup>th</sup> percentile and the circles tagging each region. It's a  
503 regional summary of what is shown in the trend global map. In Eastern Asia, the area where  
504 trends are significantly positive is more extended than for the significant decrease (28% versus  
505 15%), but the trend values tend to be smaller (at least when comparing the 50th percentiles, -0.05  
506 versus +0.01 Pmolec/cm<sup>2</sup>/yr). The map of regions is included in the supplement. Canada is  
507 included in northern America but as shown in the trend map, most of Canada does not have OMI  
508 data

509 Over continental areas, significant positive and negative trends are found in about 15-  
510 20% of the grid cells each (Figure 12). Regions with predominantly decreasing TrC-NO<sub>2</sub> include  
511 western and southern Europe (where about 50-60% of cells with a significant decrease), northern  
512 America (40% of cells with a significant decrease, mostly located in the eastern United States),  
513 Japan, and Indonesia. In absolute terms, these negative trends reach values of about -0.03  
514 Pmolec/cm<sup>2</sup>/yr. Specific eastern regions of China also show similar significant TrC-NO<sub>2</sub>  
515 decreases but overall, a larger part of the country faces increasing trends up to +0.03  
516 Pmolec/cm<sup>2</sup>/yr. Positive trends of similar magnitude are observed over most of India, as well as  
517 in specific parts of south-eastern Asia (mainly Vietnam) and the Middle East (mainly Iran and  
518 Iraq). Conversely, TrC-NO<sub>2</sub> trends in Africa and South America remain mainly insignificant,  
519 except in a few specific regions with significant increases (e.g. South Africa, Chile, Morocco,  
520 and parts of Brazil).

521 The trends in NO<sub>2</sub> have varying effects on the tropospheric ozone column, which is related  
522 to the different local chemistry in each region. The concomitant increase or decrease in TrC-O<sub>3</sub>  
523 and TrC-NO<sub>2</sub> trends over the eastern US, and central Europe is due to the dominant NO-sensitive  
524 condition due to the strict NO<sub>x</sub> control measures that were applied over the last two decades. The  
525 decreasing trend of TrC-NO<sub>2</sub> but increasing trend of TrC-O<sub>3</sub> in some regions in the central US,  
526 e.g., over Chicago is due to the high NO<sub>x</sub> conditions in these regions (e.g., Elshorbany et al., 2021  
527 and references therein). The increasing TrC-O<sub>3</sub> trends as TrC-NO<sub>2</sub> decreases over China and parts  
528 of eastern Asia can also be explained by the high NO<sub>x</sub> levels dominated in these regions.  
529



530



531

532 Figure 13: Summary of the statistically significant and insignificant regional trends of OMI NO<sub>2</sub>  
 533 tropospheric column (TrC-NO<sub>2</sub>) trends over 2005-2019, at a 95% confidence level (see text for  
 534 details on the calculation of the trends). For each region, the trend on the bars is in the format:  
 535 p50 [p5; p95], which represents the 50<sup>th</sup>[5<sup>th</sup>, and 95<sup>th</sup>] percentiles of the trends.

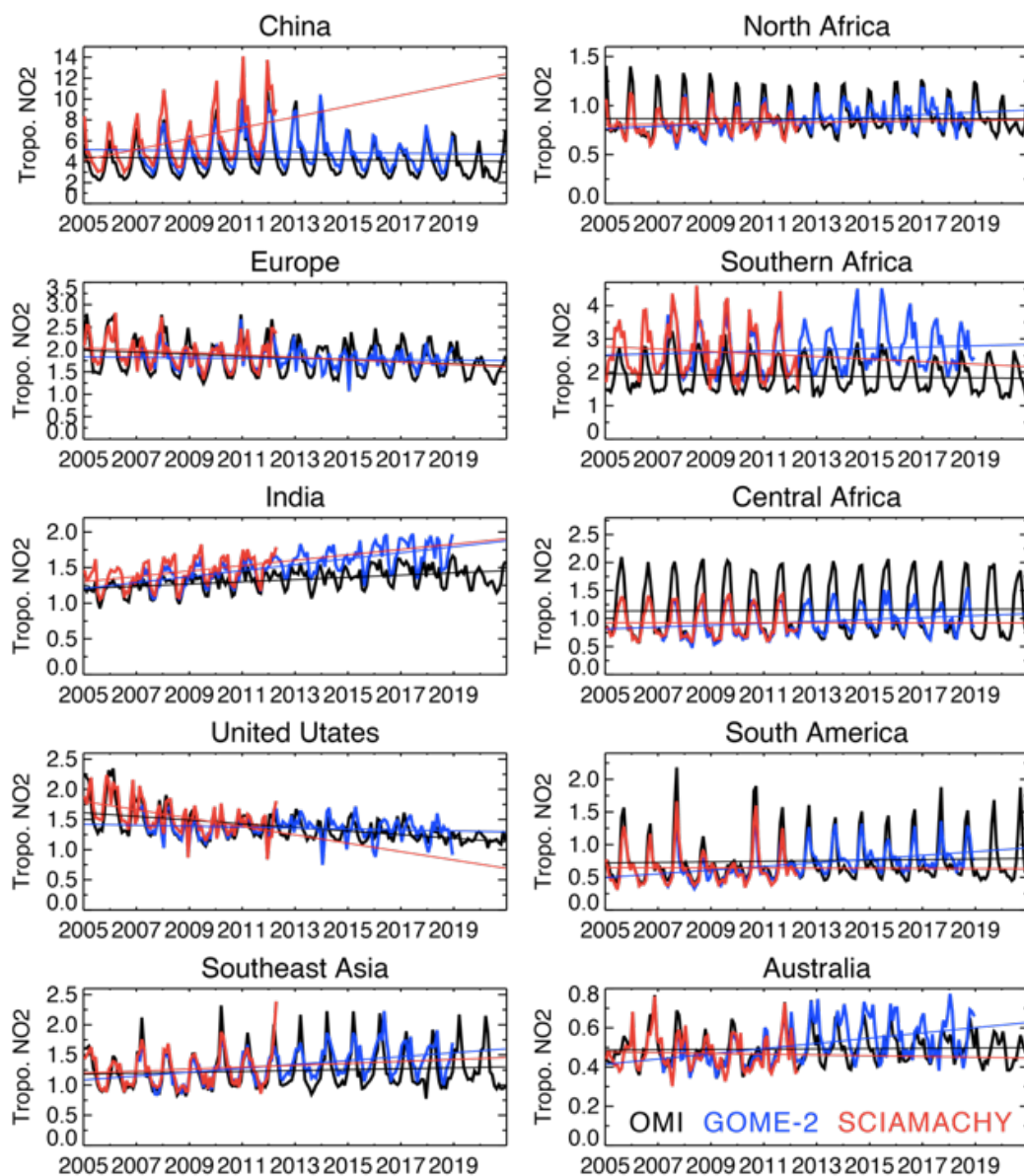
536

537 Figure 14 shows the time series of regional mean tropospheric NO<sub>2</sub> concentrations from three  
 538 satellite instruments, OMI for 2005-2020, GOME-2 for 2007-2018, and SCIAMACHY for 2005-  
 539 2012. All the instruments exhibit common large seasonal and year-to-year variations over both  
 540 industrial regions and biomass-burning areas. Slight systematic differences among the instruments  
 541 can mainly be attributed to the different overpass times. The satellite observations show positive  
 542 trends over China by 2010, followed by a continued decrease. Over the USA and Europe, all the  
 543 retrievals show a downward trend over the analysis period. Over the US, the observed TrC-NO<sub>2</sub>





544 decreased rapidly during 2005–2009 and subsequently show weaker reductions, as discussed by  
 545 Jiang et al. (2018). A similar slowdown trend is found in Europe. Over India, the OMI observations  
 546 show positive trends over the 14 years (+1.6 % yr<sup>-1</sup>). The seasonal and year-to-year variations over  
 547 Southeast Asia and northern and central Africa are associated with changes in biomass-burning  
 548 activity.  
 549



550

551 Figure 14: Time series of regional monthly mean tropospheric NO<sub>2</sub> columns (in 10<sup>15</sup> molecules  
 552 cm<sup>-2</sup>) averaged over China (110–123° E, 30–40° N), Europe (10° W–30° E, 35–60° N), the US  
 553 (70–125° W, 28–50° N), India (68–89° E, 8–33° N), South America (50–70° W, 20° S–Equator),

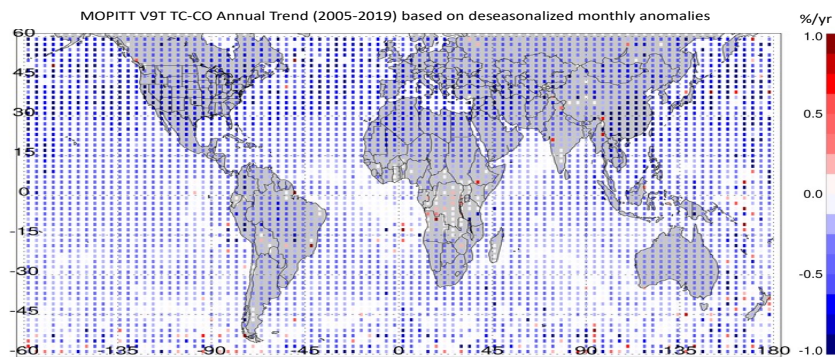




554 northern Africa (20° W–40° E, Equator–20° N), central Africa (10–40° E, Equator–20° S),  
555 southern Africa (25–34° E, 22–31° S), southeastern Asia (96–105° E, 10–20° N), and Australia  
556 (113–155° E, 11–44° S) obtained from OMI (black), GOME-2 (blue), and SCIAMACHY (red).

### 557 3.4.5. Carbon Monoxide

558 CO trends are calculated based on MOPITT v9 products (adapted from Buchholz et al. (2021),  
559 see sec. 2.2.1). Observed CO trends below show a slowing in the trend compared to the previous  
560 analysis (Buchholz et al. (2021)). In the northern hemisphere, CO trends are largely negative over  
561 the US and Europe, which is consistent with the implemented policies to reduce air pollution  
562 since 2005. Except for small sporadic positive trends, no significant trends can be calculated over  
563 Central Asia (India and China), while there is a strong negative trend in East China due to recent  
564 strong focus on air quality improvement, and no significant trend in the SH (relative to slope  
565 error).



566  
567 Figure 15: Trends in TC CO from MOPITT V9T data, 2005-2019. Trends are computed from  
568 deseasonalized monthly anomalies.

569  
570 Calculated global CO trends are driven mainly by the decreasing trends in the NH. Shown below  
571 are the trends in the MOPITT column average volume mixing ratio (VMR) anomalies from 2005  
572 to 2019 (Figure 16) using QR as well as Weighted least squares (WLS)) as Buchholz et al.  
573 (2021). The region boundaries are the same as used in Fig. 10 and 11. Results show a significant  
574 decreasing trend in the NH ( $-0.35 \pm 0.1\%$  annually), a smaller decreasing trend in the Mid-  
575 latitudes ( $-0.26 \pm 0.1\%$  annually) and no significant trend in the SH ( $-0.14 \pm 0.1\%$  annually). The  
576 three anthropogenic regions investigated in the NH all show strong decreases in CO. The larger  
577 negative trend over Australia ( $-0.2 \pm 0.1\%$  annually) than the average SH, suggests sources from  
578 the other two land regions (Southern Africa and South America) may be counteracting negative  
579 trends in CO for the SH.

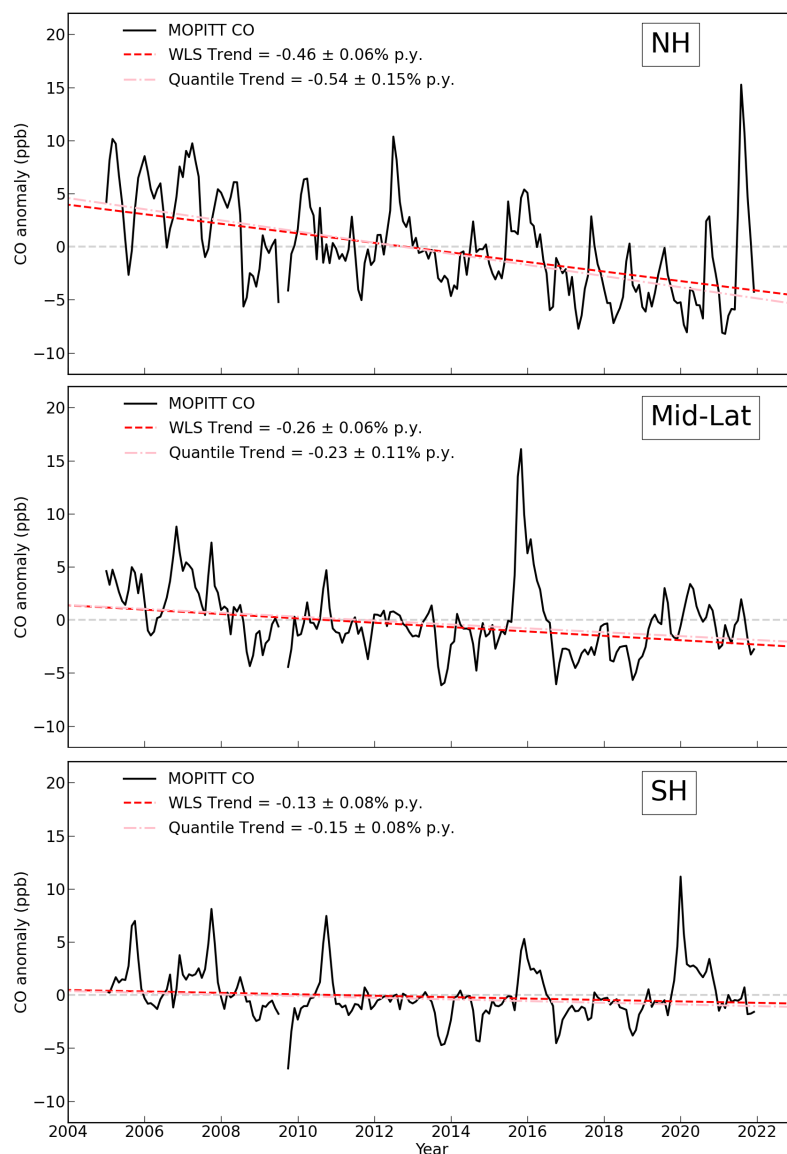
580 We also compare CO trends with Community Earth System Model (CESM) simulations  
581 (Supplement Fig S1). While the magnitude of modeled CO tends to be underestimated relative to  
582 observations, the anomalies between model and measurements are comparable, indicating the  
583 model reproduces interannual variability well. The negative trends in the NH are also reproduced  
584 by CESM, although to a smaller degree than observations, suggesting that the trends in sources  
585 or loss processes (such as OH oxidation) are underestimated in the model. These processes will  
586 impact the feedback into modeled ozone and the resulting interpretation of driving factors for  
587 ozone abundance and variability. Interestingly, CESM correctly represents a negative trend in



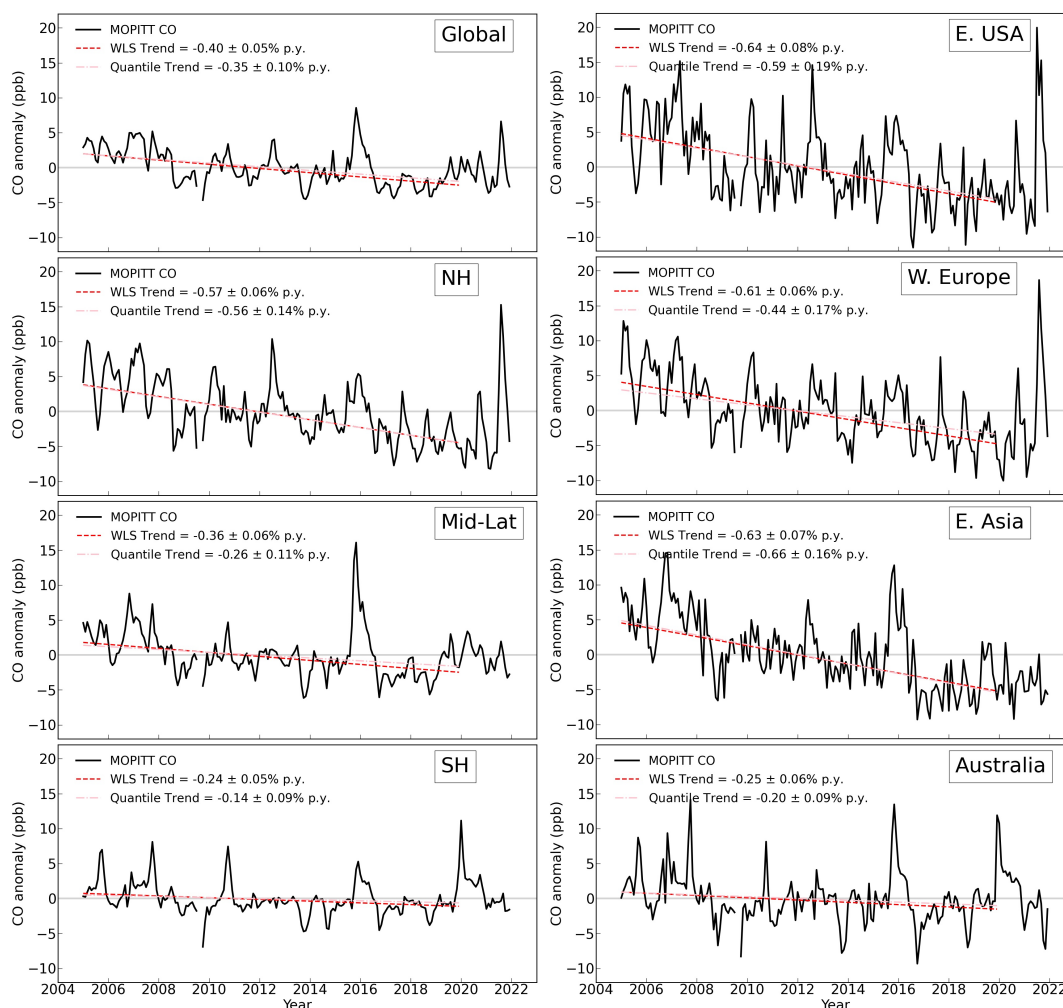
588 CO for the NH and East Asia while GEOS GMI has a positive CO trend in those regions (Fig.  
589 11), likely due to the well-known misrepresentation of East Asia air quality improvements in  
590 models (Yin et al, 2015; Strode et al., 2016; Zheng et al, 2019). In the SH, CESM does not  
591 predict significant trends.

592

593



594



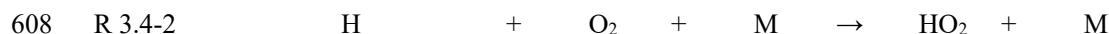
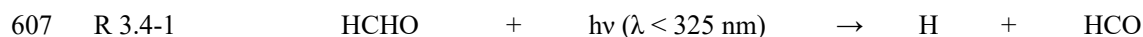
595

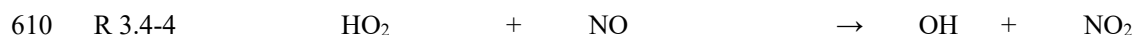
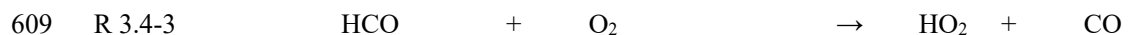
596 Figure 16: MOPITT monthly average CO anomalies in column average volume mixing ratio  
 597 (VMR, ppb), 2005-2021 (black). Updated dataset based on Buchholz et al. (2021). Data is Level  
 598 3, monthly average daytime observations, using version 9 joint NIR/TIR retrievals (V9J).  
 599 Regions are defined in Figure 10 and Figure 11. Trends are calculated on anomalies 2005-2019.  
 600 The weighted Least Squares trend (red) is weighted by the monthly regional standard deviation.  
 601 The quantile regression trend is also shown (pink). Grey dashed lines indicate a zero trend.

602

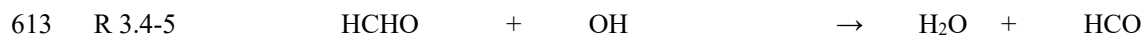
### 603 3.4.6. HCHO Trends

604 HCHO, mainly a photochemical product results from hydrocarbon oxidation. HCHO is itself a  
 605 source of OH and ozone through its photolysis producing HO<sub>2</sub>, which can be recycled back to  
 606 OH if sufficient NO levels are present.





611 Unlike higher aldehydes, the OH reaction with HCHO leads also to the formation of a formyl  
612 radical (HCO), which ultimately forms HO<sub>2</sub> (R 3.4-3).

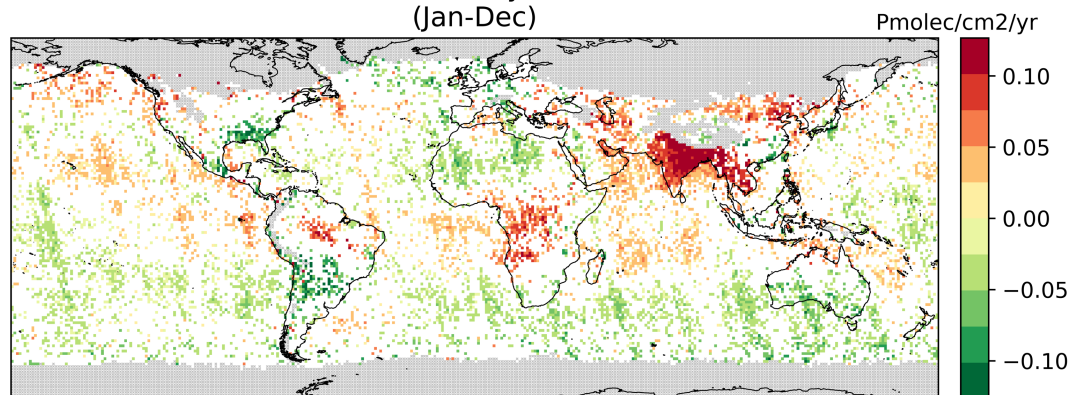


614 Due to its solubility, the variability of HCHO also depends on the presence of clouds, and wet  
615 deposition ultimately represents another important sink for HCHO (Lelieveld and Crutzen, 1991).  
616 Overall, HCHO plays a key role in the O<sub>3</sub> budget, both in polluted and remote regions.

617 Trends of the OMI HCHO tropospheric columns (hereafter referred to as TrC-HCHO) are  
618 computed as described for OMI TrC-NO<sub>2</sub>. TrC-HCHO trends over 2005-2019 are shown in  
619 Figure 17 with a regional summary in Figure 18. The first global feature to highlight on the  
620 global trends map is the presence of stripes along the OMI orbits. The number of rows affected  
621 by the OMI row anomaly has increased over the years (Boersma et al., 2018). The affected rows  
622 are filtered out in the HCHO data, but the change in the sampling and the related increase in the  
623 noise impact the trend analysis. Along orbit stripes in the trend analysis should be ignored but  
624 zonal trends are still valid (Figure 17).

625

Annual trend of OMI TrC-HCHO  
(based on monthly anomalies)  
(Jan-Dec)



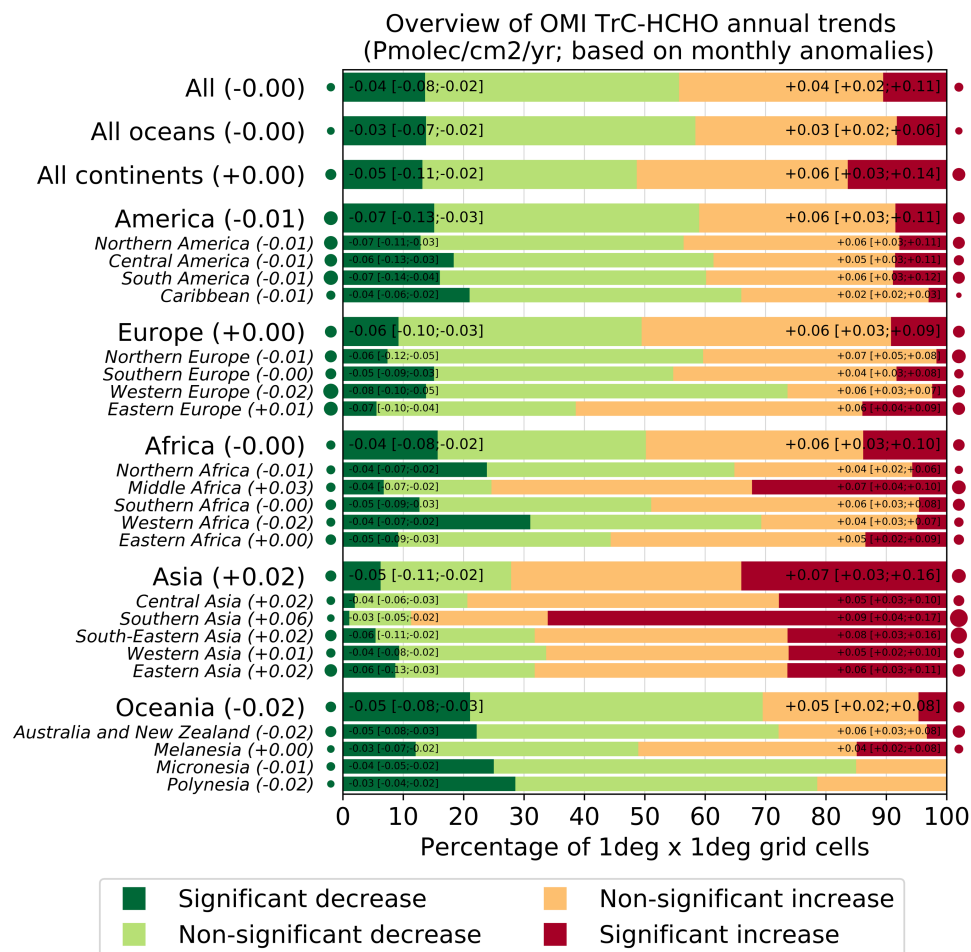
626

627 Figure 17: Global trends of OMI HCHO tropospheric column (TrC-HCHO) over 2005-2019 (see  
628 text for details on the calculation of the trends). Grey areas correspond to areas without enough  
629 data, white areas correspond to regions where the trends remain statistically insignificant at a  
630 95% confidence level.

631 Despite the fact that TrC-HCHO trends remain insignificant over a large part of the globe,  
632 specific regions do highlight clear trends. The region with clearest changes is unambiguously  
633 southern Asia where about 65% of the cells show increasing trends with a median of +0.09  
634 Pmolec/cm<sup>2</sup>/yr. The other regions with a large portion (25-30% of the cells) of increasing trends  
635 include the rest of Asia and Middle Africa, with median TrC-HCHO trends ranging between  
636 +0.05 and +0.08 Pmolec/cm<sup>2</sup>/yr, as well as some parts of central Brazil (Amazonians).  
637 Conversely, some significant decreases of TrC-HCHO are observed in the south-eastern US, the  
638 southern half of Southern America, North and western Africa, and southern Australia, although  
639 part of them overlap with the aforementioned stripes and might thus not be real.



640



641

642 Figure 18: Summary of the statistically significant and insignificant regional trends of OMI  
 643 HCHO tropospheric column (TrC-HCHO) trends over 2005-2019, at a 95% confidence level  
 644 (see text for details on the calculation of the trends). For each region, the trends reported on the  
 645 left (resp. right) represent the 5<sup>th</sup>, 50<sup>th</sup> and 95<sup>th</sup> percentiles of the trends calculated over the  
 646 different grid cells showing a significant TrC-HCHO increase or decrease.

647

648 HCHO trends are consistent with that of O<sub>3</sub> (sec. 3.4.1). O<sub>3</sub> and HCHO trends are consistent with  
 649 NO<sub>2</sub> over Eastern US and Europe. However, NO<sub>2</sub> trends are decreasing over the northern coast  
 650 of Australia while that of O<sub>3</sub> and HCHO are increasing. Similarly, while NO<sub>2</sub> trends are slightly  
 651 increasing over southern Australia, trends of O<sub>3</sub> and HCHO were decreasing. The decreasing  
 652 trends of HCHO and O<sub>3</sub> as NO<sub>2</sub> increases is evidence of the VOC-limited conditions in these  
 653 regions. Under these conditions, increased NO<sub>2</sub> levels lead to a reduction of OH via  
 654 OH+NO<sub>2</sub>=HNO<sub>3</sub>, which decreases the oxidation capacity and thus lowers the photochemical  
 655 formation of HCHO and O<sub>3</sub>.

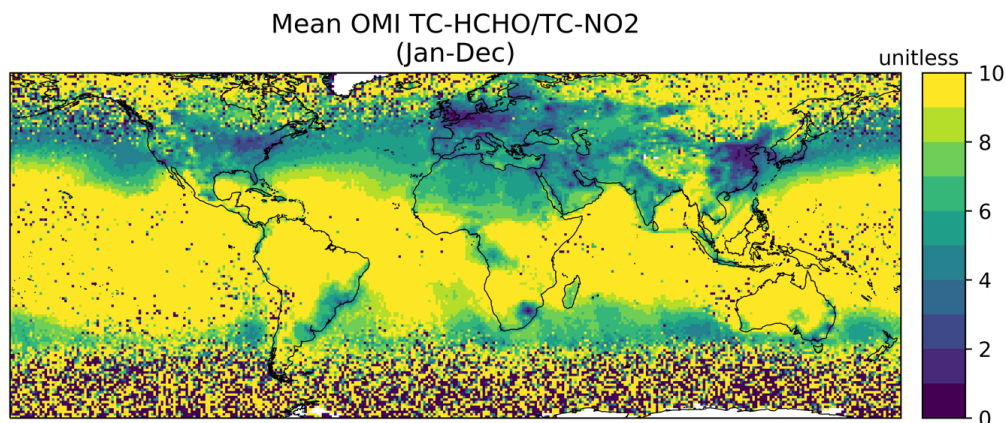
656





657 **3.4.7. HCHO/NO<sub>2</sub>**

658 Since the pioneer study of Martin et al. (2004), the ratio of TrC-HCHO/NO<sub>2</sub> observed from space  
 659 has been used in a number of studies to give insights on the O<sub>3</sub> chemical regime, higher (resp.  
 660 lower) TrC-HCHO/NO<sub>2</sub> ratios coming with more NO<sub>x</sub>-limited (resp. RO<sub>x</sub>-limited) regimes.  
 661 Although imperfect (e.g. Souri et al., 2023), this indicator yet provides some qualitative  
 662 information on the evolution of the O<sub>3</sub> regime over the last years. The mean TrC-HCHO/NO<sub>2</sub> over  
 663 2005-2019 are shown in Figure 19, and the trend results in Figure 20 with a regional summary in  
 664 Figure 21. The highest ratios are observed in the tropical regions due to strong TrC-HCHO due to  
 665 high biogenic and fire NMVOC emissions in tropical South America and Africa combined with  
 666 relatively low TrC-NO<sub>2</sub>. Conversely, lower TrC-HCHO/NO<sub>2</sub> ratios are observed across western  
 667 Europe and north-eastern Asia, and to a lesser extent north-eastern US.  
 668



669 Figure 19: Global mean OMI HCHO/NO<sub>2</sub> tropospheric column ratio over 2005-2019.  
 670  
 671

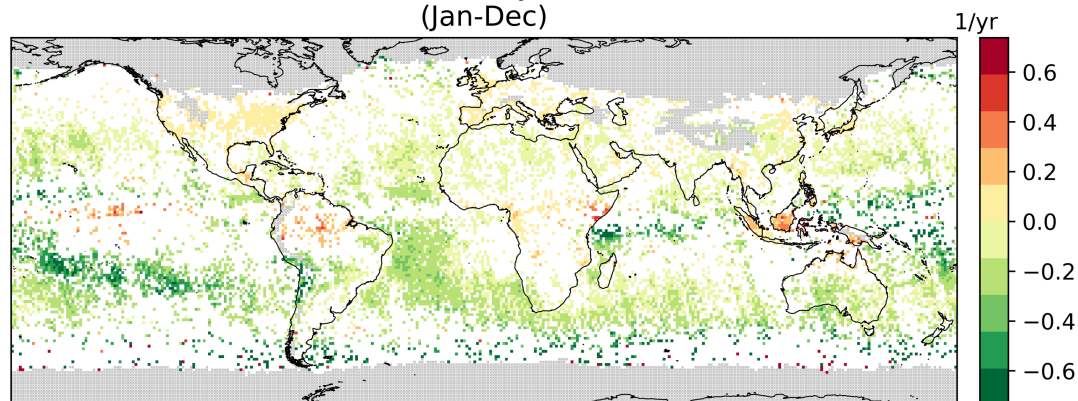
672 At a global scale, the significant changes in TrC-HCHO/ TrC-NO<sub>2</sub> ratios mostly go in the  
 673 direction of a reduction, with about 25% of the grid cells showing a median trend of -0.52 yr<sup>-1</sup>.  
 674 (while only 5% of the cells show a significant increase of +0.03 yr<sup>-1</sup>). This suggests that these  
 675 areas are evolving toward more NO<sub>x</sub>-sensitive conditions (which does not necessarily imply that  
 676 they are already in this regime). This situation is observed over a large part of Oceania  
 677 (especially Polynesia) and specific parts of Africa, Asia, and America. The opposite significant  
 678 trends, toward more RO<sub>x</sub>-sensitive conditions, are mainly observed over Europe and northern  
 679 America, as well as south-eastern Asia.

680





Annual trend of OMI TrC-HCHO/NO<sub>2</sub>  
(based on monthly anomalies)  
(Jan-Dec)



681

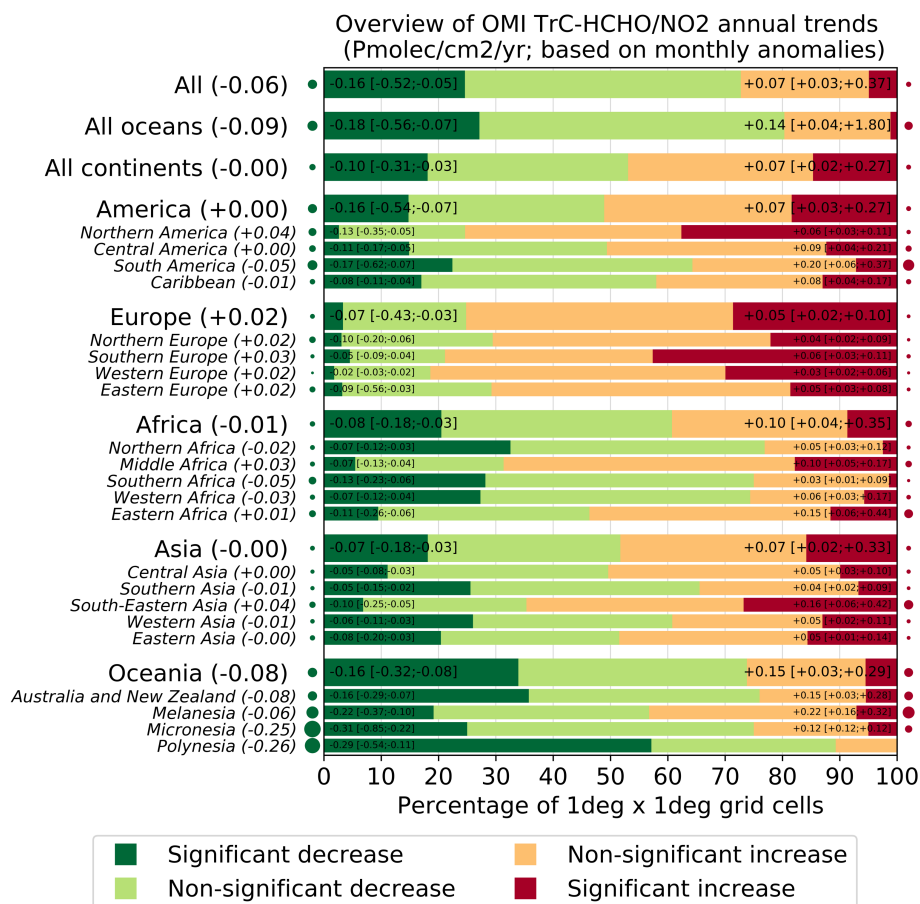
682 Figure 20: Global trends of OMI HCHO/NO<sub>2</sub> tropospheric column ratio over 2005-2019 (see  
683 text for details on the calculation of the trends). Grey areas correspond to areas without enough  
684 data, white areas correspond to regions where the trends remain statistically insignificant at a  
685 95% confidence level.

686

687 These trends on the TrC-HCHO/ TrC-NO<sub>2</sub> ratio can be mainly driven by specific trends on TrC-  
688 HCHO and/or TrC-NO<sub>2</sub>, depending on the region. The increase in southern and western Europe  
689 and southeast Asia appears primarily due to decreasing TrC-NO<sub>2</sub>, since TrC-HCHO does not  
690 change significantly. Over North America, observed TrC-HCHO values do decrease but the less  
691 than TrC-NO<sub>2</sub>, which thus drives the ratio toward an increase. Conversely, the increase of TrC-  
692 TrC-HCHO/TrC-NO<sub>2</sub> in equatorial Africa and Amazonians appears mainly driven to increasing  
693 TrC-HCHO. Note that over the US, Jin et al. (2020) demonstrated the reasonable ability of the  
694 OMI-based TrC-HCHO/TrC-NO<sub>2</sub> trends to capture the transition from RO<sub>x</sub>-limited to NO<sub>x</sub>-limited  
695 regimes over main US cities and found a relatively good consistency between observed changes  
696 of the surface O<sub>3</sub> and space-based HCHO/NO<sub>2</sub> increasing trends. The regions where TrC-  
697 HCHO/TrC-NO<sub>2</sub> is significantly decreasing include southwestern America and Australia, due to  
698 both decreasing TrC-HCHO and increasing TrC-NO<sub>2</sub> (Figure 21).

699

700



701

702

703

704

705

706

Figure 21: Summary of the statistically significant and insignificant regional trends of OMI TrC-HCHO/TrC-NO<sub>2</sub> tropospheric column ratio trends over 2005-2019, at a 95% confidence level (see text for details on the calculation of the trends). For each region, the trends reported on the left (resp. right) represent the 5<sup>th</sup>, 50<sup>th</sup> and 95<sup>th</sup> percentiles of the trends calculated over the different grid cells showing a significant TrC-HCHO/TrC-NO<sub>2</sub> increase or decrease.

707

708



709

### 710 **3.5. Lightning NO<sub>x</sub> and Its Effects on NO<sub>x</sub> and Tropospheric O<sub>3</sub>**

711 Nitric oxide (NO) is produced in lightning flash channels and quickly comes into equilibrium with  
712 NO<sub>2</sub>. Cloud-scale simulations of thunderstorms indicate that 55-75% of lightning NO<sub>x</sub> (LNO<sub>x</sub>) is  
713 detrained above 8 km (Pickering et al., 1998) where it enhances upper tropospheric NO<sub>y</sub>, OH, and  
714 O<sub>3</sub> (Labrador et al., 2005; Allen et al., 2010; Liaskos et al., 2015) and contributes to positive  
715 radiative forcing by O<sub>3</sub> (Lacis et al., 1990; Finney et al., 2018) and negative radiative forcing by  
716 CH<sub>4</sub> (Fiore et al., 2006; Finney et al., 2018). The lifetime of NO<sub>x</sub> in the upper troposphere is  
717 controlled by the chemical cycling of NO<sub>x</sub> with reservoir species and is 10-20 days away from  
718 deep convection (Prather and Jacob, 1997) but only 2-12 hours in the vicinity of convection (Nault  
719 et al., 2016, 2017). This chemical recycling provides a source of NO<sub>x</sub>, which causes the ozone  
720 production efficiency of emitted NO<sub>x</sub> to be 4-20 times higher in the upper troposphere than at the  
721 surface. Thus, LNO<sub>x</sub> has a disproportionate impact on the tropospheric O<sub>3</sub> budget (Pickering et al.,  
722 1990; Grewe et al., 2001; Sauvage et al., 2007).

723 The distribution of lightning is fairly well known over much of the Earth due to remote  
724 sensing observations and an increase in the number and capability of ground-based lightning  
725 networks. However, the LNO<sub>x</sub> production efficiency (PE, mol fl<sup>-1</sup>) is a continued source of  
726 uncertainty. Schumann and Huntrieser (2007) reviewed the literature on LNO<sub>x</sub> production, finding  
727 a best estimate of 250 moles per flash, with uncertainty factors ranging from 0.13 to 2.7. The PE  
728 can be estimated from theoretical and laboratory considerations (Price et al., 1997; Koshak et al.,  
729 2014), using thunderstorm anvil observations by aircraft (Ridley et al., 2004; Huntrieser et al.,  
730 2008, 2011; Pollack et al., 2016; Nault et al., 2017; Allen et al., 2021a), based on satellite data  
731 (Bucsela et al., 2010; Beirle et al., 2010; Pickering et al., 2016; Bucsela et al., 2019; Lapierre et  
732 al., 2020; Zhang et al., 2020; Allen et al., 2019, 2021b), or using cloud-resolved (e.g., DeCaria et  
733 al., 2000; 2005; Fehr et al., 2004; Ott et al., 2007, 2010; Cummings et al., 2013; Pickering et al.,  
734 2023) or global model simulations with chemistry (e.g. Martin, et al., 2007; Murray et al., 2012;  
735 Miyazaki et al., 2014; Marais et al., 2018). Miyazaki et al. (2014) assimilated OMI NO<sub>2</sub>, MLS and  
736 TES O<sub>3</sub>, and MOPITT CO into a chemical transport model to provide comprehensive constraints  
737 on the global LNO<sub>x</sub> source, resulting in an estimate of mean PE of 310 moles per flash. Marais et  
738 al. (2018) used cloud-sliced upper tropospheric NO<sub>2</sub> from OMI together with the GEOS-Chem  
739 model to estimate a mean LNO<sub>x</sub> PE of 280 moles per flash.

740 LNO<sub>x</sub> impacts air quality and deposition (Kaynak et al., 2008; Allen et al., 2012). On  
741 average LNO<sub>x</sub> adds 1-2 ppbv to surface O<sub>3</sub> (Kang et al., 2019b), although contributions as large as  
742 18 ppbv have been seen for individual events (Murray et al., 2016). Allen et al. found that the  
743 addition of LNO<sub>x</sub> to the Community Multiscale Air Quality (CMAQ) model increased wet  
744 deposition of oxidized nitrogen at National Atmospheric Deposition Program (NADP) sites by  
745 43%, reducing low biases from 33% to near-zero. Kang et al. (2019b) found similar improvements  
746 for wet deposition and also found that including LNO<sub>x</sub> resulted in smaller biases with respect to  
747 ozonesondes and aircraft profiles taken during the NASA DISCOVER-AQ field campaign (Flynn  
748 et al., 2016). Thus, to accurately assess its impacts on air quality, it is critical that LNO<sub>x</sub>-producing  
749 deep convection is accurately simulated.

750 Lightning is the dominant source of NO<sub>x</sub> in the tropical upper troposphere year-round and  
751 in the northern mid-latitudes in summer. Lightning is responsible for 10-15% of NO<sub>x</sub> emissions  
752 globally. This is 2 – 8 Tg N a<sup>-1</sup> (Schumann and Huntrieser, 2007; Verma et al., 2021) or 100 to  
753 400 mol per flash. Much of the uncertainty stems from limited knowledge of lightning NO<sub>x</sub> PE per  
754 flash or per unit flash length. Most LNO<sub>x</sub> is injected into the mid- and upper-troposphere where



755 (away from deep convection) its lifetime is longer relative to lower troposphere  $\text{NO}_x$ .  $\text{LNO}_x$  plays  
756 an important role in determining mid- and upper-tropospheric concentrations of the hydroxyl  
757 radical (OH), the atmosphere's cleanser;  $\text{CH}_4$ , an especially potent greenhouse gas; and  $\text{O}_3$ , a  
758 greenhouse gas and pollutant.

759 Only in recent years with the advent of satellite observations of lightning flashes and improved  
760 coverage by ground-based lightning networks has there been sufficient data to make estimates of  
761 trends in the occurrence of lightning. However, it is unknown whether trends in  $\text{LNO}_x$  production  
762 are similar to those of lightning itself. Lightning characteristics such as the ratio of intracloud (IC)  
763 flashes to cloud-to-ground (CG) flashes, the multiplicity (i.e., the number of strokes per flash), and  
764 the peak current or energy associated with flashes may vary over time. All of these lightning  
765 characteristics may have effects on the magnitude of  $\text{LNO}_x$  production. We have insufficient data  
766 to take into account these possible effects on  $\text{LNO}_x$  production over large spatial domains or over  
767 sufficiently long periods of time.

### 768 **3.5.1. Global Historical trends of $\text{LNO}_x$**

769 The first attempts at an examination of trends in thunderstorm activity were conducted in terms of  
770 thunder-days (in Japan by Kitagawa et al., 1989; in Brazil by Pinto et al., 2013). A more recent  
771 global analysis was conducted by Lavigne et al. (2019), who analyzed trends in thunder-days  
772 (number of days with audible thunder at weather observation stations) over 43 years and in flashes  
773 recorded by the Lightning Imaging Sensor (LIS) on the Tropical Rainfall Measuring Mission  
774 (TRMM) for 16 years. Thunder-days increased since the 1970s in the Amazon Basin, the Maritime  
775 Continent, India, Congo, Central America, and Argentina. Decreases in thunder-days were found  
776 in China, Australia, and the Sahel region of Africa. How well do thunder-days represent lightning  
777 flash rate? Lavigne et al. found a positive correlation between thunder-days and LIS flash rates in  
778 China, the Maritime Continent, South Africa and Argentina, but disagreement on the trend in India  
779 and West Africa.

780 Large-scale ( $\pm 38^\circ$  latitude) trends in lightning flashes have been examined in the data collected by  
781 the LIS on the TRMM satellite (January 1998 – December 2014) and on the International Space  
782 Station (February 2017 – December 2021). Füllekrug et al. (2022; see Figure SB2.1b) demonstrate  
783 that the annual mean deviations from the 1998 – 2021 mean are no more than  $\sim 5\%$  except for  $\sim$   
784  $10\%$  in 2020 and  $\sim 8\%$  in 2021. The possibility that these larger negative deviations in 2020 and  
785 2021 are due to Covid-19 lockdowns and general declines in economic activity has been  
786 speculated. The link may be provided by changes in Aerosol Optical Depth (AOD) as suggested  
787 by Liu et al. (2021) who demonstrated 10-20% flash reductions in March – May 2020 relative to  
788 the 2018 – 2021 mean for those months from the GLD360 and WLLN ground-based lightning  
789 networks. Regional lightning reductions were consistent with AOD reductions noted by Sanap  
790 (2021). Larger reductions in lightning were noted over Africa/Europe and Asia/Maritime  
791 Continent and lesser reductions over the Americas.

### 792 **3.5.2. Regional Historical Trends of $\text{LNO}_x$**

793 Widely varying trends in lightning over China have been reported in the literature. To some extent,  
794 whether the trend in lightning is upward or downward depends on the particular region studied and  
795 on the period of time considered. Yang and Li (2014) were the first to report on lightning trends  
796 in China. They used lightning data from the TRMM/LIS sensor and human-observed thunderstorm  
797 day occurrence over the period 1990 to 2012 in southeastern China. Thunderstorms and lightning  
798 occurrence increased over the period as well as LIS precipitation radar echo tops heights. These  
799 increases were accompanied by decreases in visibility, indicating increases in pollution aerosol.



800 Detailed work on lightning trends in China has been performed in relation to aerosols. Shi et al.  
801 (2020) correlated flashes from the TRMM/LIS Low-Resolution Monthly Time Series (2.5 deg.  
802 resolution) with AOD from MODIS-Terra V6.1 Level 3 over the period 2001 to 2014. For AOD  
803  $< 1.0$ ,  $r = 0.64$ , indicating a likely microphysical effect on lightning flash rate. For AOD  $> 1.0$ ,  $r =$   
804  $-0.06$ , which could indicate that with higher aerosol concentration there is a radiation effect  
805 stabilizing the atmosphere and/or a decrease in the number of graupel particles in the mixed-phase  
806 region of the storms that is important for charging. Flashes were also correlated with surface  
807 relative humidity and Convective Available Potential Energy (CAPE). As AOD generally  
808 increased over much of the early portion of this time period and then decreased, lightning flash  
809 rates followed similar trends. Wang et al. (2021) examined a 9-year record (2010- 2018) of CG  
810 lightning from the China Lightning Detection Network in three polluted urban areas of China  
811 (Chengdu, Wuhan, and Jinan). They found decreasing trends (see Wang et al., 2021) in CG  
812 lightning and total AOD (from the MERRA-2 reanalysis). Annual mean lightning density in these  
813 three regions decreased by 50 – 75% as annual mean AOD fell from 0.70 – 0.75 to 0.53 to 0.62.

814 Qie et al. (2022) analyzed the OTD/LIS record from 1996 through 2013, and found that lightning  
815 increased over the eastern Tibetan Plateau by  $0.072 \pm .069$  fl  $\text{km}^2 \text{ yr}^{-1}$ . Over the 18 years, this  
816 increase amounted to a total of  $1.3$  fl  $\text{km}^2 \text{ yr}^{-1}$ , compared with a climatological value of  $7.7$  fl  $\text{km}^2$   
817  $\text{yr}^{-1}$ , thereby indicating a significant increase. The ground-based World Wide Lightning Location  
818 Network (WWLLN) also showed an increase in strokes in this region. The increase in lightning  
819 frequency in this region was found to be due to an increase in thunderstorm frequency, and not  
820 due to increased storm intensity. Xue et al. (2021) found a highly significant downward trend of  
821 thunder and lightning days observed at surface weather stations in China between 1961 and 2013,  
822 particularly in the warm season. The decrease amounted to 6.5 days per decade, averaged over  
823 mainland China. Factors thought to be contributing to this decrease include a decrease in the north-  
824 south geopotential height gradient, weakening of the westerly jet stream, decreased relative  
825 humidity in the lower troposphere and a decrease in the vertical wind shear between the surface  
826 and 6 km altitude.

827 Koshak et al. (2015) analyzed National Lightning Detection Network (NLDN) CG flashes over  
828 the contiguous United States (CONUS) from 2003 to 2012. The five-year mean flashes over 2008  
829 to 2012 decreased by 12.8% from the five-year mean for 2003 to 2007 (Table 1). The CONUS  
830 average wet bulb temperature also trended downward during this period, which may have led to  
831 lesser or weaker storms. However, US Environmental Protection Agency air quality trends show  
832 an 18% decrease in PM<sub>2.5</sub> concentrations over CONUS between the two subperiods, which also  
833 could have had an influence on the flash rates. The decrease in CG flashes was slightly larger  
834 (14.8%) over the region of CONUS south of 38 deg. N latitude. However, the TRMM/LIS  
835 instrument, which detects both CG and IC flashes, showed little change in flashes over the period  
836 of interest south of 38 degrees, suggesting that perhaps the number of IC flashes increased in this  
837 region. A recent effort to update the Koshak et al. (2015) analysis is underway. NLDN flashes  
838 have been reprocessed (Kenneth Cummins, personal communication) from 2015 through 2021 to  
839 ensure that the classification of IC and CG flashes is done consistently with data prior to 2015.  
840 Trend analysis of NLDN CG flashes from 2003 (a major upgrade of the NLDN network hardware)  
841 through 2022 (William Koshak, personal communication) shows a significant reduction in CG  
842 flashes over CONUS, comparing the mean CG flashes over 2003-2004 with the mean over 2021 -  
843 2022. Within this period a major decrease (~25%) in CONUS CG flashes occurred from 2011 to  
844 2012. Flashes in 2013 remained low, but recovered by 2014-2015. A major decrease (~27%)  
845 occurred from 2019 to 2020, with a small increase in 2021. These results have been obtained from  
846 ongoing efforts by Dr. William Koshak of the NASA Marshall Space Flight Center, and are





847 presently part of a draft manuscript by lead author Koshak that extends and refines the earlier work  
848 in Koshak et al. (2015). Details concerning these trends will be contained in that manuscript.

849 A possible contributing factor to the CONUS decline in CG flashes over 2003 to 2021 is the  
850 substantial decrease in aerosol. Surface annual average PM<sub>2.5</sub> concentrations averaged over  
851 CONUS decreased by 37% from 2000 to 2021 according to the EPA National Air Quality Trends  
852 Report (<https://www.epa.gov/air-trends/air-quality-national-summary>). However, no decrease in  
853 CONUS annual average PM<sub>2.5</sub> was seen from 2019 to 2020. As mentioned previously, AOD may  
854 be a better indicator of the aerosol amount that may become incorporated into thunderstorm clouds.  
855 Sanap (2021) showed negative anomalies of AOD of ~0.1 in portions of CONUS in March and  
856 April 2020 and 0.1 to 0.2 in May 2020. The major decrease in CONUS CG flashes from 2011 to  
857 2012 has been related to drought conditions during Summer 2012 over the South Central and  
858 Southeastern US (Koshak et al., 2015). The reason for the number of CONUS flashes remaining  
859 lower in 2013 is uncertain. Koehler (2020) analyzed 26 years (1993 – 2018) of NLDN CG  
860 lightning data to construct a thunder-day climatology for CONUS. Positive anomalies from the  
861 26-year mean were found from Texas to Colorado during 2003 to 2007, and negative anomalies  
862 in this region during 2008 to 2012. These anomalies were consistent with precipitation anomalies  
863 associated with ENSO.

864

865 Table 1. The 5-year flash counts and associated percent changes over CONUS. From Koshak et  
866 al. (2015).

Period	NLDN	NLDN (up to 38°N)	LIS (raw)	LIS (corrected*)
2003 - 2007	25,204,345.8	15,931,940.6	92,655.0	46,997,805.4
2008-2012	21,986,578.8	13,574,876.0	92,659.4	47,175,192.4
Change (%)	-12.77	-14.79	0.005	0.38

867 \*Corrected for detection efficiency and view time

868

869

870 Holzworth et al. (2021) analyzed primarily CG lightning data from WWLLN for June, July, and  
871 August for the years 2010 through 2020. The ratio of lightning strokes north of 65° N latitude to  
872 the total global strokes increased by a factor of three over this period. This increase occurred as  
873 the surface temperature anomaly in this region increased by 0.3°C (see Holzworth et al., 2021).  
874 These results suggest a substantial increase in upper tropospheric NO<sub>x</sub> and subsequent ozone  
875 production at high northern latitudes.

876

### 877 3.5.3. Future LNO<sub>x</sub> trends

878 Price (2013) discusses an apparent paradox concerning lightning in future climate. On one hand  
879 increased tropical convection will transport more water vapor to the upper troposphere where it is  
880 a strong greenhouse gas, causing further warming of the upper troposphere and stabilization of the  
881 tropical atmosphere, leading to less lightning. On the other hand, in the current climate as CAPE  
882 increases, lightning increases. However, higher latitudes are warming more rapidly, decreasing the  
883 north-south temperature gradient, acting to suppress mid-latitude storms. Hence, there is large  
884 uncertainty concerning future lightning trends.

885 Parameterizations in global chemistry and climate models have been developed for  
886 lightning flash rate. These schemes typically use kinematic, thermodynamic or microphysical  
887 variables from the model as predictors. In some studies such predictors have simply been applied





888 to output from multiple climate models. This is the case with the Romps et al. (2014) work, which  
889 showed that when a lightning parameterization scheme using CAPE x Precipitation Rate is applied  
890 to 11 climate models an increase in CG lightning by 12 +/- 5% per degree Celsius of climate  
891 warming was computed. This work simply used the 12-hour resolution time series of spatial means  
892 of these variables over CONUS as input. Changes in IC lightning flashes were not considered. IC  
893 flashes typically outnumber CG flashes by a factor of 3 averaged over CONUS. Therefore, the  
894 result of this work is unknown with respect to the amount of change in LNO<sub>x</sub> emission. Romps et  
895 al. (2018) updated their analysis using CAPE from 3-hourly North American Regional Reanalysis  
896 (NARR) data and hourly precipitation from NOAA River Forecast Centers, finding that CAPE x  
897 Precipitation Rate captures the spatial, seasonal, and diurnal variations of NLDN CG flash rate  
898 over land, but does not predict the pronounced land-ocean contrast in flash rates. Therefore, these  
899 analyses are of limited value in estimating trends of LNO<sub>x</sub> over broader-scale regions. Romps et  
900 al (2019) tested four lightning proxies in a cloud-resolved 4-km resolution simulation over  
901 CONUS with the Weather Research and Forecasting (WRF) model, and over the tropical oceans  
902 with a Radiative Convective Equilibrium model. The proxies were CAPE x Precipitation Rate,  
903 precipitation with vertical velocity > 10 m/s, vertical ice flux at the 260K isotherm, and vertical  
904 integral of cloud ice and graupel product. The fractional change in proxy values per 1 degree  
905 Celsius of warming over CONUS was +8 to +16%. Over the tropical oceans the changes in proxy  
906 values per degree ranged from +12% for CAPE x Precipitation Rate to -1% for ice flux and -3%  
907 for the cloud ice and graupel product. Therefore, over broad regions of the Earth, there is great  
908 uncertainty on future trends in lightning.

909 Finney et al. (2016; 2018) compared lightning projections for 2100 using vertical ice flux  
910 (Finney et al., 2014) and cloud-top height parameterizations for flash rate in the UK Chemistry  
911 and Aerosols Model. They obtained -15% global change in total flash rate with ice flux under a  
912 strong global warming scenario (see Finney et al., 2018), which was composed of a greater  
913 decrease in the tropics and small increases in mid-latitudes. In terms of LNO<sub>x</sub> emissions this work  
914 using the ice flux scheme produced -0.15 TgN K<sup>-1</sup> change over the years from 2000 to 2100,  
915 implying less O<sub>3</sub> production. With the cloud-top height scheme they obtained +0.44 TgN K<sup>-1</sup> LNO<sub>x</sub>  
916 change, implying increased O<sub>3</sub> production. However, the ice flux scheme provided a more realistic  
917 representation of global lightning for present day. Therefore, the negative LNO<sub>x</sub> emissions change  
918 from this scheme may be more realistic. If indeed the ice flux scheme better represents the current  
919 distribution of lightning, both the Romps and Finney results suggest no significant increase in  
920 LNO<sub>x</sub> emission in future climate, and possibly a small global decrease. Murray (2018) points out  
921 that the ice flux scheme is a closer representation of the underlying charging mechanism, but this  
922 scheme needs to be tested in multiple global chemistry and climate models.

923

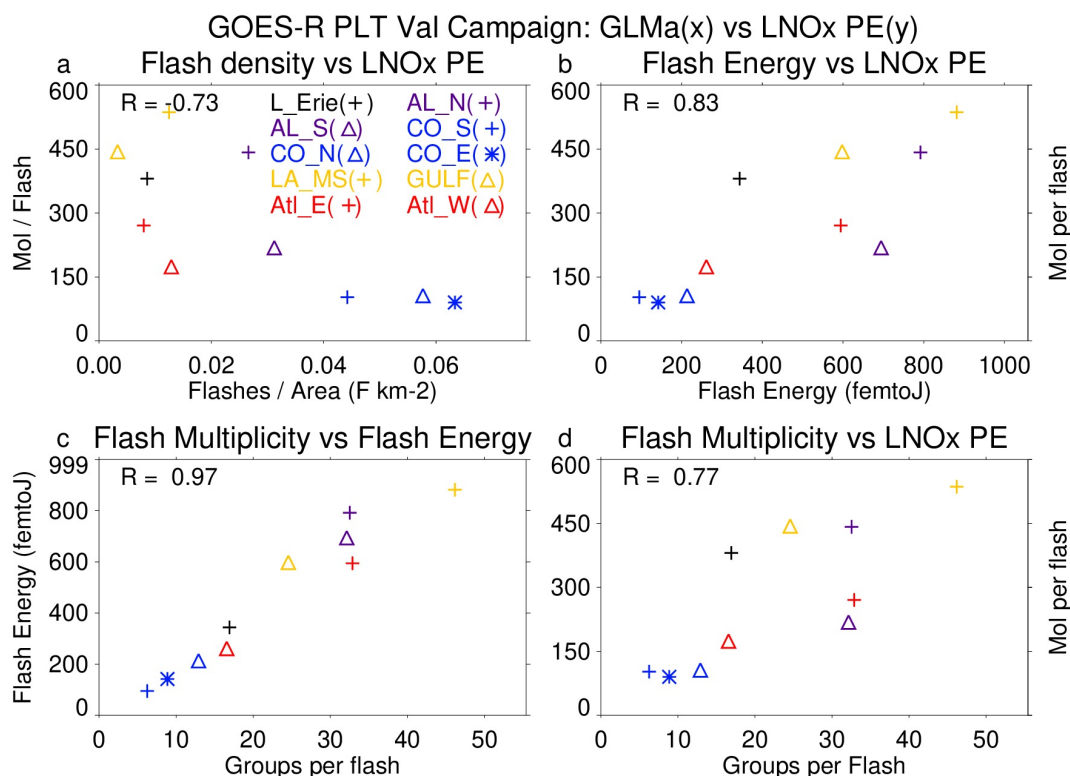
#### 924 **3.5.4. Recent findings concerning LNO<sub>x</sub> PE**

925 Recent satellite-based estimates of LNO<sub>x</sub> production (Figure 22) have suggested a possible flash  
926 rate dependence of LNO<sub>x</sub> production per flash (Bucsela et al., 2019; Allen et al., 2019; 2021).  
927 Smaller values of LNO<sub>x</sub> PE in these studies were found to be associated with high flash rates,  
928 likely due to smaller flashes in these conditions (Bruning and Thomas, 2015). Allen et al. (2021a)  
929 noted positive correlations (Figure 22) of LNO<sub>x</sub> PE with flash energy and with flash multiplicity  
930 (number of strokes per flash). Laboratory studies by Wang et al. (1998) found a positive correlation  
931 between peak current and LNO<sub>x</sub> production. Koshak et al. (2015) found an 8% increase in peak  
932 current from the 2003-2007 period to the 2008-2012 period that accompanied the 12.8% decrease



933 in CG flashes. These findings make it difficult to project future LNO<sub>x</sub> production given only a  
 934 prediction of future lightning flashes.

935



936

937 Figure 22. Scatterplots showing the GLMa-derived relationship between (a) LNO<sub>x</sub> PE (mol per  
 938 flash) and flash density (flashes km<sup>-2</sup>), (b) LNO<sub>x</sub> PE and flash energy (fJ), (c) flash energy and  
 939 flash multiplicity, and (d) LNO<sub>x</sub> PE and flash multiplicity. Colors are used to separate flight days  
 940 while symbols are used to separate system within each flight day. Correlations are shown in the  
 941 upper right. LNO<sub>x</sub> PE derived from airborne remote sensor, the Geo-CAPE Airborne Simulator  
 942 (GCAS) during the GOES-R Post-launch Test field campaign. GLMa indicates Geostationary  
 943 Lightning Mapper data adjusted for missing data. From Allen et al. (2021a).

944

### 945 3.5.5. Impacts of LNO<sub>x</sub> on upper tropospheric O<sub>3</sub>

946 The literature concerning the effects of lightning NO<sub>x</sub> production on upper tropospheric ozone  
 947 focuses on photochemical ozone production in storm outflow The STERAO-A storm simulation  
 948 by DeCaria et al. (2005) indicated that additional ozone production attributable to lightning NO  
 949 within the storm cloud during the lifetime of the storm was very small (~2 ppbv). However,  
 950 simulation of the photochemistry over the 24 hours following the storm showed that an additional  
 951 10 ppbv of ozone production in the upper troposphere can be attributed to lightning NO production.  
 952 Convective transport of HO<sub>x</sub> precursors led to the generation of a HO<sub>x</sub> plume, which substantially  
 953 aided the downstream ozone production. Ott et al. (2007) simulated the July 21, 1998 EULINOX  
 954 thunderstorm. During the storm, the inclusion of lightning NO<sub>x</sub> in the model combined with



955 convectively-transported boundary layer  $\text{NO}_x$  from the Munich, Germany region resulted in  
956 sufficiently large  $\text{NO}_x$  mixing ratios to cause a small titration loss of ozone (on average less than  
957 4 ppbv) at all model levels. Simulations of the chemical environment in the 24 hours following the  
958 storm show on average a small increase in the net production of ozone at most levels resulting  
959 from lightning  $\text{NO}_x$ , maximizing at approximately 5 ppbv per day at 5.5 km. Between 8 and 10.5  
960 km, lightning  $\text{NO}_x$  caused decreased net ozone production. Ren et al. (2008) found that net  
961 tropospheric ozone production proceeded at a median rate of  $\sim 11$  ppbv per day above 9 km in the  
962 Intercontinental Transport Experiment (INTEX-A) in which the effects of frequent deep  
963 convection over the United States dominated the upper troposphere. Apel et al. (2012) noted that  
964 a box model calculation indicated a net ozone increase of  $\sim 10$  ppbv over a few hours following  
965 observed convection with lightning over Canada in the Arctic Research of the Composition of the  
966 Troposphere from Aircraft and Satellite (ARCTAS) experiment. Apel et al. (2015) performed box  
967 modeling of the chemistry downwind of two DC3 storms in northeast Colorado on June 22, 2012.  
968 The northern storm ingested fresh biomass burning smoke, and the southern storm was affected  
969 by more aged biomass burning emissions. The model predicted substantial downwind ozone  
970 production in the UT for both storms. The southern storm was predicted to produce more ozone  
971 over 2 days (14 ppbv) than the northern storm (11 ppbv) despite having lower VOC OH reactivity.  
972 Sensitivity tests showed that this was principally due to more  $\text{NO}_x$  being present in the southern  
973 storm outflow because of  $\text{LNO}_x$ . Brune et al. (2018) found general agreement between observed  
974 and modeled OH and  $\text{HO}_2$  in the outflow of the June 21, 2012 DC3 mesoscale convective system.  
975 In this study the DC-8 made multiple passes through the outflow as it moved downwind. Box  
976 model calculations yielded a 13 ppbv increase in ozone over 5 hours, similar to the observed 14  
977 ppbv increase (see Brune et al, 2018). This rate of increase is larger than others in the literature,  
978 perhaps because for a portion of the 5 hours the outflow was in cirrus cloud, in which photolysis  
979 rates may have been larger than clear-sky values due to multiple scattering. Using a regional  
980 chemistry model, Pickering et al. (2023) estimated that net ozone production in the upper  
981 tropospheric outflow of a severe high flash rate storm observed over Oklahoma proceeded at a rate  
982 of 10-11 ppbv  $\text{day}^{-1}$  during the first 24 hours of downwind transport. Downwind photochemical  
983 production of ozone due to  $\text{LNO}_x$  accounted for much of the recovery of upper tropospheric ozone  
984 following large reductions due to convective transport of lower ozone boundary layer air.

### 985 **3.5.6. Summary of $\text{LNO}_x$**

986  $\text{LNO}_x$  is responsible for the largest fraction of upper tropospheric ozone in the tropics year-round  
987 and in the mid-latitudes in summer. Radiative forcing due to ozone is most sensitive due to the  
988 ozone near the tropopause. Therefore, it is of great importance to have knowledge of the trends in  
989 ozone in this region that are due to changes in frequency and characteristics of lightning flashes.  
990 While uncertainty remains concerning trends in global flash rates, regionally important trends have  
991 been noted in CONUS and in China, which tend to be correlated to the decreasing atmospheric  
992 aerosol content. An increasing trend at Arctic latitudes has been noted, as that region rapidly  
993 warms. Future trends in flash rate also are uncertain, with conflicting predictions coming from  
994 models with differing flash rate parameterizations. Flash characteristics (e.g., flash extent, flash  
995 energy or peak current, intracloud fraction) have been found to have important implications for  
996  $\text{LNO}_x$  production per flash. Insufficient knowledge of these characteristics makes it highly  
997 uncertain to estimate changes in  $\text{LNO}_x$  production, even with knowledge of flash rate trends.

998



999 **3.6. Soil NO and HONO emissions and their impacts on O<sub>3</sub>**

1000 Nitrous acid (HONO) is produced from microbial activity in soils with a similar mechanism and  
1001 strength as NO (Oswald et al., 2013). This emission source may partially account for the current  
1002 mismatch between observed and simulated HONO levels in the lower troposphere (Su et al.,  
1003 2011; Yang et al., 2020). Zhang et al. (2016) estimate a 29 % contribution of soil-HONO to the  
1004 HONO sources in China. This may also contribute significantly to OH production with important  
1005 implications for the HO<sub>x</sub> and O<sub>3</sub> budget. To account for this emission source and assess the  
1006 global potential for atmospheric pollution soil-HONO emissions have been parameterized based  
1007 on the HONO/NO emission ratio measured at multiple field samples (taken from different  
1008 regions of the world) and up-scale it to the 4 major land cover types applied to the whole globe.  
1009 The study estimates a global emission source of 7 TgN/yr from soil-HONO in 2009 (Emmerichs  
1010 et al., 2023). This is at the lower end of the estimated range of 7.4-12 TgN/yr presented by Wu et  
1011 al. (2022) for 2017 who employ an empirical and statistical model in combination with  
1012 observations. Due to the importance of NO and HONO soil emissions for the O<sub>3</sub> budget their  
1013 variability and historical and future trends are described here and linked to O<sub>3</sub>. Additionally, we  
1014 discuss a modification of the soil NO emission scheme.

1015 **3.6.1. Global modeling of reactive nitrogen emissions from soil**

1016 In this section, we present a short overview of the soil-NO emission algorithms and estimates for  
1017 regional and global emissions. The emission of nitrogen oxides (NO) from the soil is the major  
1018 source of NO<sub>x</sub> in unpolluted regions accounting for 15-25 % of global emissions (Weng et al.,  
1019 2020, Vinken et al., 2014). Thereby, NO is produced from the nitrification in soil (microbial  
1020 activity) and depends non-linearly on soil properties like pH, carbon and nutrient content,  
1021 temperature, and soil moisture (Gödde and Conrad 2000, Oswald et al. 2013). Model algorithms  
1022 estimate soil-NO emissions with a function dependent on biological and meteorological drivers.  
1023 The common empirical approach by Yienger and Levy (1995), which is used in the current  
1024 CMIP6 simulations (Szopa et al. 2022), is based on a biome-specific emission factor, soil  
1025 temperature, precipitation, and the canopy uptake reduction factor. The resulting global estimate  
1026 is in the range of 3.3-7.7 TgN/yr which is, however, only at the lower end of the more recent  
1027 model and observation-based estimates. The Yienger and Levy (1995) approach generally  
1028 underestimates soil NO for all landcover types except in the tundra and rainforest due to the  
1029 pulsing parameterization, which describes a large NO<sub>x</sub> release at the wetting of very dry soil and  
1030 the subsequent rapid decay (Steinkamp et al., 2009). This is accounted for in the more  
1031 mechanistic approach by Hudman et al. (2012) representing pulsing of the emissions following  
1032 dry spells and N-inputs from chemical fertilizer and atmospheric N-deposition. This approach  
1033 calculates spatial and temporal patterns of soil moisture, temperature, pulsing, fertilizer, manure  
1034 and atmospheric N deposition and biome overall replacing the emission factors by Yienger and  
1035 Levy (1995) which yields in comparison 34 % more annual global soil emissions of nitrogen  
1036 oxide (10.7 TgN/yr). Satellite top-down estimates range from 7.9 TgN/yr (Miyazaki et al., 2017:  
1037 2005-2014, assimilation of satellite data sets) to 16.7 TgN/yr (Vinken et al., 2014; GEOS-Chem  
1038 and OMI). The emission of soil-NO varies regionally with small sources in Australia (~0.5  
1039 TgN/yr), Europe, Russia and Southern Hemisphere (SH) Africa (0.7 TgN/yr, 0.8 TgN/yr),  
1040 America (0.9-1 TgN/yr) and high values in S.E. Asia and Northern Hemisphere (NH) Africa (2-  
1041 2.1 TgN/yr). The emission estimates (here for 0.25° lat. × 0.3125° lon.) increase with resolution  
1042 in some regions like Europe by 38 % (Weng et al., 2020).

1043 Nitrous acid (HONO), a major OH source, is also produced from microbial activity in soils with  
1044 a similar mechanism and strength as NO (Oswald et al., 2013). This additional emission source



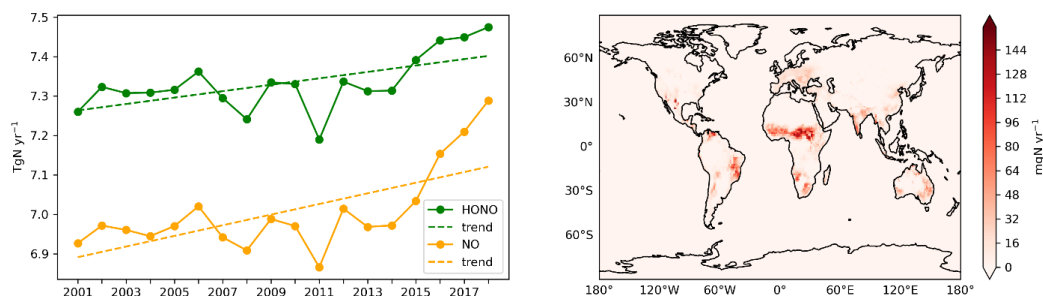
1045 may account for the current mismatch between models and measurements representing HONO  
 1046 levels in the lower troposphere (Su et al., 2011; Yang et al., 2020). Soil emissions of HONO play  
 1047 a major role in the daytime-HONO concentrations in rural areas (in the lowest layers) where  
 1048 traffic emissions and NO<sub>2</sub> heterogeneous reactions occur less than in urban areas (Wu et al.  
 1049 2022). HONO photolysis is a main OH source and impacts the oxidation capacity of the  
 1050 atmosphere (Zhang 2016, 2019). Therefore, this may also contribute significantly to OH  
 1051 production with important implications for the HO<sub>x</sub> and O<sub>3</sub> budget.

### 1052 3.6.2. Variability and trends of soil emissions of NO and HONO in the last 15 years

1053 The magnitude of soil emissions varies strongly with season where the emissions rise from  
 1054 January and July by a factor of 2.5 (Weng et al., 2020). This follows the meteorological  
 1055 variability as for instance, heavy rainfall over dry grasslands/forests causes a pulse of soil NO  
 1056 emissions coupled with the usage of fertilizer (Hudman et al., 2012). According to the CCMI  
 1057 simulations by Jöckel et al. (2016) (following the future ('medium high') climate scenario  
 1058 RCP6.0 the soil NO emissions show a positive trend since pre-industrial times with a steeper  
 1059 increase of up to 0.3 TgN/decade from the year 2000. As soil emissions of HONO rely on the  
 1060 same biogeochemical process with similar dependencies on temperature and water content as NO  
 1061 also increased from 2000 to 2019.

1062 For soil-HONO, however, the trend over 2005-2019 is much smaller, most pronounced in  
 1063 Central Africa (Figure 24). Thereby, the highest positive monthly anomalies occur mainly in the  
 1064 5 most recent years which is likely due to the more frequent heat wave occurrence, e.g. in Europe  
 1065 and North America. Overall, Africa relates the most (~30%) to the global anomaly (Figure 23 -  
 1066 Figure 24).

1067



1068

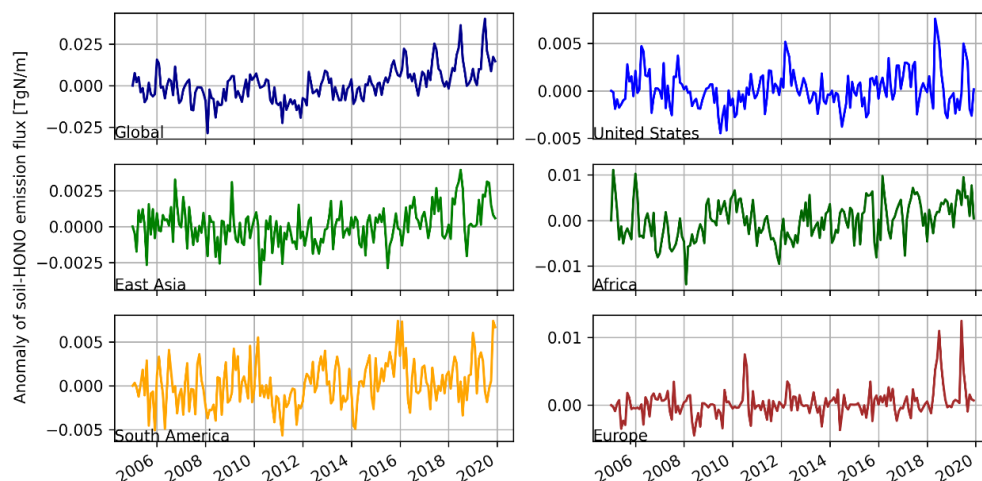
1069 Figure 23: Time series of soil-HONO and soil-NO emissions and their trends (left) and the mean  
 1070 global distribution of the soil-HONO emission trend for 2005-2019 based on monthly anomalies  
 1071 (right).

1072

1073 Since soil-HONO emissions contribute 10-20 % to surface O<sub>3</sub>, most significantly in the Southern  
 1074 Hemisphere (Wu et al., 2022), its positive emission trends may have contributed to the decrease  
 1075 in O<sub>3</sub> over the last 15 years (see other sections).

1076





1077

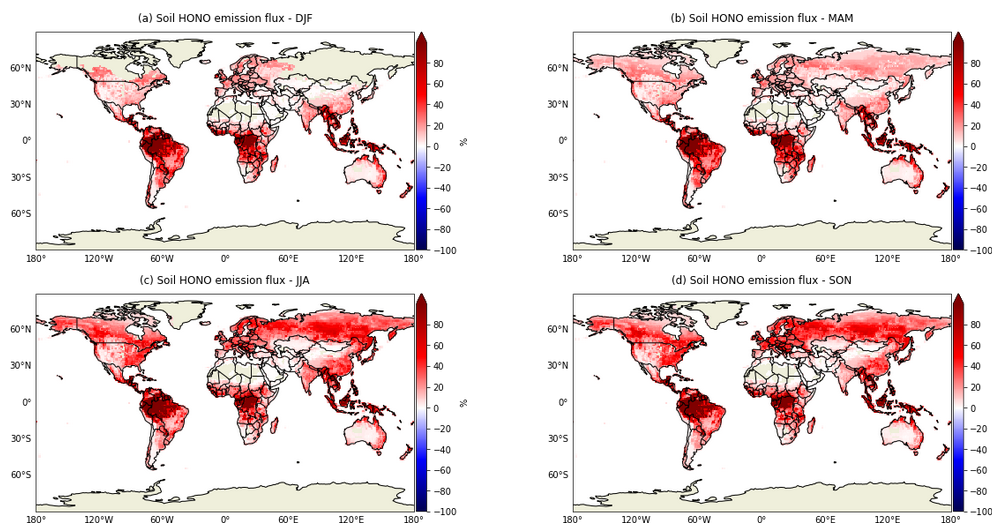
1078 Figure 24: Monthly anomalies of HONO emissions from soil (de-seasonalized).

1079

1080 **3.6.3. Canopy Reduction Factor**

1081 Most NO soil emission models (Yienger and Levy, 1995; Hudman et al., 2012) rely on an  
 1082 empirical canopy reduction scheme which represents loss processes in plants as the diffusion of  
 1083 NO<sub>2</sub> through the stomata and direct deposition to the cuticle. In particular, a large fraction of  
 1084 NO<sub>x</sub> (and peroxyacyl nitrate) loss during night may be only explainable by non-stomatal  
 1085 processes (Delaria et al., 2020b). Mechanistically, the canopy reduction can be described by an  
 1086 efficient NO<sub>x</sub> deposition to plants. Thus, Delaria et al. (2020a) points out that models already  
 1087 represent the uptake by vegetation and do not need to use a canopy reduction scheme. The  
 1088 potential change of NO soil emissions is shown by employing the global model  
 1089 ECHAM/MESSy (1°x1°) with an explicit trace gas uptake at stomata and cuticle (Emmerichs et  
 1090 al., 2021) for two different seasons in 2005 and 2006. Removing the canopy reduction factor in  
 1091 the model leads to a significant increase of soil NO emissions highest over tropical forests  
 1092 (Figure 25). The temporal variation follows the vegetational growth as in the Northern  
 1093 Hemisphere summer 50% higher emissions occur. These findings are reasonable as Hudman et  
 1094 al. (2012) estimated that the canopy reduction scheme overall lowers the NO emissions by 10-  
 1095 15% at grasslands and up to 85% over forests (GEOS-Chem at 2°x2.5° in 2006). Consequently,  
 1096 improper accounting for the canopy reduction factor may imply a strong underestimation of the  
 1097 soil-N in densely forested regions and globally by about 31% (2005-2006).

1098



1099

1100 Figure 25: Relative difference Canopy Reduction soil HONO

1101

1102 **3.6.4. Projections of soil NO and variability in different climates**

1103 The future land use is predicted to change as a consequence of the growing demand for  
 1104 nutrition and biofuels which implies an increasing use of fertilizer. Consequently, NO soil  
 1105 emissions are estimated to rise by ~28% during the century to 11.5 TgN/yr at the end of 2100  
 1106 (Fowler et al., 2015). Similarly, Liu et al. (2021) estimate an increasing soil NO emission of 8.9  
 1107 TgN/yr by the year 2050 due to intensive nitrification processes.

1108 An increase of LAI by 10 %, in contrast, would lead to 1% lower emissions. In addition, several  
 1109 responses are expected from the changing climate. In fact, the 1°C higher temperature would  
 1110 cause ~5% increase of emissions (Weng et al., 2020). Following the future (‘medium high’)  
 1111 climate scenario RCP6.0 (Representative Concentration Pathway, 6 W/m<sup>2</sup> radiative forcing until  
 1112 2500, stabilization after 2150) used for the CMIP5 (Climate Model Intercomparison Project)  
 1113 simulations. Jöckel et al. (2016) suggest an increase of ~15 % soil NO emissions due to  
 1114 increasing soil temperature (an increase of soil microbes) since present-day (2010) until 2100.  
 1115 However, the most significant implications for large-scale denitrification activity are changing  
 1116 rainfall and the regional hydrological cycles (Fowler et al., 2015). In general, soil NO<sub>x</sub> will play  
 1117 a more important role for the global budget in the troposphere due to the decreasing  
 1118 anthropogenic emissions in the future. Therefore, increasing NO<sub>x</sub>-soil emissions may slow down  
 1119 the decrease of O<sub>3</sub> in response to declining anthropogenic emissions (Wu et al. 2022).

1120

1121 **3.6.5. Next steps with biogeochemical models implemented in ESMs**

1122 Uncertainties of modeling soil nitrogen emissions are associated with the model input and  
 1123 parameters (Wang and Chen 2012). Process-based biogeochemical models which also consider  
 1124 the complexity of soil emission processes as DNDC (Denitrification–Decomposition) are needed  
 1125 (Li et al., 2011). The capability to represent interactive biogeochemical cycles allows for  
 1126 instance for the online calculation of crop nutrition from soil. Also, a model like CLM5  
 1127 distinguishes between natural and agricultural soils which more accurately predicts the fertilizer



1128 usage (Fung et al., 2022). Resolving the soil and litter biogeochemical dynamics vertically, in  
1129 addition, lead to a more efficient retainment and recycling of N by the ecosystem (Koven et al.,  
1130 2013). However, these models should be calibrated to multiple sites (Wang et al., 2019) which is  
1131 limited by the availability of measurement data, especially when it comes to global modeling.

1132

#### 1133 **4. Conclusion**

1134 In this article, we investigate temporal and spatial trends and variability of tropospheric ozone in  
1135 relation to its precursors using satellite products, ozonesonde measurements, and model  
1136 simulations. Our results show that ozone has positive trends at all latitudes and column depths  
1137 regardless of the tropopause height within  $\pm 100$  hPa. The positive trends in the 30-60°N band are  
1138 due to increasing trends over Canada and Alaska and are slightly offset by the small negative  
1139 trends over the Eastern US and Europe. The decreasing trends above 30°N and 30°S are due to  
1140 the offsetting impact of negative trends over Eastern US and Europe in the north, and Australia  
1141 and South Africa in the south, respectively. The decreasing trends of TrC-O<sub>3</sub> over Eastern US  
1142 and Europe are consistent with the decreasing trend of TrC-NO<sub>2</sub>, which is due to the effective  
1143 measures applied over the last two decades to mitigate air pollution in these regions. The  
1144 decrease of TrC-O<sub>3</sub> as a result of decreasing TrC-NO<sub>2</sub> trends is due to the NO-sensitive  
1145 conditions dominating most of these regions. The increasing trends of TrC-O<sub>3</sub> in the other  
1146 regions of the world where TrC-NO<sub>2</sub> is decreasing as a result of VOC-sensitive conditions,  
1147 especially over East Asia. TrC-HCHO trends are decreasing in the Eastern US, some parts of  
1148 northern and western Africa, and western and northern Europe increasing in South Asia, central  
1149 Africa, northern Australia, and Brazil. TrC-HCHO trends are consistent with that of TrC-O<sub>3</sub> over  
1150 Eastern US and Europe. The decreasing trends of HCHO and O<sub>3</sub> as NO<sub>2</sub> increases is evidence of  
1151 the VOC-limited conditions in these regions. Under these conditions, increased NO<sub>2</sub> levels lead  
1152 to a reduction of OH, which decreases the oxidation capacity and thus lowers the photochemical  
1153 formation of HCHO and O<sub>3</sub>. We have also shed light on NO<sub>x</sub> lightning and its relation to ozone  
1154 trends. LNO<sub>x</sub> is responsible for the largest fraction of upper tropospheric ozone in the tropics  
1155 year-round and in the mid-latitudes in summer. Ozone Radiative forcing is due to the ozone near  
1156 the tropopause. An increasing trend of LNO<sub>x</sub> at Arctic latitudes has been noted, as that region  
1157 rapidly warms. However, future trends in flash rate are uncertain, with conflicting predictions  
1158 coming from models with differing flash rate parameterizations. Soil HONO emissions had their  
1159 highest positive monthly anomalies mainly in the 5 most recent years which is likely due to the  
1160 more frequent heat wave occurrence, e.g. in Europe and North America. Soil HONO trends are  
1161 highest in Africa accounting for ~30% of the global anomaly. Soil NO<sub>x</sub> emissions could play an  
1162 important role in the tropospheric NO<sub>x</sub> global budget due to the decreasing anthropogenic  
1163 emissions in the future. Therefore, the expected increase in NO<sub>x</sub>-soil emissions may slow down  
1164 the decrease of O<sub>3</sub> in response to declining anthropogenic emissions. Overall, this study  
1165 presented a comprehensive overview of tropospheric ozone trends in relation to its precursors in  
1166 different spatial and temporal scales.

1167 Competing interests: At least one of the (co-)authors is a member of the editorial board of  
1168 Atmospheric Chemistry and Physics

#### 1169 **Acknowledgment**

1170 This study was partially funded by the NSF AGS, grant number 1900795, USF Creative  
1171 Scholarship Grant 2022. A part of the research was conducted at the Jet Propulsion Laboratory,  
1172 California Institute of Technology, under a contract with NASA. HP has received funding from



1173 the Ministerio de Ciencia e Innovación through the MITIGATE project (grant no. PID2020-  
1174 113840RA-I00 funded by MCIN/AEI/10.13039/501100011033) and the Ramon y Cajal grant  
1175 (RYC2021-034511-I, MCIN / AEI / 10.13039/501100011033 and European Union  
1176 NextGenerationEU/PRTR). The GEOS-GMI simulation was supported by the NASA's Making  
1177 Earth System Data Records for Use in Research Environments (MEaSUREs) program and the  
1178 high-performance computing resources for GEOS-GMI were provided by the NASA Center for  
1179 Climate Simulation (NCCS).

1180

## 1181 5. References

- 1182 Allen, D., Pickering, K., Duncan, B., and Damon, M. (2010), Impact of lightning NO  
1183 emissions on North American photochemistry as determined using the Global  
1184 Modeling Initiative (GMI) model, *J. Geophys. Res.*, 115, D22301,  
1185 doi:10.1029/2010JD014062.
- 1186 Allen, D. J., Pickering, K. E., Pinder, R. W., Henderson, B. H., Appel, K. W., and Prados, A.  
1187 (2012), Impact of lightning-NO on eastern United States photochemistry during the  
1188 summer of 2006 as determined using the CMAQ model, *Atmos. Chem.  
1189 Phys.*, 12, 1737-1758, doi:10.5194/acp-12-1737-2012.
- 1190 Allen, D. J., Pickering, K. E., Bucsel, E., van Geffen, J., Lapierre, J., Koshak, W., & Eskes,  
1191 H. (2021b). Observations of Lightning NO<sub>x</sub> production from Tropospheric Ozone  
1192 Monitoring Instrument Case Studies over the United States, *J. Geophys. Res.*, 126  
1193 (10), <https://doi.org/10.1029/2020JD034174>.
- 1194 Allen, D. J., Pickering, K. E., Lamsal, L., Mach, D., Quick, M. G., Lapierre, J., Janz, S.,  
1195 Koshak, W., Kowalewski, M. & Blakeslee, R. (2021a), Observations of Lightning  
1196 NO<sub>x</sub> production from GOES-R Post Launch Test Field Campaign Flights, *J. Geophys.  
1197 Res.*, 126 (8), <https://doi.org/10.1029/2020JD033769>.
- 1198 Allen, D., J., Pickering, K. E., Bucsel, E., Krotkov, N., and Holzworth, R. (2019), Lightning  
1199 NO<sub>x</sub> Production in the Tropics as Determined Using OMI NO<sub>2</sub> Retrievals and  
1200 WWLLN Stroke Data, *J. Geophys. Res.*, <https://doi.org/10.1029/2018JD029824>.
- 1201 Apel, E. C., J. R. Olson, J. H. Crawford, R. S. Hornbrook, A. J. Hills, C. A. Cantrell, L. K.  
1202 Emmons, D. J. Knapp, S. Hall, R. L. Mauldin III, A. J. Weinheimer, A. Fried, D. R.  
1203 Blake, J. D. Crouse, J. M. St. Clair, P. O. Wennberg, G. S. Diskin, H. E. Fuelberg,  
1204 A. Wisthaler, T. Mikoviny, W. Brune, and D. D. Riemer, (2012) Impact of the deep  
1205 convection of isoprene and other reactive trace species on radicals and ozone in the  
1206 upper troposphere, *Atmos. Chem. Phys.*, 12, 1135–1150, [www.atmos-chem-  
1207 phys.net/12/1135/2012/doi:10.5194/acp-12-1135-2012](http://www.atmos-chem-phys.net/12/1135/2012/doi:10.5194/acp-12-1135-2012).
- 1208 Apel, E. C., et al. (2015), Upper tropospheric ozone production from lightning NO<sub>x</sub>-  
1209 impacted convection: Smoke ingestion case study from the DC3 campaign, *J.  
1210 Geophys. Res. Atmos.*, 120, doi:10.1002/2014JD022121.
- 1211 Barret, B., De Mazière, M., and Mahieu, E.: Ground-based FTIR measurements of CO from  
1212 the Jungfraujoch: characterisation and comparison with in situ surface and MOPITT  
1213 data, *Atmos. Chem. Phys.*, 3, 2217–2223, <https://doi.org/10.5194/acp-3-2217-2003>,  
1214 2003.



- 1215 Bauwens, M.; Compornolle, S.; Stavrou, T.; Müller, J.; Gent, J.; Eskes, H.; Levelt, P.F.;  
1216 van der A, R.; Veeffkind, J.P.; Vlietinck, J.; et al. Impact of Coronavirus Outbreak on  
1217 NO<sub>2</sub> Pollution Assessed Using TROPOMI and OMI Observations. *Geophys. Res.*  
1218 *Lett.* 2020, 47.
- 1219 Beirle, S., H. Huntrieser, and T Wagner (2010), Direct satellite observation of lightning-  
1220 produced NO<sub>x</sub>, *Atmos. Chem. Phys.*, 10(22), 10965-10986, doi:10.5194/acp-10-  
1221 10965.
- 1222 Boersma, K., Eskes, H., Richter, A., De Smedt, I., Lorente, A., Beirle, S., Van Geffen, J.,  
1223 Peters, E., Van Roozendaal, M., and Wagner, T.: QA4ECV NO<sub>2</sub> tropospheric and  
1224 stratospheric vertical column data from OMI (Version 1.1) (data set), Royal  
1225 Netherlands Meteorological Institute (KNMI), [https://doi.org/10.21944/qa4ecv-no2-](https://doi.org/10.21944/qa4ecv-no2-omi-v1.1)  
1226 [omi-v1.1](https://doi.org/10.21944/qa4ecv-no2-omi-v1.1), 2017a.
- 1227 Boersma, K., Eskes, H., Richter, A., De Smedt, I., Lorente, A., Beirle, S., Van Geffen, J.,  
1228 Peters, E., Van Roozendaal, M., and Wagner, T.: QA4ECV NO<sub>2</sub> tropospheric and  
1229 stratospheric vertical column data from GOME-2 (Version 1.1) (data set), Royal  
1230 Netherlands Meteorological Institute (KNMI), [https://doi.org/10.21944/qa4ecv-no2-](https://doi.org/10.21944/qa4ecv-no2-gome2a-v1.1)  
1231 [gome2a-v1.1](https://doi.org/10.21944/qa4ecv-no2-gome2a-v1.1), 2017b.
- 1232 Boersma, K., Eskes, H., Richter, A., De Smedt, I., Lorente, A., Beirle, S., Van Geffen, J.,  
1233 Peters, E., Van Roozendaal, M., and Wagner, T.: QA4ECV NO<sub>2</sub> tropospheric and  
1234 stratospheric vertical column data from SCIAMACHY (Version 1.1) (data set), Royal  
1235 Netherlands Meteorological Institute (KNMI), [https://doi.org/10.21944/qa4ecv-no2-](https://doi.org/10.21944/qa4ecv-no2-scia-v1.1)  
1236 [scia-v1.1](https://doi.org/10.21944/qa4ecv-no2-scia-v1.1), 2017c.
- 1237 Boersma, K. F., Eskes, H. J., Richter, A., De Smedt, I., Lorente, A., Beirle, S., van Geffen, J.  
1238 H. G. M., Zara, M., Peters, E., Van Roozendaal, M., Wagner, T., Maasackers, J. D.,  
1239 van der A, R. J., Nightingale, J., De Rudder, A., Irie, H., Pinardi, G., Lambert, J.-C.,  
1240 and Compornolle, S. C.: Improving algorithms and uncertainty estimates for satellite  
1241 NO<sub>2</sub> retrievals: results from the quality assurance for the essential climate variables  
1242 (QA4ECV) project, *Atmos. Meas. Tech.*, 11, 6651–6678, [https://doi.org/10.5194/amt-](https://doi.org/10.5194/amt-11-6651-2018)  
1243 [11-6651-2018](https://doi.org/10.5194/amt-11-6651-2018), 2018.
- 1244 Brune, W. H., et al. (2018) Atmospheric oxidation in the presence of clouds during the Deep  
1245 Convective Clouds and Chemistry (DC3) study, *Atmos. Chem. Phys.*, 18, 14493–14510,  
1246 2018, <https://doi.org/10.5194/acp-18-14493-2018>.
- 1247 Bruning, E. C. & Thomas, R. J. (2015), Lightning channel length and flash energy  
1248 determined from moments of the flash area distribution, *J. Geophys. Res. Atmos.*,  
1249 120, 8925–8940, doi:[10.1002/2015JD023766](https://doi.org/10.1002/2015JD023766)
- 1250 Buchholz, R.R.; Deeter, M.N.; Worden, H.M.; Gille, J.; Edwards, D.P.; Hannigan, J.W.;  
1251 Jones, N.B.; Paton-Walsh, C.; Griffith, D.W.T.; Smale, D.; et al. Validation of  
1252 MOPIIT carbon monoxide using ground-based Fourier transform infrared  
1253 spectrometer data from NDACC. *Atmos. Meas. Tech.* 2017, 10, 1927–1956.
- 1254 Buchholz, R. R., Worden, H. M., Park, M., Francis, G., Deeter, M. N., Edwards, D. P.,  
1255 Emmons, L. K., Gaubert, B., Gille, J., Martinez-Alonso, S., Tang, W., Kumar, R.,  
1256 Drummond, J. R., Clerbaux, C., George, M., Coheur, P.-F., Hurtmans, D., Bowman,  
1257 K. W., Luo, M., Payne, V. H., Worden, J. R., Chin, M., Levy, R. C., Warner, J., Wei,  
1258 Z., and Kulawik, S. S.: Air pollution trends measured from Terra: CO and AOD over





- 1259 industrial, fire-prone, and background regions, *Remote Sens. Environ.*, 256, 112275,  
1260 <https://doi.org/10.1016/j.rse.2020.112275>, 2021.
- 1261 Bucsela, E. J., K. E. Pickering, T. L. Huntemann, R. C. Cohen, A. Perring, J. F. Gleason, R.  
1262 J. Blakeslee, R. I. Albrecht, R. Holzworth, J. P. Cipriani, D. Vargas-Navarro, I. Mora-  
1263 Segura, A. Pacheco-Hernández, S. Laporte-Molina, (2010) Lightning-generated NO<sub>x</sub>  
1264 seen by OMI during NASA's TC<sup>4</sup> experiment, *J. Geophys. Res.*, 115, D00J10,  
1265 doi:10.1029/2009JD013118.
- 1266 Bucsela, E., Pickering, K. E., Allen, D., Holzworth, R., and Krotkov, N. (2019), Midlatitude  
1267 lightning NO<sub>x</sub> Production Efficiency Inferred from OMI and WLLN Data, *J.*  
1268 *Geophys. Res.*, <https://doi.org/10.1029/2019JD030561>.
- 1269 Cazorla, M. and Herrera, E.: An ozonesonde evaluation of spaceborne observations in the  
1270 Andean tropics, *Sci Rep*, 12, <https://doi.org/10.1038/s41598-022-20303-7>, 2022.
- 1271 Chang K-L, Petropavlovskikh I, Cooper OR, Schultz MG, Wang T. Regional trend analysis  
1272 of surface ozone observations from monitoring networks in eastern North America,  
1273 Europe and East Asia. *Elem Sci Anth.* 2017;5:50. DOI: 10.1525/elementa.243.
- 1274 Chang K-L, Martin G. Schultz, Gerbrand Koren, Niklas Selke, Guidance note on best  
1275 statistical practices for TOAR analyses, <https://doi.org/10.48550/arXiv.2304.14236>,  
1276 2023.
- 1277 Christiansen, A., Mickley, L. J., Liu, J., Oman, L. D., and Hu, L.: Multidecadal increases in  
1278 global tropospheric ozone derived from ozonesonde and surface site observations: can  
1279 models reproduce ozone trends?, *Atmos Chem Phys*, 22, 14751–14782,  
1280 <https://doi.org/10.5194/acp-22-14751-2022>, 2022.
- 1281 Cummings, K. A., T. L. Huntemann, and K. E. Pickering (2013), Cloud-resolving chemistry  
1282 simulation of a Hector thunderstorm, *Atmos. Chem. Phys.*, 13(5), 2757–2777,  
1283 doi:10.5194/acp-13-2757.
- 1284 DeCaria, A., K. Pickering, G. Stenchikov, J. Scala, J. Stith, J. Dye, B. Ridley, and P.  
1285 Laroche, A cloud-scale model study of lightning-generated NO<sub>x</sub> in an individual  
1286 thunderstorm during STERAO-A, *J. Geophys. Res.*, 105, 11,601–11,616, 2000.
- 1287 DeCaria, A. J., K. E. Pickering, G. L. Stenchikov, and L. E. Ott (2005), Lightning-generated  
1288 NO<sub>x</sub> and its impact on tropospheric ozone production: A three-dimensional modeling  
1289 study of a STERAO-A thunderstorm, *J. Geophys. Res.*, 110, D14303,  
1290 doi:10.1029/2004JD005556. Deeter, M., Francis, G., Gille, J., Mao, D., Martínez-  
1291 Alonso, S., Worden, H., Ziskin, D., Drummond, J., Commane, R., Diskin, G., and  
1292 McKain, K.: The MOPITT Version 9 CO product: sampling enhancements and  
1293 validation, *Atmos. Meas. Tech.*, 15, 2325–2344, [https://doi.org/10.5194/amt-15-](https://doi.org/10.5194/amt-15-2325-2022)  
1294 2325-2022, 2022.
- 1295 De Smedt, I., Theys, N., Yu, H., Danckaert, T., Lerot, C., Compernelle, S., Van Roozendael,  
1296 M., Richter, A., Hilboll, A., Peters, E., Pedernana, M., Loyola, D., Beirle, S.,  
1297 Wagner, T., Eskes, H., van Geffen, J., Boersma, K. F., and Veefkind, P.: Algorithm  
1298 theoretical baseline for formaldehyde retrievals from S5P TROPOMI and from the  
1299 QA4ECV project, *Atmos. Meas. Tech.*, 11, 2395–2426, [https://doi.org/10.5194/amt-](https://doi.org/10.5194/amt-11-2395-2018)  
1300 11-2395-2018, 2018 Fadnavis, S., Sagalgile, A., Sonbawne, S., Vogel, B., Peter, T.,  
1301 Wienhold, F. G., Dirksen, R., Oelsner, P., Naja, M., and Müller, R.: Comparison of  
1302 ozonesonde measurements in the upper troposphere and lower Stratosphere in



- 1303 Northern India with reanalysis and chemistry-climate-model data, *Sci Rep*, 13, 7133,  
1304 <https://doi.org/10.1038/s41598-023-34330-5>, 2023.
- 1305 Duncan, B. N., Strahan, S. E., Yoshida, Y., Steenrod, S. D., and Livesey, N.: Model study of  
1306 the cross-tropopause transport of biomass burning pollution, *Atmos. Chem. Phys.*, 7,  
1307 3713–3736, <https://doi.org/10.5194/acp-7-3713-2007>, 2007.
- 1308 Elguindi, N., Granier, C., Stavrakou, T., Darras, S., Bauwens, M., Cao, H., Chen, C., Denier  
1309 van der Gon, H. A. C., Dubovik, O., Fu, T. M., Henze, D. K., Jiang, Z., Keita, S.,  
1310 Kuenen, J. J. P., Kurokawa, J., Liousse, C., Miyazaki, K., Müller, J. F., Qu, Z.,  
1311 Solmon, F., and Zheng, B.: Intercomparison of Magnitudes and Trends in  
1312 Anthropogenic Surface Emissions From Bottom-Up Inventories, Top-Down  
1313 Estimates, and Emission Scenarios, *Earths Future*, 8, e2020EF001520,  
1314 <https://doi.org/10.1029/2020EF001520>, 2020.
- 1315 Elshorbany, Y. F., Kurtenbach, R., Wiesen, P. Lissi, E., Rubio, M., Villena, G., Gramsch, E.,  
1316 Rickard, A. R., Pilling, M. J., Kleffmann, J.: Oxidation capacity of the city air of  
1317 Santiago, Chile, *Atmospheric Chemistry and Physics*, 9, 2257–2273, 2009.
- 1318 Elshorbany, Y. F., Barnes, I., Becker, K. H., Kleffmann, J., and Wiesen, P.: Sources and  
1319 Cycling of Tropospheric Hydroxyl Radicals-An Overview, *Zeitschrift für*  
1320 *Physikalische Chemie*, 224, 967–987, DOI:10.1524/zpch.2010.6136, 2010.
- 1321 Elshorbany, Y. F., Kleffmann, J., Hofzumahaus, A., Kurtenbach, R., Wiesen, P., Dorn, H.-P.,  
1322 Schlosser, E., Brauers, T., Fuchs, H., Rohrer, F., Wahner, A., Kanaya, Y., Yoshino,  
1323 A., Nishida, S., Kajii, Y., Martinez, M., Rudolf, M., Harder, H., Lelieveld, J., Elste,  
1324 T., Plass-Dülmer, C., Stange, G., and Berresheim, H.: HO<sub>x</sub> Budgets during  
1325 HO<sub>x</sub>Comp: a Case Study of HO<sub>x</sub> Chemistry under NO<sub>x</sub> limited Conditions, *J.*  
1326 *Geophys. Res.*, 117, D03307, doi: 10.1029/2011JD017008, 2012.
- 1327 Elshorbany, Y. F., Crutzen, P. J., Steil, B., Pozzer, A., Tost, H., and Lelieveld, J.: Global and  
1328 regional impacts of HONO on the chemical composition of clouds and aerosols,  
1329 *Atmos. Chem. Phys.*, 14, 1167–1184, <https://doi.org/10.5194/acp-14-1167-2014>,  
1330 2014.
- 1331 Elshorbany, Y. F.; Hannah C. Kapper; Jerald R. Ziemke; Scott A. Parr; (2021). The Status of  
1332 Air Quality in the United States During the COVID-19 Pandemic: A Remote Sensing  
1333 Perspective . *Remote Sensing*, doi:10.3390/rs13030369, 2021.
- 1334 Fehr, T., H. Höller, and H. Huntrieser (2004), Model study on production and transport of  
1335 lightning-produced NO<sub>x</sub> in a EULINOX supercell storm, *J. Geophys. Res.*, 109,  
1336 D09102, doi:10.1029/2003JD003935.
- 1337 Finney, D. L., R. M. Doherty, O. Wild, H. Huntrieser, H. C. Pumphrey, and A. M. Blyth  
1338 (2014), Using cloud ice flux to parameterize large-scale lightning, *Atmos. Chem.*  
1339 *Phys.*, 14, 12665–12682, [www.atmos-chem-phys.net/14/12665/2014/](http://www.atmos-chem-phys.net/14/12665/2014/)  
1340 doi:10.5194/acp-14-12665-2014.
- 1341 Finney, D. L., R. M. Doherty, O. Wild, P. J. Young, and A. Butler (2016), Response of  
1342 lightning NO<sub>x</sub> emissions and ozone production to climate change: Insights from the  
1343 Atmospheric Chemistry and Climate Model Intercomparison Project, *Geophys. Res.*  
1344 *Let.*, 43, 5492–5500, doi:[10.1002/2016GL068825](https://doi.org/10.1002/2016GL068825).



- 1345 Finney, D. L., R. M. Doherty, O. Wild, D. S. Stevenson, I. A. MacKenzie, and A. M. Blyth  
1346 (2018), A projected decrease in lightning under climate change, *Nature Climate*  
1347 *Change*, 8, 210-213.
- 1348 Fiore, A. M., L. W. Horowitz, E. J. Dlugokencky, and J. J. West (2006), Impact of  
1349 meteorology and emissions on methane trends, 1990–2004, *Geophys. Res. Lett.*, 33,  
1350 L12809, doi:10.1029/2006GL026199.
- 1351 Fleming, Z.L., Doherty, R.M., von Schneidmesser, E., Malley, C.S., Cooper, O.R., Pinto,  
1352 J.P., Colette, A., Xu, X., Simpson, D., Schultz, M.G., Lefohn, A.S., Hamad, S.,  
1353 Moolla, R., Solberg, S. and Feng, Z., Tropospheric Ozone Assessment Report:  
1354 Present-day ozone distribution and trends relevant to human health. 2018. *Elem Sci*  
1355 *Anth*, 6(1), p.12. DOI: 10.1525/elementa.73.
- 1356 Flynn, C. M., K. E. Pickering, J. H. Crawford, A. Weinheimer, K. L. Thornhill, C. Loughner,  
1357 P. Lee, Variability of O<sub>3</sub> and NO<sub>2</sub> profile shapes during DISCOVER-AQ:  
1358 Implications for satellite observations and comparisons to model-simulated profiles,  
1359 *Atmos. Environ.*, 147, 133-156, 2016.
- 1360 Fortems-Cheiney, A., Chevallier, F., Pison, I., Bousquet, P., Szopa, S., Deeter, M. N., and  
1361 Clerbaux, C.: Ten years of CO emissions as seen from Measurements of Pollution in  
1362 the Troposphere (MOPITT), *J. Geophys. Res.*, 116, D05304,  
1363 <https://doi.org/10.1029/2010JD014416>, 2011.
- 1364 Fortems-Cheiney, A., Chevallier, F., Pison, I., Bousquet, P., Saunio, M., Szopa, S., Cressot,  
1365 C., Kurosu, T. P., Chance, K., and Fried, A.: The formaldehyde budget as seen by a  
1366 global-scale multi-constraint and multi-species inversion system, *Atmos. Chem.*  
1367 *Phys.*, 12, 6699–6721, <https://doi.org/10.5194/acp-12-6699-2012>, 2012.
- 1368 Fullekrug, M. E. Williams, C. Price, S. Goodman, R. Holzworth, K. Virts, and D. Buechler  
1369 (2022) Sidebar 2.1: Lightning, in State of the Climate: 2021, *Bull. Amer. Meteor.*  
1370 *Soc.*, 108, S79-S81, doi:10.1175/BAMS-D-22-0092.1
- 1371 Fung, K. M., Val Martin, M., and Tai, A. P. K.: Modeling the interinfluence of fertilizer-  
1372 induced NH<sub>3</sub> emission, nitrogen deposition, and aerosol radiative effects using  
1373 modified CESM2, *Biogeosciences*, 19, 1635–1655, <https://doi.org/10.5194/bg-19-1635-2022>, 2022.
- 1375 Gaubert, B., Emmons, L. K., Raeder, K., Tilmes, S., Miyazaki, K., Arellano Jr., A. F., Elguindi,  
1376 N., Granier, C., Tang, W., Barré, J., Worden, H. M., Buchholz, R. R., Edwards, D. P.,  
1377 Franke, P., Anderson, J. L., Saunio, M., Schroeder, J., Woo, J.-H., Simpson, I. J.,  
1378 Blake, D. R., Meinardi, S., Wennberg, P. O., Crouse, J., Teng, A., Kim, M.,  
1379 Dickerson, R. R., He, H., Ren, X., Pusede, S. E., and Diskin, G. S.: Correcting model  
1380 biases of CO in East Asia: impact on oxidant distributions during KORUS-AQ, *Atmos.*  
1381 *Chem. Phys.*, 20, 14617–14647, <https://doi.org/10.5194/acp-20-14617-2020>, 2020.
- 1382 Gaudel, A., Cooper, O.R., Ancellet, G., Barret, B., Boynard, A., Burrows, J.P., Clerbaux, C.,  
1383 Coheur, P.-F., Cuesta, J., Cuevas, E., Doniki, S., Dufour, G., Ebojje, F., Foret, G.,  
1384 Garcia, O., Granados Muñoz, M.J., Hannigan, J.W., Hase, F., Huang, G., Hassler, B.,  
1385 Hurtmans, D., Jaffe, D., Jones, N., Kalabokas, P., Kerridge, B., Kulawik, S.S., Latter,  
1386 B., Leblanc, T., Le Flochmoën, E., Lin, W., Liu, J., Liu, X., Mahieu, E., McClure-  
1387 Begley, A., Neu, J.L., Osman, M., Palm, M., Petetin, H., Petropavlovskikh, I., Querel,  
1388 R., Rappoe, N., Rozanov, A., Schultz, M.G., Schwab, J., Siddans, R., Smale, D.,



- 1389 Steinbacher, M., Tanimoto, H., Tarasick, D.W., Thouret, V., Thompson, A.M.,  
1390 Trickl, T., Weatherhead, E., Wespes, C., Worden, H.M., Vigouroux, C., Xu, X.,  
1391 Zeng, G. and Ziemke, J., Tropospheric Ozone Assessment Report: Present-day  
1392 distribution and trends of tropospheric ozone relevant to climate and global  
1393 atmospheric chemistry model evaluation. 2018. *Elem Sci Anth*, 6(1), p.39. DOI:  
1394 10.1525/elementa.291.
- 1395 Gelaro, Ronald, et al. "The modern-era retrospective analysis for research and applications,  
1396 version 2 (MERRA-2)." *Journal of climate* 30.14 (2017): 5419-5454.
- 1397 Göttele and Conrad: <https://doi.org/10.1007/s003740000247>
- 1398 Grewe, V., Brunner, D., Dameris, M., Grenfell, J. L., Hein, R., Shindell, D., & Staehelin, J.  
1399 (2001), Origin and variability of upper tropospheric nitrogen oxides and ozone at  
1400 northern mid-latitudes, *Atmos. Env.*, 35, 3421-3433.
- 1401 Griffiths, P. T., Murray, L. T., Zeng, G., Shin, Y. M., Abraham, N. L., Archibald, A. T.,  
1402 Deushi, M., Emmons, L. K., Galbally, I. E., Hassler, B., Horowitz, L. W., Keeble, J.,  
1403 Liu, J., Moeini, O., Naik, V., O'Connor, F. M., Oshima, N., Tarasick, D., Tilmes, S.,  
1404 Turnock, S. T., Wild, O., Young, P. J., and Zanis, P.: Tropospheric ozone in CMIP6  
1405 simulations, *Atmos. Chem. Phys.*, 21, 4187–4218, [https://doi.org/10.5194/acp-21-](https://doi.org/10.5194/acp-21-4187-2021)  
1406 4187-2021, 2021.
- 1407 Holzworth, R. H., Brundell, J. B., McCarthy, M. P., Jacobson, A. R., Rodger, C. J., &  
1408 Anderson, T. S. (2021). Lightning in the Arctic. *Geophysical Research Letters*, 48,  
1409 e2020GL091366.  
1410 <https://doi.org/10.1029/2020GL091366>.
- 1411 Hubert, D., Heue, K.-P., Lambert, J.-C., Verhoelst, T., Allaart, M., Compernelle, S., Cullis,  
1412 P. D., Dehn, A., Félix, C., Johnson, B. J., Keppens, A., Kollonige, D. E., Lerot, C.,  
1413 Loyola, D., Maata, M., Mitro, S., Mohamad, M., PETERS, A., Romahn, F., Selkirk, H.  
1414 B., da Silva, F. R., Stauffer, R. M., Thompson, A. M., Veeffkind, J. P., Vömel, H.,  
1415 Witte, J. C., and Zehner, C.: TROPOMI tropospheric ozone column data: geophysical  
1416 assessment and comparison to ozonesondes, GOME-2B and OMI, *Atmos Meas Tech*,  
1417 14, 7405–7433, <https://doi.org/10.5194/amt-14-7405-2021>, 2021.
- 1418 Hudman et al., (2012) [www.atmos-chem-phys.net/12/7779/2012/](http://www.atmos-chem-phys.net/12/7779/2012/)
- 1419 Huntrieser, H., U. Schumann, H. Schlager, H. Höller, A. Giez, H.-D. Betz, D. Brunner, C.  
1420 Forster, O. Pinto Jr., and R. Calheiros (2008), Lightning activity in Brazilian  
1421 thunderstorms during TROCCINOX: Implications for NO<sub>x</sub> production, *Atmos. Chem.*  
1422 *Phys.*, 8, 21–953.
- 1423 Huntrieser, H., H. Schlager, M. Lichtenstern, P. Stock, T. Hamburger, H. Hoeller, K.  
1424 Schmidt, H.-D. Betz, A. Ulanovsky, and F. Ravegnani (2011) Mesoscale convective  
1425 systems observed during AMMA and their impact on the NO<sub>x</sub> and O<sub>3</sub> budget over  
1426 West Africa, *Atmos. Chem. Phys.*, 11, 2503–2536, [www.atmos-chem-](http://www.atmos-chem-phys.net/11/2503/2011)  
1427 [phys.net/11/2503/2011](http://www.atmos-chem-phys.net/11/2503/2011), doi:10.5194/acp-11-2503-2011
- 1428 Jin, X., Fiore, A., Boersma, K. F., Smedt, I. D., and Valin, L.: Inferring Changes in  
1429 Summertime Surface Ozone–NO<sub>x</sub>–VOC Chemistry over U.S. Urban Areas from  
1430 Two Decades of Satellite and Ground-Based Observations, *Environmental Science*  
1431 *Technology*, 54, 6518–6529, <https://doi.org/10.1021/acs.est.9b07785>, 2020



- 1432 Kang, D., K. Foley, R. Mathur, S. Roselle, K. Pickering, and D. Allen, Lightning NO<sub>x</sub>  
1433 Production in CMAQ Part II – Performance Evaluations, *Geosci. Model Devel.*, 12,  
1434 4409–4424, <https://doi.org/10.5194/gmd-12-4409-2019>, 2019.
- 1435 Kaynak, B., Hu, Y., Martin, R. V., Russell, A. G., Choi, Y., & Wang, Y. (2008). The effect  
1436 of lightning NO<sub>x</sub> production on surface ozone in the continental United States.  
1437 *Atmospheric Chemistry and Physics*, 8, 5151–5159.
- 1438 Koven et al., (2013) <https://bg.copernicus.org/articles/10/7109/2013/>
- 1439 Kitagawa, N., (1989) Long-term variations in thunder-day frequencies in Japan. *J. Geophys.*  
1440 *Res.*, 94, 13 183–13 189, <https://doi.org/10.1029/JD094iD11p13183>.
- 1441 Koehler, T. L. (2020) Cloud-to-Ground Lightning Flash Density and Thunderstorm Day  
1442 Distributions over the Contiguous United States Derived from NLDN Measurements:  
1443 1993–2018, *Mon. Weather Rev.*, DOI: 10.1175/MWR-D-19-0211.1
- 1444 Kopacz, M., Jacob, D. J., Fisher, J. A., Logan, J. A., Zhang, L., Megretskaia, I. A., Yantosca,  
1445 R. M., Singh, K., Henze, D. K., Burrows, J. P., Buchwitz, M., Khlystova, I., McMillan,  
1446 W. W., Gille, J. C., Edwards, D. P., Eldering, A., Thouret, V., and Nedelec, P.: Global  
1447 estimates of CO sources with high resolution by adjoint inversion of multiple satellite  
1448 datasets (MOPITT, AIRS, SCIAMACHY, TES), *Atmos. Chem. Phys.*, 10, 855–876,  
1449 <https://doi.org/10.5194/acp-10-855-2010>, 2010.
- 1450 Koshak, W., Peterson, H., Biazar, A., Khan, M., & Wang, L. (2014). The NASA Lightning  
1451 Nitrogen Oxides Model (LNOM): application to air quality modeling. *Atmospheric*  
1452 *Research*, 135, 363-369.
- 1453 Koshak, W.J., Cummins, K.L., Buechler, D.E., Vant-Hull, B., Blakeslee, R.J., Williams,  
1454 E.R. and Peterson, H.S. (2015) Variability of CONUS lightning in 2003–12 and  
1455 associated impacts. *Journal of Applied Meteorology and Climatology*, 54, 15– 41,  
1456 <https://doi.org/10.1175/JAMC-D-14-0072.1>.
- 1457 Krizan, P. and Lastovicka, J.: Trends in positive and negative ozone laminae in the Northern  
1458 Hemisphere, *Journal of Geophysical Research: Atmospheres*, 110,  
1459 <https://doi.org/https://doi.org/10.1029/2004JD005477>, 2005.
- 1460 Labow, G. J., Ziemke, J. R., McPeters, R. D., Haffner, D. P., and Bhartia, P. K.: A total  
1461 ozone-dependent ozone profile climatology based on ozonesondes and Aura MLS  
1462 data, *Journal of Geophysical Research: Atmospheres*, 120, 2537–2545,  
1463 <https://doi.org/10.1002/2014JD022634>, 2015.
- 1464 Labrador, L. J., Kuhlmann, R. V., and Lawrence, M. G. (2005), The effects of lightning-  
1465 produced NO<sub>x</sub> and its vertical distribution on atmospheric chemistry: sensitivity  
1466 simulations with MATCH-MPIC, *Atmos. Chem. Phys.*, 5, 1815-1834.
- 1467 Lacis, A. A., Wuebbles, D. J., and Logan, J. A. (1990), Radiative forcing of climate by  
1468 changes in the vertical distribution of ozone, *J. Geophys. Res.*, 95, 9971-9982.
- 1469 Lapierre, J. L., Laughner, J. L., Geddes, J. A., Koshak, W. J., Cohen, R. C., Pusede, S. E.  
1470 (2020), Observing U.S. regional variability in lightning NO<sub>2</sub> production rates, *J.*  
1471 *Geophys. Res.*, 125 (5), <https://doi.org/10.1029/2019JD031362>.





- 1472 Lavigne, T., C. Liu, and N. Liu, (2019) How does the trend in thunder days relate to  
1473 the variation of lightning flash density? *J. Geophys. Res. Atmos.*, 124, 4955–  
1474 4974, <https://doi.org/10.1029/2018JD029920>
- 1475 Lefohn, AS, Malley, CS, Smith, L, Wells, B, Hazucha, M, Simon, H, Naik, V, Mills, G,  
1476 Schultz, MG, Paoletti, E, De Marco, A, Xu, X, Zhang, L, Wang, T, Neufeld, HS,  
1477 Musselman, RC, Tarasick, D, Brauer, M, Feng, Z, Tang, H, Kobayashi, K, Sicard, P,  
1478 Solberg, S and Gerosa, G, 2018. Tropospheric ozone assessment report: Global ozone  
1479 metrics for climate change, human health, and crop/ecosystem research. *Elem Sci*  
1480 *Anth*, 6: 28. DOI: 10.1525/elementa.279.
- 1481 Lelieveld, J.; P. J. Crutzen (1991). The role of clouds in tropospheric photochemistry. , 12(3),  
1482 229–267. doi:10.1007/bf00048075
- 1483 Liaskos, C. E., Allen, D. J., & Pickering, K. E. (2015), Sensitivity of tropical tropospheric  
1484 composition to lightning NO<sub>x</sub> production as determined by replay simulations with  
1485 GEOS-5, *J. Geophys. Res. Atmos.*, 120, 8512–8534, doi:[10.1002/2014JD022987](https://doi.org/10.1002/2014JD022987).
- 1486 Liu, Y., Williams, E. R., Guha, A., & Said, R. (2021), How will lightning change during the  
1487 pollution-reduced COVID-19 pandemic period? A data study on the global lightning  
1488 activity, AGU Fall Meeting 2021.
- 1489 Liu et al., (2021) <https://acp.copernicus.org/articles/21/17743/2021/>
- 1490 Liu, J., Strode, S. A., Liang, Q., Oman, L.D., Colarco, P. R., Fleming, E. L., et al. (2022).  
1491 Change in tropospheric ozone in the recent decades and its contribution to global total  
1492 ozone. *Journal of Geophysical Research: Atmospheres*, 127, e2022JD037170.  
1493 <https://doi.org/10.1029/2022JD037170>
- 1494 Li et al. (2011) <https://doi.org/10.1016/j.chnaes.2010.11.006>
- 1495 Marais, E. A., Jacob, D. J., Choi, S., Joiner, J., Belmonte-Rivas, M., Cohen, R. C., et al.  
1496 (2018). Nitrogen oxides in the global upper troposphere: interpreting cloud-sliced  
1497 NO<sub>2</sub> observations from the OMI satellite instrument, *Atmospheric Chemistry and*  
1498 *Physics*, <https://doi.org/10.5194/acp-18-17017-2018>
- 1499 Martin, R. V., Sauvage, B., Folkins, I., Sioris, C. E., Boone, Bernath, C. P., & Ziemke, J.  
1500 (2007), Space-based constraints on the production of nitric oxide by lightning, *J.*  
1501 *Geophys. Res.*, 112, D09309, doi:10.1029/2006JD007831.
- 1502 Matandirotya, N.R., Burger, R. An assessment of NO<sub>2</sub> atmospheric air pollution over three  
1503 cities in South Africa during 2020 COVID-19 pandemic. *Air Qual Atmos Health* **16**,  
1504 263–276 (2023). <https://doi.org/10.1007/s11869-022-01271-3>
- 1505 McDuffie, E. E., Smith, S. J., O'Rourke, P., Tibrewal, K., Venkataraman, C., Marais, E. A.,  
1506 Zheng, B., Crippa, M., Brauer, M., and Martin, R. V.: A global anthropogenic emission  
1507 inventory of atmospheric pollutants from sector- and fuel-specific sources (1970–  
1508 2017): an application of the Community Emissions Data System (CEDS), *Earth Syst.*  
1509 *Sci. Data*, 12, 3413–3442, <https://doi.org/10.5194/essd-12-3413-2020>, 2020.
- 1510 Meng, L., Liu, J., Tarasick, D. W., Randel, W. J., Steiner, A. K., Wilhelmsen, H., Wang, L.,  
1511 and Haimberger, L. (2021). Continuous rise of the tropopause in the Northern  
1512 Hemisphere over 1980–2020. *Science Advances*,  
1513 <https://doi.org/10.1126/sciadv.abi8065>, 2021.



- 1514 Mills G, Pleijel H, Malley CS, Sinha B, Cooper OR, Schultz MG, Neufeld HS, Simpson D,  
1515 Sharps K, Feng Z, Gerosa G, Harmens H, Kobayashi K, Saxena P, Paoletti E, Sinha  
1516 V, Xu X., [Tropospheric Ozone Assessment Report: Present-day tropospheric ozone](#)  
1517 [distribution and trends relevant to vegetation](#). *Elem Sci Anth*. 2018;6(1):47. DOI:  
1518 10.1525/elementa.302.
- 1519 Miyazaki, K., H. J. Eskes, K. Sudo, and C. Zhang, (2014) Global lightning NO<sub>x</sub> production  
1520 estimated by an assimilation of multiple satellite data sets, *Atmos. Chem Phys.*, 14,  
1521 3277–3305,  
1522 [www.atmos-chem-phys.net/14/3277/2014/doi:10.5194/acp-14-3277-2014](http://www.atmos-chem-phys.net/14/3277/2014/doi:10.5194/acp-14-3277-2014).
- 1523 Miyazaki, K., Bowman, K., Sekiya, T., Eskes, H., Boersma, F., Worden, H., Livesey, N.,  
1524 Payne, V. H., Sudo, K., Kanaya, Y., Takigawa, M., and Ogochi, K.: Updated  
1525 tropospheric chemistry reanalysis and emission estimates, TCR-2, for 2005–2018,  
1526 *Earth Syst. Sci. Data*, 12, 2223–2259, <https://doi.org/10.5194/essd-12-2223-2020>,  
1527 2020.
- 1528 McPeters, R. D. and Labow, G. J.: Climatology 2011: An MLS and sonde derived ozone  
1529 climatology for satellite retrieval algorithms, *Journal of Geophysical Research:*  
1530 *Atmospheres*, 117, n/a-n/a, <https://doi.org/10.1029/2011JD017006>, 2012.
- 1531 Molod, A., Takacs, L., Suarez, M., and Bacmeister, J.: Development of the GEOS-5  
1532 atmospheric general circulation model: evolution from MERRA to MERRA2,  
1533 *Geosci. Model Dev.*, 8, 1339–1356, <https://doi.org/10.5194/gmd-8-1339-2015>, 2015.
- 1534 Murray, L. T. (2018), An uncertain future for lightning, *Nature Climate Change*, 8, 191-192.
- 1535 Murray, L. T. (2016), Lightning NO<sub>x</sub> and Impacts on Air Quality, *Curr Pollution Rep* (2016)  
1536 2:115–133, DOI 10.1007/s40726-016-0031-7
- 1537 Murray, L. T., D. J. Jacob, J. A. Logan, R. C. Hudman, and W. J. Koshak (2012), Optimized  
1538 regional and interannual variability of lightning in a global chemical transport model  
1539 constrained by LIS/OTD satellite data, *J. Geophys. Res.*, 117, D20307,  
1540 doi:[10.1029/2012JD017934](https://doi.org/10.1029/2012JD017934).
- 1541 Nault, B. A., Garland, C., Wooldridge, J. L., Brune, W. H., Campuzano-Jost, P., Crouse, J.  
1542 D., et al. (2016). Observational Constraints on the Oxidation of NO<sub>x</sub> in the Upper  
1543 Troposphere, *The Journal of Physical Chemistry A*, 120 (9), 1468-1478, doi:  
1544 10.1021/acs.jpca.5b07824
- 1545 Nault, B. A., Laughner, J. L., Wooldridge, P. J., Crouse, J. D., Dibb, J., Diskin, et al.  
1546 (2017). Lightning NO<sub>x</sub> emissions: reconciling measured and modeled estimates with  
1547 updated NO<sub>x</sub> chemistry. *Geophysical Research Letters*, 44, 9479–9488.
- 1548 Newton, R., Vaughan, G., Ricketts, H. M. A., Pan, L. L., Weinheimer, A. J., and Chemel, C.:  
1549 Ozone profiles from the West Pacific Warm Pool: measurements and  
1550 validation, *Atmos Chem Phys*, 16, 619–634, [https://doi.org/10.5194/acp-16-619-](https://doi.org/10.5194/acp-16-619-2016)  
1551 2016, 2016.
- 1552 Nielsen, J. Eric, et al. "Chemical mechanisms and their applications in the Goddard Earth  
1553 Observing System (GEOS) earth system model." *Journal of Advances in Modeling*  
1554 *Earth Systems* 9.8 (2017): 3019-3044.
- 1555 Oleribe OO, Suliman AAA, Taylor-Robinson SD, Corrah T. Possible Reasons Why Sub-  
1556 Saharan Africa Experienced a Less Severe COVID-19 Pandemic in 2020. *J*



- 1557 *Multidiscip Healthc.* 2021;14:3267-3271, <https://doi.org/10.2147/JMDH.S331847>,  
1558 2021.
- 1559 Orbe, C., Oman, L. D., Strahan, S. E., Waugh, D. W., Pawson, S., Takacs, L. L., and Molod,  
1560 A. M. (2017). Large-scale atmospheric transport in GEOS replay simulations. *Journal*  
1561 *of Advances in Modeling Earth Systems*, 9, 2545–2560.  
1562 <https://doi.org/10.1002/2017MS001053>
- 1563 Ott, L. E., K. E. Pickering, G. L. Stenchikov, H. Huntrieser, and U. Schumann (2007),  
1564 Effects of lightning NO<sub>x</sub> production during the 21 July European Lightning Nitrogen  
1565 Oxides Project storm studied with a three-dimensional cloud-scale chemical transport  
1566 model, *J. Geophys. Res.*, 112, D05307, doi:10.1029/2006JD007365.
- 1567 Ott, L. E., K. E. Pickering, G. L. Stenchikov, D. J. Allen, A. J. DeCaria, B. Ridley, R.-F. Lin,  
1568 S. Lang, and W.-K. Tao (2010), Production of lightning NO<sub>x</sub> and its vertical  
1569 distribution calculated from three-dimensional cloud-scale chemical transport model  
1570 simulations, *J. Geophys. Res.*, 115, D04301, doi:10.1029/2009JD011880 Philipona, R.,  
1571 C. Mears, M. Fujiwara, P. Jeannet, P. Thorne, G. Bodeker, L. Haimberger, M. Hervo,  
1572 C. Popp, G. Romanens, W. Steinbrecht, R. Stubi, R. Van Malderen, adiosondes show  
1573 that after decades of cooling, the lower stratosphere is now warming. *J. Geophys.*  
1574 *Res. Atmos.* 123, 12509–12522 (2018).
- 1575 Pickering, K. E., A. M. Thompson, R. R. Dickerson, W. T. Luke, D. P. McNamara, J. P.  
1576 Greenberg, and P. R. Zimmerman, Model calculations of tropospheric ozone  
1577 production potential following observed convective events, *J. Geophys. Res.*,  
1578 95:14,049-14,062, 1990.
- 1579 Pickering, K. E., Y. Wang, W.-K. Tao, C. Price, and J.-F. Mueller, Vertical distributions of  
1580 lightning NO<sub>x</sub> for use in regional and global chemical transport models, *J. Geophys.*  
1581 *Res.*, 103: 31,203-31,216, 1998.
- 1582 Pickering, K. E., E. Bucsela, D. Allen, A. Ring, R. Holzworth, and N. Krotkov (2016),  
1583 Estimates of lightning NO<sub>x</sub> production based on OMI NO<sub>2</sub> observations over the Gulf  
1584 of Mexico, *J. Geophys. Res. Atmos.*, 121, doi:[10.1002/2015JD024179](https://doi.org/10.1002/2015JD024179).
- 1585 Pickering, K. E., Y. Li, K. A. Cummings, M. C. Barth, D. J. Allen, E. Bruning, (2023)  
1586 Lightning NO<sub>x</sub> in the May 29-30, 2012 Deep Convective Clouds and Chemistry  
1587 (DC3) Severe Storm and its Downwind Chemical Consequences, *J. Geophys. Res.-*  
1588 *Atmos.*, to be submitted.
- 1589 Pinto, O., Jr., K. P. Naccarato, and I. R. C. A. Pinto, 2013: Thunderstorm incidence in  
1590 southeastern Brazil estimated from different data sources. *Ann. Geophys.*, 31,  
1591 1213–1219, <https://doi.org/10.5194/angeo-31-1213-2013>.
- 1592 Prodromos Zanis, Dimitris Akritidis, Steven Turnock, Vaishali Naik, Sophie  
1593 Szopa, Aristeidis K Georgoulas, Susanne E Bauer, Makoto Deushi, Larry W  
1594 Horowitz, James Keeble, Climate change penalty and benefit on surface ozone: a  
1595 global perspective based on CMIP6 earth system models, [Environmental Research](https://doi.org/10.1088/1748-9326/ac4a34)  
1596 [Letters, Volume 17, Number 2, DOI: https://doi.org/10.1088/1748-9326/ac4a34](https://doi.org/10.1088/1748-9326/ac4a34)
- 1597 Pollack, I. B., C. R. Homeyer, T. B. Ryerson, K. C. Aikin, J. Peischl, E. C. Apel, T. Campos,  
1598 F. Flocke, R. S. Hornbrook, D. J. Knapp, et al. (2016), Airborne quantification of  
1599 upper tropospheric NO<sub>x</sub> production from lightning in deep convective storms over the



- 1600 United States Great Plains, *J. Geophys. Res. Atmos.*, 121, 2002–2028,  
1601 doi:[10.1002/2015JD023941](https://doi.org/10.1002/2015JD023941).
- 1602
- 1603 Prather, M. J. and D. J. Jacob (1997) A persistent imbalance in HO<sub>x</sub> and NO<sub>x</sub> photochemistry  
1604 of  
1605 the upper troposphere driven by deep tropical convection, *Geophys. Res. Lett.*, 24,  
1606 3189 – 3192.
- 1607 Price, C., J. Penner, and M. Prather (1997), NO<sub>x</sub> from lightning 1. Global distribution based  
1608 on lightning physics, *J. Geophys. Res.*, 102 (D5), 5929-5941.
- 1609 Price, C. G., (2013) Lightning Applications in Weather and Climate Research, *Surv.*  
1610 *Geophys.* (2013) 34:755–767, DOI 10.1007/s10712-012-9218-7
- 1611 Qie, K., Qie, X., & Tian, W. (2021), Increasing trend of lightning activity in the South Asian  
1612 region, *Science Bulletin*, 66 (1), 78-84.
- 1613 Qie, K., Tian, W., Wang, W., Wu, X., Yuan, T., Tian, H., Luo, J., Zhang, R., & Want, T.  
1614 Regional trends of lightning activity in the tropics and subtropics, *Atmos.*  
1615 *Res.*, 242 (2020), Article 104960, [10.1016/j.atmosres.2020.104960](https://doi.org/10.1016/j.atmosres.2020.104960)
- 1616 Randel, W. J., L. Polvani, F. Wu, D. E. Kinnison, C.-Z. Zou, C. Mears, Troposphere  
1617 stratosphere temperature trends derived from satellite data compared with ensemble  
1618 simulations from WACCM. *J. Geophys. Res. Atmos.* 122, 9651–9667 (2017).
- 1619 Ren, X., J. R. Olson, J. H. Crawford, W. H. Brune, J. Mao, R. B. Long, G. Chen, M. A.  
1620 Avery, G. W. Sachse, J. D. Barrick, G. S. Diskin, L. G. Huey, Alan Fried, Ronald C.  
1621 Cohen, Brian Heikes, Paul Wennberg, Hanwant B. Singh, Donald R. Blake, Richard  
1622 E. Shetter, (2008) HO<sub>x</sub> Chemistry during INTEX–A 2004: Observation, Model  
1623 Calculations and comparison with previous studies, *J. Geophys. Res.*, 113, D05310,  
1624 doi:10.1029/2007JD009166.
- 1625 Ridley, B., Ott, L., Pickering, K., Emmons, L., Montzka, D., Weinheimer, A., et al. (2004),  
1626 Florida thunderstorms: A faucet of reactive nitrogen to the upper troposphere, *J.*  
1627 *Geophys. Res.*, 109 (D17), 10.1029/2004JD004769.
- 1628 Romps, D. M., Seeley, J. T., Vollaro, D., & Molinar, J. (2014), Projected increase in  
1629 lightning strikes in the United States due to global warming, *Science*, 851-854.
- 1630 Romps, D. M., Charn, A. B., Holzworth, R. H., Lawrence, W. E., Molinari, J., & Vollaro, D.  
1631 (2018). CAPE times P explains lightning over land but not the land-ocean contrast.  
1632 *Geophysical Research Letters*, 45, 12,623–12,630.  
1633 <https://doi.org/10.1029/2018GL080267>
- 1634 Romps, D. M. (2019). Evaluating the future of lightning in cloud-resolving models.  
1635 *Geophysical Research Letters*, 46, <https://doi.org/10.1029/2019GL085748>
- 1636 Sanap, S. D. (2021) Global and regional variations in aerosol loading during COVID-19  
1637 imposed lockdown, *Atmos. Environ.*, 246, <https://doi.org/10.1016/j.atmosenv.2020.118132>.
- 1638 Sauvage, B., R. V. Martin, A. van Donkelaar, and J. R. Ziemke (2007) Quantification of the  
1639 factors controlling tropical tropospheric ozone and the South Atlantic maximum, *J.*  
1640 *Geophys. Res.*, 112, D11309, doi:10.1029/2006JD008008.



- 1641 Sanap, S. D. (2021) Global and regional variations in aerosol loading during COVID-19  
1642 imposed lockdown, *Atmos. Environ.*, 246, <https://doi.org/10.1016/j.atmosenv.2020.118132>.
- 1643 Sauvage, B., R. V. Martin, A. van Donkelaar, and J. R. Ziemke (2007) Quantification of the  
1644 factors controlling tropical tropospheric ozone and the South Atlantic maximum, *J.*  
1645 *Geophys. Res.*, 112, D11309, doi:10.1029/2006JD008008.
- 1646 Sanap, S. D. (2021) Global and regional variations in aerosol loading during COVID-19  
1647 imposed lockdown, *Atmos. Environ.*, 246, <https://doi.org/10.1016/j.atmosenv.2020.118132>.
- 1648 Sauvage, B., R. V. Martin, A. van Donkelaar, and J. R. Ziemke (2007) Quantification of the  
1649 factors controlling tropical tropospheric ozone and the South Atlantic maximum, *J.*  
1650 *Geophys. Res.*, 112, D11309, doi:10.1029/2006JD008008.
- 1651 Schumann, U., and H. Huntrieser (2007), The global lightning-induced nitrogen oxides  
1652 source, *Atmos. Chem. Phys.*, 7, 3823-3907.
- 1653 Sen, P (1968). Estimated of the regression coefficient based on Kendall's Tau. *J Am Stat*  
1654 *Assoc* 39:1379-1389
- 1655 Shi, Z., H. Wang, Y. Tan, L. Li, C. Li, (2020) Influence of aerosols on lightning activities in  
1656 central eastern parts of China, *Atmos Sci Lett.*, 21:e957,  
1657 <https://doi.org/10.1002/asl.957>.
- 1658 Sourì, A. H., Johnson, M. S., Wolfe, G. M., Crawford, J. H., Fried, A., Wisthaler, A., Brune,  
1659 W. H., Blake, D. R., Weinheimer, A. J., Verhoelst, T., Compernelle, S., Pinardi, G.,  
1660 Vigouroux, C., Langerock, B., Choi, S., Lamsal, L., Zhu, L., Sun, S., Cohen, R. C.,  
1661 Min, K.-E., Cho, C., Philip, S., Liu, X., and Chance, K.: Characterization of errors in  
1662 satellite-based HCHONO<sub>2</sub> tropospheric column ratios with respect to chemistry,  
1663 column-to-PBL translation, spatial representation, and retrieval uncertainties,  
1664 *Atmospheric Chemistry and Physics*, 23, 1963–1986, [https://doi.org/10.5194/acp-23-](https://doi.org/10.5194/acp-23-1963-2023)  
1665 [1963-2023](https://doi.org/10.5194/acp-23-1963-2023), 2023
- 1666 Stauffer, R. M., Thompson, A. M., Kollonige, D., Tarasick, D., Van Malderen, R., Smit, H.  
1667 G. J., Vömel, H., Morris, G., Johnson, B. J., Cullis, P., and et al.: An Examination of  
1668 the Recent Stability of Ozone Global Network Data, *Earth and Space Science*  
1669 *Open Archive*, 48, <https://doi.org/10.1002/essoar.10511590.1>, 2022.
- 1670 Steinbrecht, W., Claude, H., Köhler, U., and Hoinka, K. P.: Correlations between tropopause  
1671 height and total ozone: Implications for long-term changes, *J. Geophys. Res.*, 103,  
1672 19183–19192, <https://doi.org/10.1029/98JD01929>, 1998.
- 1673 Steiner, A. K., F. Ladst. dter, W. J. Randel, A. C. Maycock, Q. Fu, C. Claud, H. Gleisner, L.  
1674 Haimberger, S. -P. Ho, P. Keckhut, T. Leblanc, C. Mears, L. M. Polvani, B. D.  
1675 Santer, T. Schmidt, V. Sofieva, R. Wing, C. -Z. Zou, Observed temperature changes  
1676 in the troposphere and stratosphere from 1979 to 2018. *J. Climate* 33, 8165–8194  
1677 (2020).
- 1678 Strahan, S. E., Duncan, B. N., and Hoor, P. (2007). Observationally derived transport  
1679 diagnostics for the lowermost stratosphere and their application to the GMI chemistry  
1680 and transport model. *Atmospheric Chemistry and Physics*, 7(9), 2435–2445.  
1681 <https://doi.org/10.5194/acp-7-2435-2007>.
- 1682 Sue et al. 2011: <https://doi.org/10.1126/science.1208839>





- 1683 Schultz, M.G., Schröder, S., Lyapina, O., Cooper, O., Galbally, I., Petropavlovskikh, I., von  
1684 Schneidmesser, E., Tanimoto, H., Elshorbany, Y., Naja, M., Seguel, R., Dauert, U.,  
1685 Eckhardt, P., Feigenspahn, S., Fiebig, M., Hjellbrekke, A.-G., Hong, Y.-D., Christian  
1686 Kjeld, P., Koide, H., Lear, G., Tarasick, D., Ueno, M., Wallasch, M., Baumgardner,  
1687 D., Chuang, M.-T., Gillett, R., Lee, M., Molloy, S., Moolla, R., Wang, T., Sharps, K.,  
1688 Adame, J.A., Ancellet, G., Apadula, F., Artaxo, P., Barlasina, M., Bogucka, M.,  
1689 Bonasoni, P., Chang, L., Colomb, A., Cuevas, E., Cupeiro, M., Degorska, A., Ding,  
1690 A., Fröhlich, M., Frolova, M., Gadhavi, H., Gheusi, F., Gilge, S., Gonzalez, M.Y.,  
1691 Gros, V., Hamad, S.H., Helmig, D., Henriques, D., Hermansen, O., Holla, R., Huber,  
1692 J., Im, U., Jaffe, D.A., Komala, N., Kubistin, D., Lam, K.-S., Laurila, T., Lee, H.,  
1693 Levy, I., Mazzoleni, C., Mazzoleni, L., McClure-Begley, A., Mohamad, M., Murovic,  
1694 M., Navarro-Comas, M., Nicodim, F., Parrish, D., Read, K.A., Reid, N., Ries, L.,  
1695 Saxena, P., Schwab, J.J., Scorgie, Y., Senik, I., Simmonds, P., Sinha, V., Skorokhod,  
1696 A., Spain, G., Spangl, W., Spoor, R., Springston, S.R., Steer, K., Steinbacher, M.,  
1697 Suharguniyawan, E., Torre, P., Trickl, T., Weili, L., Weller, R., Xu, X., Xue, L. and  
1698 Zhiqiang, M., Tropospheric Ozone Assessment Report: Database and Metrics Data of  
1699 Global Surface Ozone Observations. 2017. *Elem Sci Anth*, 5, p.58. DOI:  
1700 10.1525/elementa.244.
- 1701 Tarasick, D., Galbally, I.E., Cooper, O.R., Schultz, M.G., Ancellet, G., Leblanc, T.,  
1702 Wallington, T.J., Ziemke, J., Liu, X., Steinbacher, M., Staehelin, J., Vigouroux, C.,  
1703 Hannigan, J.W., García, O., Foret, G., Zanis, P., Weatherhead, E., Petropavlovskikh,  
1704 I., Worden, H., Osman, M., Liu, J., Chang, K.-L., Gaudel, A., Lin, M., Granados-  
1705 Muñoz, M., Thompson, A.M., Oltmans, S.J., Cuesta, J., Dufour, G., Thouret, V.,  
1706 Hassler, B., Trickl, T. and Neu, J.L., 2019. Tropospheric Ozone Assessment Report:  
1707 Tropospheric ozone from 1877 to 2016, observed levels, trends and uncertainties.  
1708 Tropospheric Ozone Assessment Report: Tropospheric ozone from 1877 to 2016,  
1709 observed levels, trends and uncertainties. *Elem Sci Anth*, 7(1), p.39. DOI :  
1710 10.1525/elementa.376, 2019.
- 1711 Thompson, A. M., Witte, J. C., Sterling, C., Jordan, A., Johnson, B. J., Oltmans, S. J.,  
1712 Fujiwara, M., Vömel, H., Allaart, M., Piders, A., Coetzee, G. J. R., Posny, F.,  
1713 Corrales, E., Diaz, J. A., Félix, C., Komala, N., Lai, N., Ahn Nguyen, H. T., Maata,  
1714 M., Mani, F., Zainal, Z., Ogino, S., Paredes, F., Penha, T. L. B., Silva, F. R., Sallons-  
1715 Mitro, S., Selkirk, H. B., Schmidlin, F. J., Stübi, R., and Thiongo, K.: First  
1716 Reprocessing of Southern Hemisphere Additional Ozonesondes (SHADOZ) Ozone  
1717 Profiles (1998–2016): 2. Comparisons With Satellites and Ground-Based Instruments,  
1718 *Journal of Geophysical Research: Atmospheres*, 122,  
1719 <https://doi.org/10.1002/2017JD027406>, 2017.
- 1720 Tsvilidou, M., Sauvage, B., Barret, B., Wolff, P., Clark, H., Bennouna, Y., Blot, R.,  
1721 Boulanger, D., Nédélec, P., Le Flochmoën, E., and Thouret, V.: Tropical tropospheric  
1722 ozone and carbon monoxide distributions: characteristics, origins and control factors,  
1723 as seen by IAGOS and IASI, *Atmos. Chem. Phys. Discuss.* (preprint),  
1724 <https://doi.org/10.5194/acp-2022-686>, in review, 2022.
- 1725 Turnock, S. T., Allen, R. J., Andrews, M., Bauer, S. E., Deushi, M., Emmons, L., Good, P.,  
1726 Horowitz, L., John, J. G., Michou, M., Nabat, P., Naik, V., Neubauer, D., O'Connor,  
1727 F. M., Olivie, D., Oshima, N., Schulz, M., Sellar, A., Shim, S., Takemura, T., Tilmes,  
1728 S., Tsigaridis, K., Wu, T., and Zhang, J.: Historical and future changes in air



- 1729 pollutants from CMIP6 models, *Atmos. Chem. Phys.*, 20, 14547–14579,  
1730 <https://doi.org/10.5194/acp-20-14547-2020>, 2020.
- 1731 Theil, H. (1950), “A rank-invariant method of linear and polynomial regression analysis. I,  
1732 II, III”, *Nederl. Akad. Wetensch., Proc.*, 53: 386–392, 521–525, 1397–1412.
- 1733 Verma, S., Yadava, P. K., Lal, D. M., Mall, R. K., Harshbardhan, K., & Payra, S. (2021),  
1734 Role of Lightning NO<sub>x</sub> in ozone formation: A review, *Pure and Applied Geophysics*,  
1735 178, 1425-1443.
- 1736 Wang, H., Shi, Z., Wang, X., Tan, Y., Wang, H., Li, L., & Lin, X. (2021), Cloud-to-Ground  
1737 Lightning Response to Aerosol over Air-Polluted Urban Areas in China. *Remote*  
1738 *Sens.* 13, 2600. <https://doi.org/10.3390/rs13132600>
- 1739 Wang, H., Lu, X., Jacob, D. J., Cooper, O. R., Chang, K.-L., Li, K., Gao, M., Liu, Y., Sheng,  
1740 B., Wu, K., Wu, T., Zhang, J., Sauvage, B., Nédélec, P., Blot, R., and Fan, S.: Global  
1741 tropospheric ozone trends, attributions, and radiative impacts in 1995–2017: an  
1742 integrated analysis using aircraft (IAGOS) observations, ozonesonde, and multi-  
1743 decadal chemical model simulations, *Atmos Chem Phys*, 22, 13753–13782,  
1744 <https://doi.org/10.5194/acp-22-13753-2022>, 2022.
- 1745 Wang, Y., A. W. DeSilva, G. C. Goldenbaum, and R. R. Dickerson, (1998) Nitric oxide  
1746 production by simulated lightning: Dependence on current, energy, and pressure, *J.*  
1747 *Geophys. Res.*, 103, 19,149-19,159.
- 1748 Wilcox, R. (2001). *Fundamentals of Modern Statistical Methods: Substantially Improving*  
1749 *Power and Accuracy*. Springer Science and Business Media.
- 1750 Wu, D., Zhang, J., Wang, M., An, J., Wang, R., Haider, H., et al. (2022). Global and regional  
1751 patterns of soil nitrous acid emissions and their acceleration of rural photochemical  
1752 reactions. *Journal of Geophysical Research: Atmospheres*, 127, e2021JD036379.  
1753 <https://doi.org/10.1029/2021JD036379>
- 1754 WMO, 1992, *International Meteorological Vocabulary* (2nd ed.), Geneva: Secretariat of the  
1755 World Meteorological Organization. 1992. p. 636. ISBN 978-92-63-02182-3)
- 1756 Wang and Chen, 2012: <https://doi.org/10.1016/j.geoderma.2011.11.009>
- 1757 Xue, X., Ren, G. Y., Xu, X. D., Sun, X. B., Yang, G. W., Zhang, P. F., & Zhang, S. Q.  
1758 (2021), The trends of warm-season thunderstorm and lightning days in China and the  
1759 influence of environmental factors, *J. Geophys. Res.*, 126 (15),  
1760 10.1029/2021JD034950.
- 1761 Yang, X., and Z. Li, 2014: Increases in thunderstorm activity and relationships with air  
1762 pollution in southeast China, *J. Geophys. Res. Atmos.*, 119, 1835–1844,  
1763 doi:10.1002/2013JD021224.
- 1764 Yin, Y., Chevallier, F., Ciais, P., Broquet, G., Fortems-Cheiney, A., Pison, I., and Saunois, M.:  
1765 Decadal trends in global CO emissions as seen by MOPITT, *Atmos. Chem. Phys.*, 15,  
1766 13433–13451, <https://doi.org/10.5194/acp-15-13433-2015>, 2015.
- 1767 Young, P.J., Naik, V., Fiore, A.M., Gaudel, A., Guo, J., Lin, M.Y., Neu, J.L., Parrish, D.D.,  
1768 Rieder, H.E., Schnell, J.L., Tilmes, S., Wild, O., Zhang, L., Ziemke, J.R., Brandt, J.,  
1769 Delcloo, A., Doherty, R.M., Geels, C., Hegglin, M.I., Hu, L., Im, U., Kumar, R.,  
1770 Luhar, A., Murray, L., Plummer, D., Rodriguez, J., Saiz-Lopez, A., Schultz, M.G.,



- 1771 Woodhouse, M.T. and Zeng, G. Tropospheric Ozone Assessment Report: Assessment  
1772 of global-scale model performance for global and regional ozone distributions,  
1773 variability, and trends. 2018. Elem Sci Anth, 6(1), p.10. DOI: 10.1525/elementa.265.
- 1774 Zhang, X., Yin, Y., van der A, R., Lapierre, J. L., Chen, Q., Kuang, X., Yan, S., Chen, J., He,  
1775 C., and Shi, R. (2020), Estimates of lightning NO<sub>x</sub> production based on high-  
1776 resolution OMI NO<sub>2</sub> retrievals over the continental US, Atmos. Meas. Tech., 13,  
1777 1709–1734, <https://doi.org/10.5194/amt-13-1709-2020> .
- 1778 Zhang et al., 2020: <https://doi.org/10.1016/j.atmosenv.2020.117596>
- 1779 Zhang, L., T. Wang, Q. Zhang, J. Zheng, Z. Xu, and M. Lv (2016), Potential sources of nitrous  
1780 acid (HONO) and their impacts on ozone: A WRF-Chem study in a polluted subtropical  
1781 region, J. Geophys. Res. Atmos., 121, 3645–3662, doi:10.1002/2015JD024468.
- 1782